# Heat Transfer Enhancement of Latent Thermal Energy Storage System Using Multiple Tubes and Modified Shell Designs

by

Rehan Qaiser

A thesis submitted in partial fulfillment for the
degree of Master of Science in Mechanical Engineering

in the

Faculty of Engineering

Department of Mechanical Engineering

2020

*This postulation is dedicated to my parents and teachers, who are constantly a light for me in obscurity and their unflinching help, guided my unfocused words into Sound thoughts*

# CERTIFICATE OF APPROVAL

# Heat Transfer Enhancement of Latent Thermal Energy Storage System Using Multiple Tubes and Modified Shell Designs

by

**(Rehan Qaiser)**

Registration No: MME183004

## THESIS EXAMINING COMMITTEE

| S. No. | Examiner | Name | Organization |
|--------|----------|------|--------------|
| (a) | External Examiner | Dr. Muhammad Anwar | IST, Islamabad |
| (b) | Internal Examiner | Dr. Khawar Naveed Abbasi | CUST, Islamabad |
| (c) | Supervisor | Dr. Muhammad Mahabat Khan | CUST, Islamabad |

---

Dr. Muhammad Mahabat khan

Thesis Supervisor

November, 2020

---

Dr. Muhammad Mahabat khan

Head

Dept. of Mechanical Engineering

November, 2020

Dr. Imtiaz Ahmad Taj

Dean

Faculty of Engineering

November, 2020

# *Author's Declaration*

I, **Rehan Qaiser,** hereby state that my MS thesis titled "**Heat Transfer Enhancement of Latent Thermal Energy Storage System Using Multiple Tubes and Modified Shell Designs**" is my own work and has not been previously submitted by me anywhere else for taking any degree. At any time if my statement is found to be incorrect even after my graduation, the University has the right to withdraw my MS Degree.

**(Rehan Qaiser)**

Registration No: MME183004

# *Plagiarism Undertaking*

I solemnly declare that research work presented in this thesis titled "**Heat Transfer Enhancement of Latent Thermal Energy Storage System Using Multiple Tubes and Modified Shell Designs**" is exclusively my research work with no remarkable contribution from any other individual. Small contribution/help wherever taken has been dully acknowledged and that complete thesis has been written by me. I understand the zero tolerance policy of the Higher Education Commission and CUST towards plagiarism. Therefore, I as an author of the above titled thesis declare that no part of my thesis has been plagiarized and any material used as reference is properly cited. I undertake that if I am found guilty of any formal plagiarism in the above titled thesis even after award of MS Degree, the University reserves the right to withdraw/revoke my MS degree and that HEC and the University have the right to publish my name on the HEC/University website on which names of students are placed who submitted plagiarized work.

**(Rehan Qaiser)**

Registration No: MME183004

# *List of Publications*

It is certified that following publication(s) has been made out of the research work that has been carried out for this thesis:

1. **R. Qaiser**, M. M. Khan, L. A. Khan and M. Irfan "Melting performance enhancement of PCM based thermal energy storage system using multiple tubes and modified shell designs," *Submitted in Journal of Energy Storage*, 2020.

**(Rehan Qaiser)**

Registration No: MME183004

# Acknowledgements

# *Abstract*

In this work, experimental and numerical investigations are performed for heat transfer enhancement in a horizontal shell and tube Latent Thermal Energy Storage System (LTESS) using multiple heat transfer tubes and modified shell designs. Stearic acid is used as a phase-change material and it is placed in the annulus of steel shell and copper tubes carrying water as heat transfer fluid (HTF). A single Y-fin HTF tube, used as a Base Case, is split up into $2-5$ tubes with different arrangements while ensuring constant mass of the PCM. To study the effect of splitting tubes on melting characteristics of PCM, two-dimensional buoyancy driven transient numerical methodology is adopted. A significant improvement in heat transfer is observed for vertical double tube configuration and triple tube V-configuration. The average heat transfer rate is enhanced by 33.6% and 23.7% by vertical double tube configuration and triple tube V-configuration, respectively, as compared to Base Case. The corresponding complete melting times are reduced by 27.7% and 21.7%. Additionally, elliptic and triangular shell design modifications are proposed for double and triple tube arrangements, respectively. Both configurations increase the average heat transfer rate by 85% which results in reduction of the complete PCM melting time by 50% with respect to Y-fins single tube arrangement. In comparison to the Base Case, an increase in HTF temperature of 5.6% improves the average Nusselt number by more than 37% for both the cases. Additionally, the correlations for melting Fourier number and average Nusselt number are also developed.

**Keywords: Multi-Tube Heat Exchanger, Buoyant Flow; Latent Heat; Energy Storage; Heat Transfer; Longitudinal Fins.**

# Contents

# List of Figures

# List of Tables

# Symbols

$a_{th}$      Thermal diffusivity, m$^2$/s

$C_p$      Specific Heat, J/kgK

$C_{ps}$      Solid PCM Specific Heat constant, J/kgK

$C_{pl}$      Liquid PCM Specific Heat constant, J/kgK

$A_{Mushy}$      Mushy zone constant

$D_t$      Tube Diameter, mm

$D_s$      Shell Diameter, mm

$D_{maj}$      Major Diameter, mm

$D_{min}$      Minor Diameter, mm

$S_t$      Shell Thickness, mm

$L_s$      Side Length, mm

$e_{th}$      Thermal effusivity, J/s$^0$.5 m$^2$K

$g$      Gravity, m/s$^2$

$h$      Enthalpy, J/kg

$h_c$      Heat Transfer Coefficient, W/m$^2$K

$\overline{h_c}$      Average Heat Transfer Coefficient, W/m$^2$K

$k_{PCM}$      Thermal Conductivity of PCM, W/mK

$l_f$      Fin Length, mm

$L_f$      latent Heat of Fusion, kJ/kg

$Nu$      Nusselt number

$\overline{Nu}$      Average Nusselt number

$Fo$      Fourier number

$E_R$      Enhancement ratio

$Q_E$        Total Energy Storage, W

$Ra$        Rayleigh number

$F_i$        Momentum Source Term

$F_B$        Buoyancy Source Term

$Ste$        Stefan number

$t_t$        Inner tube Thickness, mm

$b$        Buffer-layer thickness

$t$        time, min

$t_{ms}$        Melting time saving, min

$t_{m,max}$        Maximum Melting time, min

$t_{m,min}$        Minimum Melting time, min

$t_m$        Melting time, min

$t_f$        Fin Thickness, mm

$T$        Temperature, K

$\overline{T}$        Average Temperature, K

$T_s$        Solidus Temperature, K

$T_l$        Liquidus Temperature, K

$T_R$        Reference Temperature, K

$T_{HTF}$        Heat transfer fluid temperature, K

$T_{PCM}$        PCM temperature, K

$M_{pcm}$        Mass of PCM, kg

$u_i$        Velocity component, m/s

$\overline{\alpha}$        Average melting fraction

$\alpha$        Melting fraction

$\overline{\alpha_1}(t)$        Melting fraction of case 1

$\overline{\alpha_i}(t)$        Melting fraction of any case

$\rho_l$        Liquidus density, kg/m$^3$

$\rho$        Mean density, kg/m$^3$

$\rho_s$        Solidus density, kg/m$^3$

$\mu$        Viscosity, kg/ms

$\theta$        Orientation angle, degree

| | |
|---|---|
| $\beta$ | Coefficient of Thermal expansion, 1/K |
| $\nu_l$ | Kinematic Viscosity, m$^3$/s |
| $\xi$ | Small Number |
| $s$ | Solidus |
| $t$ | Tube |
| $l$ | Liquidus |
| $PCM$ | Phase change material |
| $c$ | Coefficient |
| $f$ | Fin |
| $HTF$ | Heat Transfer Fluid |
| $th$ | Thermal |
| $m, max$ | Maximum Melting |
| $m$ | Melting |
| $m, min$ | Minimum Melting |
| $BC$ | Base Case |
| $Ac_t$ | Cross-Sectional Area of Tube, mm$^2$ |
| $As_t$ | Surface Area of Tube, mm$^2$ |
| $N_t$ | Number of Tubes |
| $L_s$ | Side Length, mm |
| $L$ | Length of LTESS, m |
| $c_1, c_2$ | Constants |

# Abbreviations

**HTF**    Heat Transfer Fluid

**LTES**    Latent Thermal Energy Storage

**LTESS**    Latent Thermal Energy Storage System

**PCM**    Phase Change Material

**STES**    Sensible Thermal Energy Storage

**TCES**    Thermo-Chemical Energy Storage

**TES**    Thermal Energy Storage

# Chapter 1

# Introduction

## 1.1 Background

Energy conservation is one of the most focused area of research in current era. The increasing energy demand and depleting fossil fuels require incorporating alternate sources of energy to current energy mix. Nature provides thermal energy in the form of solar energy which is abundantly available, free of cost, causes no pollution, easily utilizable, and has continuity. This thermal energy is stored as latent heat thermal energy storage (LHTES), sensible heat thermal energy storage (SHTES) and thermo-chemical energy storage (TCES). In latent thermal energy storage, there involves a phase change of material while keeping the system's temperature constant like change from solid phase to liquid phase or vice versa. Whereas, in sensible thermal energy storage systems (STESs) only temperature of the material rises in order to store heat. STESs have high working temperatures and therefore requires chemical stability and high heat capacity. In thermo-chemical energy storage (TCES) systems, thermal energy is stored by use of chemical reactions which is recuperated through reverse chemical reactions. TCES generally require controlled environments and have relatively short working life.

Phase change Material (PCM) based latent thermal energy storage systems (LT-ESS) systems provide suitable solution to thermal energy management problems

due to their ability to store large amount of heat at relatively low working temperatures. Thermal energy is stored in PCMs in form of sensible and latent thermal heat [1] as shown in **Figure: 1.1** for charging (heating) and discharging (cooling) process. Therefore, LTESSs contribute in many applications in different engineering fields such as solar air collectors [2], heating and cooling systems of electronics products [3], thermal storage of building structures and refrigeration [4], drying technology, equipment of buildings such as hot water for domestic use [5], cold storage and waste heat recovery systems.
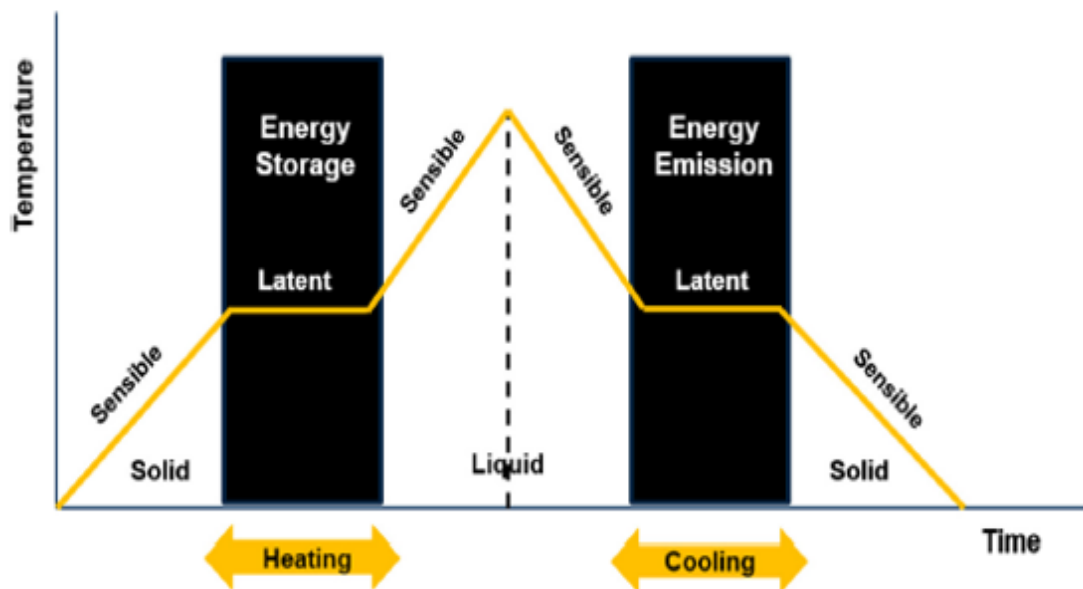


FIGURE 1.1: Schematic Diagram of the Phase Change Transition of PCM (Reproduced as it is from Kun Du et.al.,[4])

Generally, thermal energy is stored in fluid called heat transfer fluid (HTF) which acts as a heat exchange substance between heat source and PCM. HTF exchanges heat to PCMs most commonly via shell and tube heat exchanger. But most of the PCMs suffer from lower thermal conductivity which makes heat transport with in the PCM a challenging task. Therefore, heat transfer enhancement becomes essential in order to efficiently store and extract thermal energy in these systems. In recent years regarding thermal energy storage PCMs have attracted much attention. **Figure: 1.2** shows the number of studies and research conducted regarding interest in thermal energy storage since last decade.
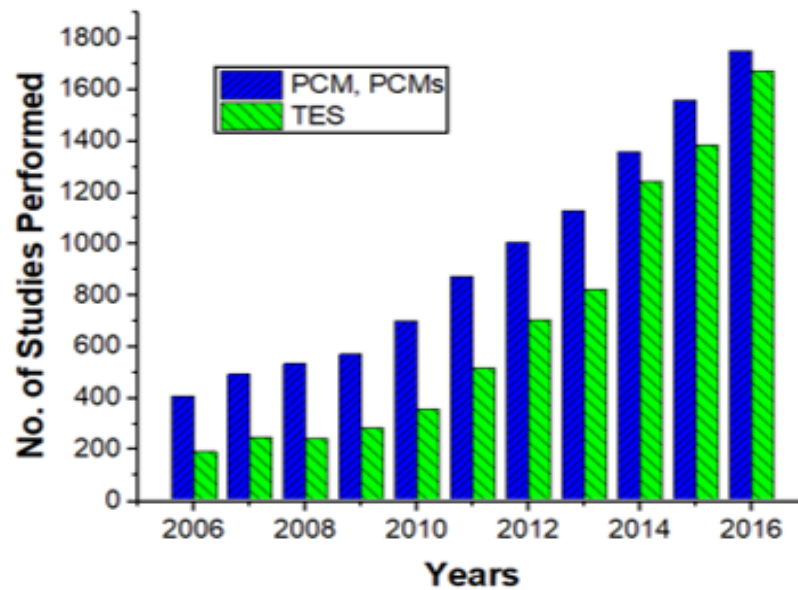
FIGURE 1.2: Literatures Retrieved by Keywords of 'PCM(s)' and 'Latent Heat Storage' from Web of Science (2006-2016) (Reproduced as it is from Zhang et.al.,[6])

In LTESS systems, PCMs store energy by phase transition such as solid to gas, liquid to gas, solid to liquid and solid to solid by applying heat equal to their phase transition temperature. Phase change systems involving gas transition are not practical because of large volumetric changes whereas, in solid-solid phase transition, crystalline structure of PCMs change which consequently result in thermal energy storage but this crystalline transition has slow rate and has low energy storage density [6]. Generally, PCMS having solid-liquid transition dominate because of their small volumetric change, they are easy to handle, high density of thermal energy and compactness [7]. Most of the known materials show solid-liquid transition but in standard applications, following properties are required for Solid-liquid transition PCMs [8],[9].

1. Thermal storage properties of PCM should include high enthalpy of phase change, high specific heat capacity and thermal conductivity with application specific melting point.

2. Physically, PCM should have high density, low vapor pressure and volumetric changes without phase separation.

3. PCM must be chemically stable, nontoxic, non-flammable, pollution free and should not cause corrosion (container or shell compatibility).

4. Crystallization rate of PCM must be sufficient with low super-cooling degree and phase transition should be reversible.

5. PCM should be abundantly available, can be recycled and has low cost.

To date, for the above given properties, no PCM fulfills all the requirements. Phase separation, supercooling, liquid leakage and low thermal conductivity are most common problems of PCMs. Hence researchers emphasized on development of such techniques to enhance these properties of PCMs in combination. Based on the melting temperatures PCMs are categorized in three forms [10]: Organics, Inorganics and Eutectics (Mixture) as shown in **Figure: 1.3**.
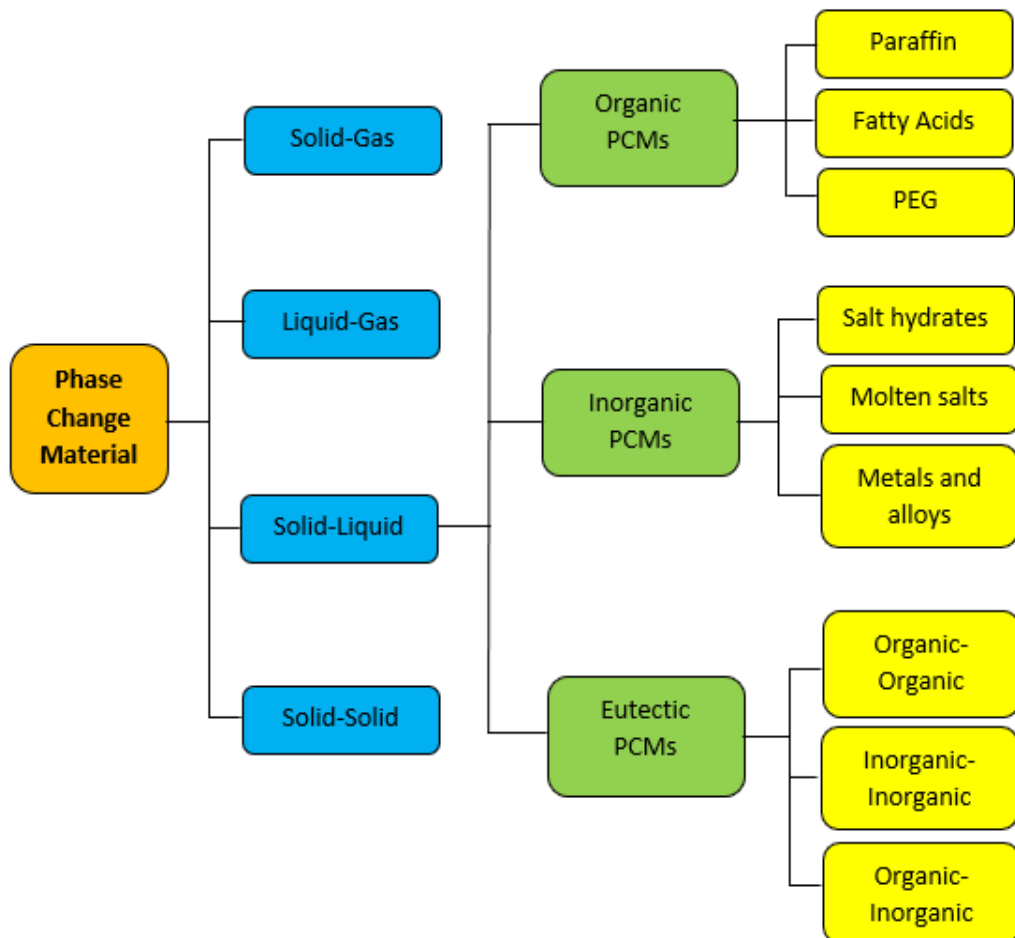


FIGURE 1.3: Classification of PCMs

Melting temperatures of organic Solid-liquid PCMs are commonly below 100°C and include paraffins, fatty acids and glycol(polyethylene) which comprise of hydrocarbons and they have wide applications in LTESS systems [11].

Further classification of inorganic Solid-liquid PCMs include salt hydrates, molten salts-alloys, metals and they have broad range of phase change temperatures.

## 1.2 Organic PCMs (Solid-Liquid)

Organic PCMs have better thermal storage properties which include congruent melting, self-nucleation, narrow ranges of phase transition, no phase separation, high thermal energy density and little or no supercooling [12].

However, their application is limited due to their leakage issues and low thermal conductivity.

### 1.2.1 Paraffin Wax

Paraffin (waxes) are chemically formed mixtures of n-alkanes denoted by $C_n H_{(2n+2)}$. They are obtained from by-products of refined crude oil. Phase transition temperatures of paraffin usually lie between 18 to 71°C [13], which are shown in **Table: 1.1**, that means these can be used for low temperature applications. Their production scales are large and comparatively in low cost than pure n-alkanes.

Chemical stability, low vapor pressure, no phase separation , self-nucleation, high latent heat density are the properties of paraffins which are desirable however, their major drawbacks include moderate flammability, low compatibility with the container, liquidity and low thermal conductivity which declare their use as a challenging task [14].

However, problem of low thermal conductivity can be resolved by using different heat transfer augmentation techniques. Which involve use of heat transfer fins, multi-tubes, inclusion of nano-particles in PCMs and shell shape modifications. These heat transfer augmentation techniques can be studied and analyzed by experimental and numerical (theoretical) approaches.

TABLE 1.1: Paraffins Thermal Properties (Reproduced as it is from Zhang et.al.,[6])

| PCMs | Phase Change Temperature °C | | Heat of Fusion (kJ/kg) | Density (kg/L) | | Thermal Conductivity (W/(m.K)) |
| | Melting | Congealing | | Solid | Liquid | |
|---|---|---|---|---|---|---|
| RT 21 | 18-23 | 22-19 | 155 | 0.88 | 0.77 | 0.2 |
| RT 22 HC | 20-23 | 23-20 | 190 | 0.76 | 0.7 | 0.2 |
| RT 24 | 21-25 | 25-21 | 160 | 0.88 | 0.77 | 0.2 |
| RT 25 | 22-26 | 26-22 | 170 | 0.88 | 0.76 | 0.2 |
| RT 26 | 25-26 | 26-25 | 180 | 0.88 | 0.75 | 0.2 |
| RT 28 HC | 27-29 | 29-27 | 250 | 0.88 | 0.77 | 0.2 |
| RT 31 | 27-33 | 33-27 | 165 | 0.88 | 0.76 | 0.2 |
| RT 35 | 29-36 | 36-31 | 160 | 0.86 | 0.77 | 0.2 |
| RT 42 | 38-43 | 43-37 | 165 | 0.88 | 0.76 | 0.2 |
| RT 44 HC | 41-44 | 44-40 | 250 | 0.8 | 0.7 | 0.2 |
| RT 47 | 41-48 | 48-41 | 165 | 0.88 | 0.77 | 0.2 |
| RT 50 | 45-51 | 51-46 | 160 | 0.88 | 0.76 | 0.2 |
| RT 54 HC | 53-54 | 54-53 | 200 | 0.85 | 0.8 | 0.2 |
| RT 55 | 51-57 | 56-57 | 170 | 0.88 | 0.77 | 0.2 |
| RT 60 | 55-61 | 61-65 | 160 | 0.88 | 0.77 | 0.2 |
| RT 62 HC | 62-63 | 62 | 260 | 0.85 | 0.84 | 0.2 |
| RT 64 HC | 63-65 | 64-61 | 250 | 0.88 | 0.78 | 0.2 |
| RT 65 | 58-65 | 65-58 | 150 | 0.88 | 0.78 | 0.2 |
| RT 69 HC | 68-70 | 69-67 | 230 | 0.94 | 0.84 | 0.2 |
| RT 70HC | 69-71 | 71-69 | 260 | 0.88 | 0.77 | 0.2 |

## 1.2.2 Fatty Acids

Carboxylic acids with chemical formula $CH_3 (CH_2)_{2n} COOH$ and long chain hydrocarbons are called as fatty acids. Their occurrence is quite abundant because they are derived from fat and oils. Capric-acid (CA), myristic-acid (MA), lauric-acid (LA), stearic-acid (SA), palmitic-acid (PA) and arachidic-acid (AA) are most commonly used PCMs. As an advantage eutectic mixture can be formed by mixing two or more fatty acids. Their phase transition temperature ranges from 16 to 74°C [15], which are also given in **Table: 1.2**.

TABLE 1.2: Thermal Properties of Fatty Acids (Reproduced as it is from Yuan et.al.,[15])

| Common Name at 20 (°C) | Melting Temperature (°C) | (Heat Storage Capacity (kJ/kg)) |
|---|---|---|
| Caprylic acid | 16.1 | 144.2 |
| Capric acid | 31.5 | 155.5 |
| Lauric acid | 43.6 | 184.4 |
| Myristic acid | 57.7 | 189.7 |
| Palmitic acid | 61.3 | 197.9 |
| Stearic acid | 66.8 | 259 |

## 1.2.3 Glycols (Polyethylene)

Glycol (Polyethylene) is a type of non-paraffin organic PCM. High heat storage capacity, bio-degradation, thermal and chemical stability, non-corrosiveness, non-toxicity, no supercooling and low vapor pressure are the favorable characteristics of PEG PCMs. Phase transition temperatures of PEGs can be altered by adjusting

their molecular weights [16]. Some thermal properties of commonly used PEGs are given in **Table: 1.3**.

TABLE 1.3: PEGs Thermal Properties (Reproduced as it is from Zhang et.al.,[6]

| PCMs | Melting Start (°C) | Peak (°C) | End (°C) | Heat Storage Capacity (J/g) |
|------|------|------|------|------|
| PEG-1000 | 19 | 45.6 | 76.7 | 78.6 |
| PEG-1500 | 33.5 | 57.3 | 87.8 | 150.1 |
| PEG-2000 | 42 | 63 | 90.9 | 163.1 |
| PEG-4000 | 45.6 | 64.7 | 93.9 | 172 |
| PEG-6000 | 46.9 | 66.7 | 94.9 | 175 |
| PEG-8000 | 47.6 | 67.7 | 97.2 | 177.2 |
| PEG-10000 | 50.3 | 69.7 | 99.5 | 191 |
| PEG-20000 | 51 | 67.7 | 95.8 | 180.5 |

## 1.3 Inorganic PCMs (Solid-Liquid)

Inorganic PCMs are categorized into salt hydrates, salts, metals and alloys [17]. Compared to the organic PCMs, inorganics PCMs have twice the capacity to store latent energy per unit volume. Low cost and high thermal conductivity are main advantages of inorganic PCMs over organic PCMs.

### 1.3.1 Salt Hydrates

Salt hydrates are formed by composition of inorganic salts and water with the chemical formula $AB.nH_2o$. Chemical bonds of water and inorganic salts are destroyed and formed by variation of temperatures. Their main process of phase transition is based on hydration and dehydration. High thermal conductivities, high heat storage capacity with little variation in volume during phase change are advantageous characteristics of salt hydrates [6]. Whereas, problems of phase

separation due to density difference during phase change, poor nucleation, super-cooling (disagreement between melting and freezing temperatures) are the short comings of these PCMs.

### 1.3.2   Molten Salts

Another kind of inorganic PCMs used in thermal energy storage are Molten salts. Based on their high melting temperature from 523 to 1953K and high heat storage capacities (68 to 1041 $Jg^{(-1)}$) these PCMs are categorized for high temperature applications [6]. They are mostly used in steam generation (high temperature) in the food industry, solar power plants and textile industry. Fluorides, nitrates, sulfates, chlorides and carbonates are some typical categories of molten salts.

### 1.3.3   Metals and Alloys

On the basis of main components, metal alloys are categorized into three types aluminum alloys, magnesium alloys and copper alloys [18]. Excellent thermal conductivities and high heat storage density per unit volume are their peculiar characteristics. Metal alloys have usually melting points higher than 300°C. Therefore, for high temperature thermal energy storage systems metal alloys are very suitable, but their major drawbacks are their instability and their toxicity.

### 1.3.4   Eutectic Mixture PCMs

Eutectic mixture PCMs are generally divided into three categories on the basis of their composition inorganic with inorganic, organic with organic and inorganic with organic. Most commonly they are used as solid-liquid PCMs. By adjusting different mass-ratios of their composition [19], their phase transition temperatures can be altered. Eutectic mixtures exhibit the same thermal properties of its constituents and they always melt and solidify without any segregation.

### 1.3.5 Heat Transfer Enhancement of PCMs (Solid-Liquid)

Low thermal conductivity is the major problem of almost all the PCMs during charging and discharging processes. As a remedy to this problem, heat transfer augmentation techniques are used. An overview such heat transfer enhancement methods are provided in **Figure: 1.4**. Some of the most probable solutions may include heat transfer fins, multiple HTF tubes (heat exchanger) , optimizing shape of shell and HTF tubes and multiple PCMs [20],[21]. The variations of chemical properties of PCMs by adding high conductivity nanoparticles [22],[23],[24] and low-density high thermal conductivity materials [25] such as metal foams also improve the heat transfer characteristics of PCMs. However, these techniques generally are not cost effective as nano particles and metal foams are difficult to produce in a controlled manner. Therefore, the geometrical optimization of the LTES system is the easiest and cost-effective technique. These heat transfer augmentation techniques can be studied and analyzed by experimental and numerical (theoretical) approaches.

### 1.3.6 Scope and Objective of this Work

In present study, triple fins horizontal shell and tube LTESS having multi HTF tubes in different shell geometries has been numerically investigated. HTF tube is split into two, three, four and five tubes with different relative positions and shell geometry is modified upon best selected tubes configurations. The effect of tube splitting and their relative positions along with shell geometry modification on melting characteristics of PCM is studied.

For this purpose, temperature distribution, energy accumulation, heat transfer rate and buoyant flow dynamics of PCM are investigated. Moreover, effect of tube material is also studied and an optimum tube material based on heat transfer augmentation rate is proposed. Furthermore, the temperature of HTF tube is systematically varied in order to investigate its effect on melting rate of PCM and thermal energy storage rate of LTESS.
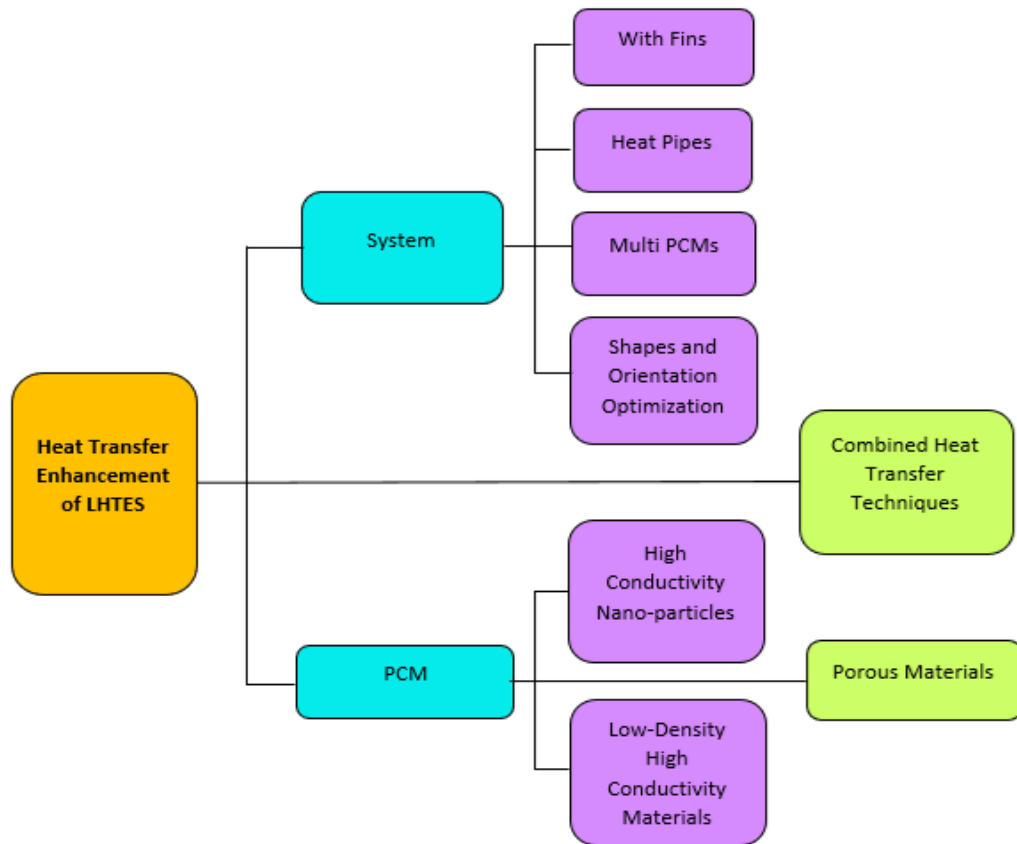
FIGURE 1.4: Heat Transfer Enhancement Techniques of LHTES System

At the end, the correlations of Fourier number and average Nusselt number are developed in terms of Stefan number and Rayleigh number, respectively, for melting of PCM.

## 1.4   Thesis Overview

Chapter 2 is about literature survey regarding phase change materials. In this chapter relevant research studies carried out so far regarding problem at hand are summarized. It includes a detailed review of techniques and methods being used to augment heat transfer characteristics of LTESS involving phase change materials.

Chapter 3 is related to numerical setup of simulation that is used for studying

phase change process of latent thermal energy storage. It consists of problem formulation along with a schematic of the computational domain. It also includes meshing strategy, boundary conditions, governing equations and Ansys Fluent setup of simulations.

Chapter 4 presents the results obtained from this numerical study. The results section is mainly divided into two sections. First section includes the analysis and study of split HTF tubes configurations and arrangements placed among LTESS for complete charging cycle. Whereas, the second section discusses the results obtained by modification of the shell geometries, which is based on the best performance split tubes configurations. Correlations are also proposed for these best configurations based on non-dimensional Stefan, Nusselt, Fourier and Rayleigh numbers.

Chapter 5 consists of conclusions of this research study. This chapter also consists of the future recommendations in the area of study under consideration in this work.

# Chapter 2

# Literature Review

The melting of PCMs involves natural convection which acts as a dominant mode of heat transfer. The buoyancy forces induce vortices in the flow which in turn increase the heat transfer rate. The orientation of heat surface plays essential role in natural convection which heat transfer rate of PCM and ultimately effects its melting time ($t_m$). However, the low thermal conductivity of PCMs makes it very difficult to augment the heat transfer. Therefore, heat transfer augmentation techniques must be involved in PCM based thermal energy storage systems.

As a remedy to poor thermal performance of shell and tube LTESS, the heat transfer enhancement in the PCM is attained by using multiple HTF tubes instead of single tube [26]. Agyenim et.al., [27] used erythritol as a PCM to experimentally investigate the thermal energy storage performance of horizontal shell and tube heat exchanger by splitting single heat transfer tube into four tubes. Temperature gradients in axial, radial and angular directions among shell and tube system were analyzed and compared. Results declared phase change enhancement of 2.5 and 3.5% in axial and radial directions, respectively. Similarly effect of inner tubes(multiple) on melting process of multi-tube heat exchanger as depicted in **Figure: 2.1 (a)**, was numerically investigated by Esapour et.al., [28] by using RT35 as a PCM. Splitting single tube into four tubes reduced the PCM melting time by 29%. Analysis was also done by varying heat transfer tubes temperatures, investigation results are shown in **Figure: 2.1 (b)**. It was concluded that by

increasing HTF temperature at inlet from 50 °C to 60 °C, melting time decreased significantly by 33 % for all the cases including the double tube and multi tubes. Melting process of RT27 (paraffin blend) as a PCM was numerically studied by Liu et.al., [29] by using various combinations of a large and small HTF tubes with different arrangements within the shell. For the multiple-tube arrangements under consideration, the effects of various numbers of multiple-tubes and diameter ratios on heat transfer were also studied. Fastest melting progression of PCM was achieved by a combination of a large and two small tubes with a diameter ratio of 2. A numerical investigation of heat transfer characteristics of LTESS with staggered and parallel configuration of HTF tubes using paraffin as PCM and air as HTF was carried out by Liu et.al., [30]. The staggered tube configuration improved the melting rate by 57% through enhanced convective heat transfer. An experimental investigation of variations of HTF temperature and mass flow rates on melting process of paraffin wax based horizontal double pipe heat storage system was carried out by Jesumathy et.al., [31] . A 2°C increase or decrease in HTF temperature at inlet enhanced melting rates by 25%.
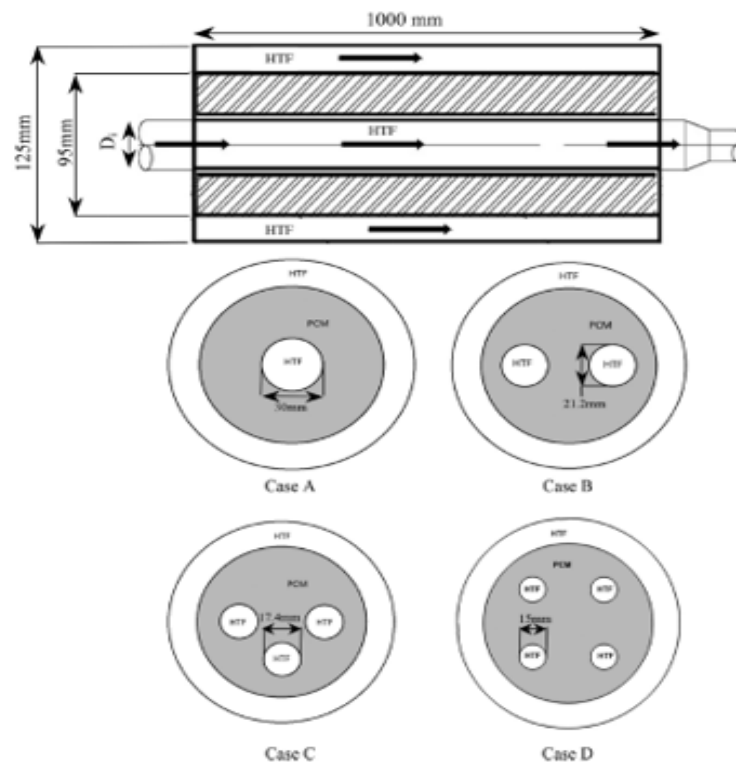


(a)
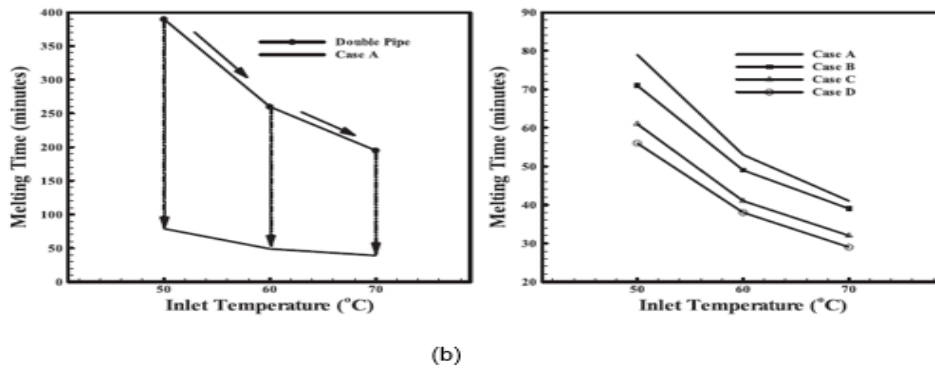
FIGURE 2.1: Physical Model and Configurations of all Multi-Tube Heat Exchangers (b)Effects of Inlet Temperatures on Melting Times (Reproduced as it is from Esapour et.al., [28])

Kousha et al., [32] experimentally investigated the melting and solidification processes of finless multi-tube heat exchanger by studying different multi tube arrangements varying from 1-4 at different HTF temperatures. Paraffin (RT-35) was used as PCM stored in cylindrical shell. In comparison to single HTF tube, four tube arrangement reduced the melting and solidification time of the system by 43 % and 50 %, respectively. Similarly, experimental study of Joybari et al ., [33] compared melting process of paraffin (RT-60) in finless single and multiple (five) tubes vertical heat exchanger configurations. The results revealed that the multi-tube configuration enhanced the convective effects and therefore accelerated the melting process of PCM. The multi-tube configuration reduced the melting time by 73.6 % as compared to single tube configuration. Although different studies pertaining to multi-tube LTESS have been performed but most of these studies do not employ fins. However, the melting process can be further accelerated by incorporating fins along with multi-tube arrangement of HTF tubes. It has been reported in the literature that the extended surfaces such as Longitudinal fins, circular fins and pin fins significantly improve the performance of LTESS [34],[35],[36],[37]. Hollow pin type fins were used by Yousaf et.al., [38] in a PCM based solar still to augment heat transfer characteristics of the system experimentally. Thermal performance of PCM based, conventional and PCM based pin finned system was quantified. They reported enhancement of 17% and 7% with the use of PCM based pinned fin system in comparison to the PCM based and conventional system, respectively. Longitudinal fins have better performance than

circular fins while charging and discharging processes of PCMs [39],[40]. Different studies performed on PCM melting investigated the effects of longitudinal fins [41], locations of fins [42] and geometrical configuration of shell [43]. They reported that increasing the thickness, length and number of fins reduced the melting time of PCM. Yang et.al., [44] numerically investigated the melting process PCM paraffin RT35 in an annularly finned horizontal LTESS. Melting behavior of PCM was analyzed by installing different number of annular fins around HTF tube. They proposed an optimum annularly finned LTESS having 31 fins and reported 65% reduction in melting time with optimum LTESS. Similarly, in a sleeve-tube horizontal LTESS, detailed numerical study was carried out by Wang et.al., [45] to analyze effect of thermo-physical and geometrical parameters on performance of LTESS as shown in **Figure: 2.2 (a)**. Fin length, fin geometry, angle between fins and different conductive shells were investigated for melting of PCM. For the given fin angles, temporal variation of liquid fraction is shown in **Figure: 2.2 (b)**. Results declared an optimal finned LTESS with fin angles of $60^0$ and $90^0$ in which melting time of PCM was reduced by 49.1%.
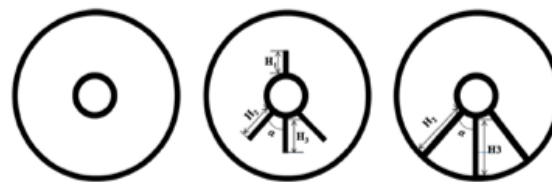


(a)
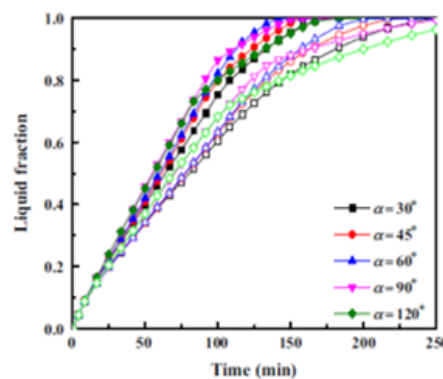


(b)

FIGURE 2.2: (a) Schematics of the Sleeve-Tube Ltes Units (B) the Time Evolution of Liquid Fraction at Different Fin Angles (Reproduced as it is from Wang et.al., [45])

Hosseini et.al., [46] performed experimental and numerical investigation to study the effect of Stefan number and fin length on the performance of LTESS. Analysis was performed for three different lengths and Stefan number. The results showed that 0.38 Stefan number and 26mm fin length enhanced melting process of the PCM and increased performance of the system by 15.3%. Rathod et.al., [47] experimentally studied the effect of longitudinal fins in a vertically oriented LTESS by using stearic acid as PCM as depicted in **Figure: 2.3**. 43.6% reduction in melting time was achieved by use of longitudinal fins. Al-Abidi et.al., [48] enhanced heat transfer of horizontal LTESS by provision of internal-external fins as shown in **Figure: 2.4 (a)**. They used paraffin RT-82 as PCM and different geometrical parameters such as fin length, fin thickness and number of internal-external fins were investigated and performance of LTESS was gauged. An optimum geometry was recommended, based on melting rate improvement, by varying different fin number combinations, lengths and thickness, as presented in Figure 8 (b). As compared to the non-finned LTESS, melting performance of the system enhanced by 43.4 % by using fins design of case G (8-Cell PCM unit geometry) as shown in **Figure: 2.4 (b)**.
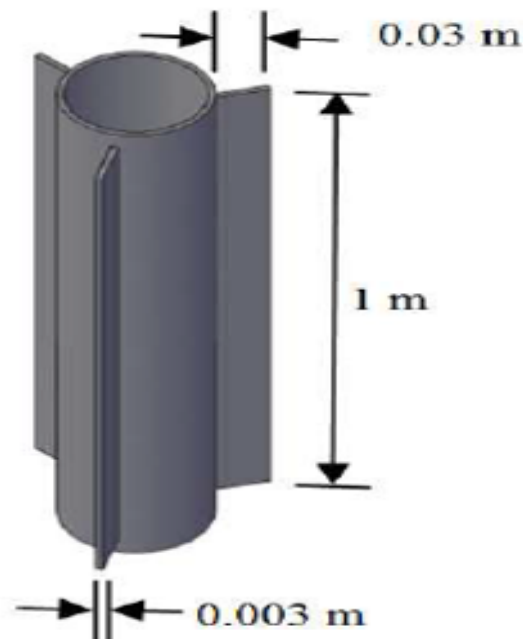


FIGURE 2.3: Schematic Diagram of HTF Unit with Fins (Reproduced as it is from Rathod et.al., [47])

(a)



(b)
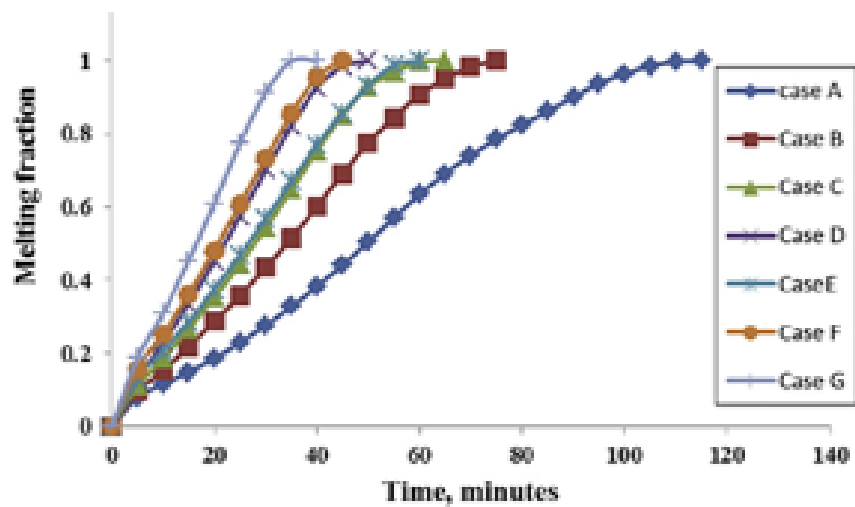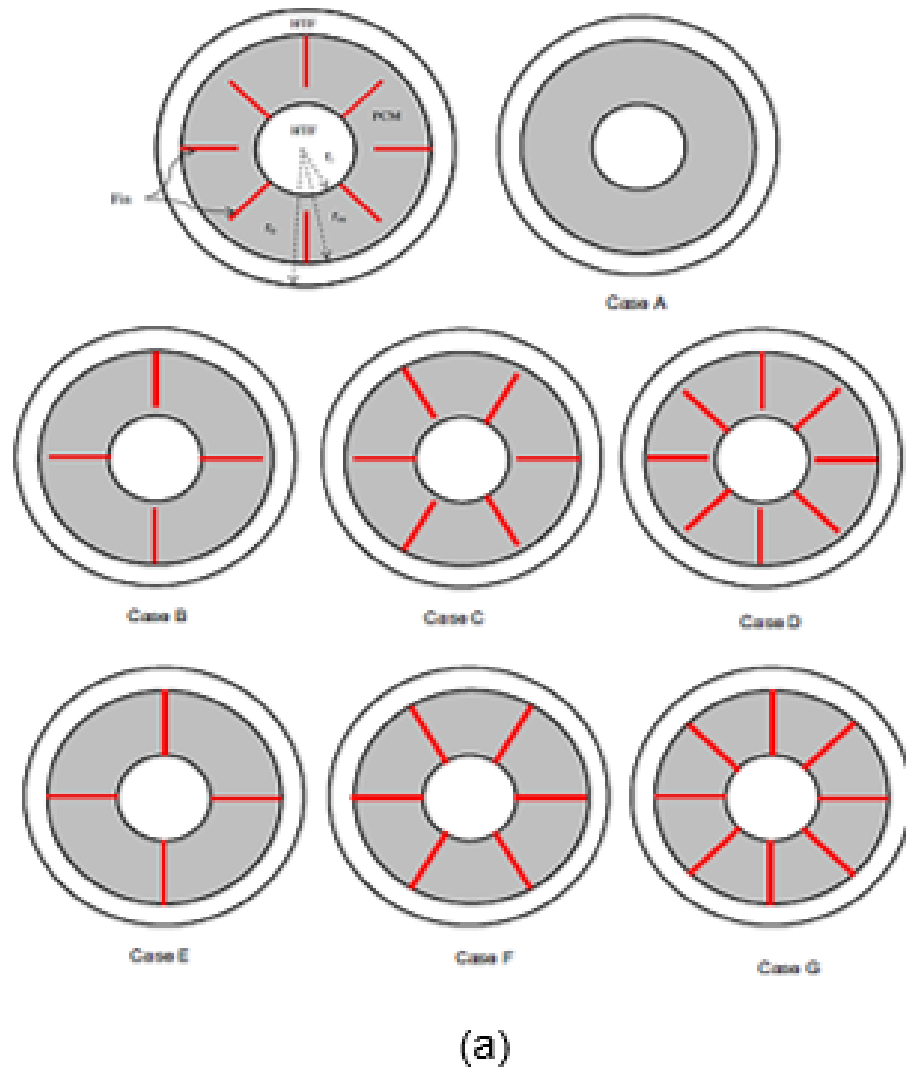
FIGURE 2.4: (a)Schematic and Physical Configuration of All Cases (b) Melting Fraction for all Enhancement Cases (Reproduced as it is from Al-Abidi et.al., [48])

Cao et.al., [49] performed numerical investigations to study the heat transfer characteristics of HTF tube with and without fins. For comparison they also increased fin number at five different constant wall temperatures to get optimum number of fins of 10, in order to augment heat transfer characteristics and heat transfer coefficient of horizontal shell and tube LTESS. For horizontal LTESS, different effects of double fin arrangement was examined by Deng et.al., [50] by placing symmetrical fins around HTF tube at six different angles. Two-dimensional transient model was used to numerically study the performance characteristics of PCM (Lauric acid) during melting process. A reduction of 50.8% in the melting time was achieved by using fin angle of 120°(optimum) with non-dimensional fin length l=$\frac{L}{r_{ori-1}}$=1 placed with fins in the base region of the cylinder, where L is the corresponding fin length, $r_o$ is the inner radius of the external shell and $r_i$ is the inner radius of internal tube. Kazemi et.al., [51] performed numerical investigations to study the effect of angle variation between fins as depicted in **Figure: 2.5 (a)**. In their investigation, three longitudinal fins were attached to the inner tube of horizontally placed LTESS filled with PCM (RT35). Simulations were performed for three 60°, 90° and 120° angles between fins. Concentration of all the fins in upper region depicted the case of smaller angle while for the case of 120°, fins were equally spread out. For different fin angles melting penetration length was quantified for analysis and was observed maximum penetration length for the case of 120° for which temporal variation of liquid fraction and heat storage rates are plotted in **Figure: 2.5 (b)**, which shows that 22.54% reduction in melting time was achieved by using fin angle of 120°.

Abdullateef et.al., [52] performed numerical and experimental investigations on triplex tube LTESS using paraffin RT82 as PCM. Improvement in thermal performance of LTESS was analyzed with internal-external longitudinal fins of triangular shape. They compared melting of PCM with and without triangular fins and reported 15% reduction in melting time by provision of internal-external triangular fins. The experimental and numerical study of Khan & Khan [53] demonstrated the importance of orientation of the longitudinal fins in shell and tube LTESS. They used stearic acid as PCM, placed in annulus of copper tube and steel shell.

The shell was insulated externally while the HTF tube was maintained at constant temperature by circulating hot water at 358 K.



(a)



(b)
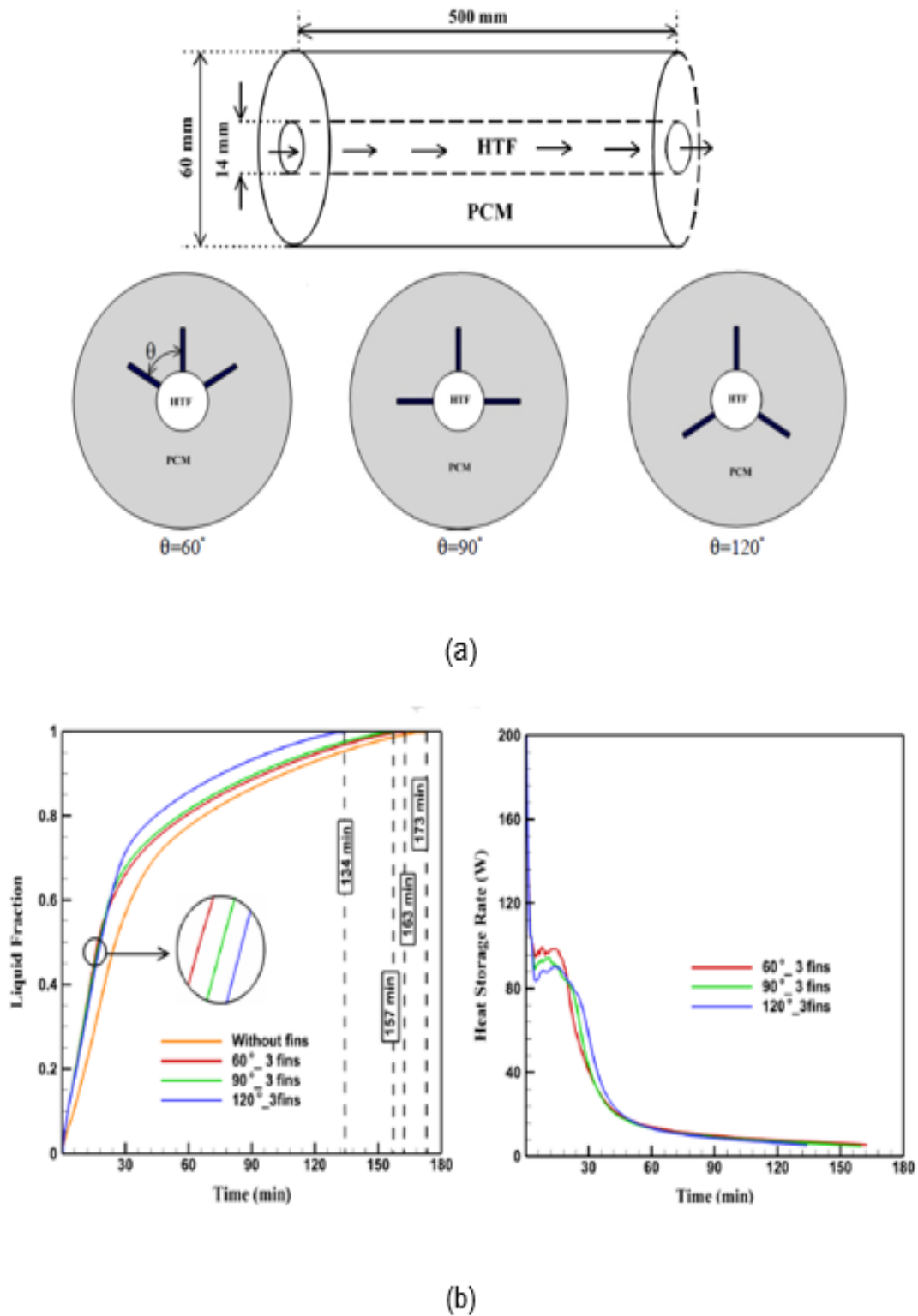
FIGURE 2.5: (a) Physical Model and Fins Arrangements of the Triple-Fins Heat Exchangers (b) Temporal Variations in Liquid-Fraction and Heat Storage Rates of Given Configurations (Reproduced as it is from Kazemi et.al., [51])

The results showed that Y-fin orientation enhanced the heat transfer rates significantly in comparison to other orientations. The Y-fin configuration reduced the melting time by more than 50% and at the same time increased the energy storage capacity by 10%. In case of multi-tube LTESS, Pizzolato et. al., [54] employed four HTF tubes and optimized the geometry of the fins based on the natural convection effects during melting and solidification of the PCM.

It was successfully demonstrated that charging and discharging process of LTESS could be significantly accelerated by employing the fins along with multiple HTF tubes. However, detailed quantitative thermal performance analysis of optimized multi-tube LTESS and the variation of multi-tube arrangements were neglected. The effectiveness of fins and heat transfer pipes during charging and discharging process of latent heat thermal energy storage unit was also experimentally studied by Robak et.al., [55] as shown in **Figure: 2.6 (a) and (b)**.

They used paraffin as PCM and results concluded that inclusion of heat pipes i.e 5 in number, enhanced melting rate by 60 %, whereas fins were not found to be significantly effective in assisting heat transfer rate. Tiari et.al., [56] performed numerical simulations to explore the effects of number of heat pipes, their spacing and fin length on thermal storage performance of potassium nitrate KNO3 (PCM), stored in a square container. It was observed that by increasing number of heat pipes from 1 to 3 (closely spaced) and using twenty fins of 35mm length, the melting rate was significantly enhanced thus reducing the charging time of the system by 30%.

Similarly, the numerical study of Bouhal et.al., [57] showed that inclusion of fins in multi-tube configuration of LTESS significantly enhanced the convective heat transfer in PCM in comparison to finless multi-tube configuration as shown in **Figure: 2.7 (a)**. They performed numerical investigations by using Gallium as PCM and four HTF tubes with longitudinal fins in a horizontal LTESS Temporal variations of liquid fractions at inlet temperatures of 40° and 45° are shown in **Figure: 2.7 (b)**, which shows that by using finned split tube heating sources among shell reduced melting time of the system by 27.24%, respectively. But at the same time, by fixing the multi-tube arrangement to a square shape, the heat

transfer rates were limited in the lower section of LTESS. Therefore, the provision of fins along with arrangement of multi-tubes play a crucial role in thermal performance enhancement of LTESS.
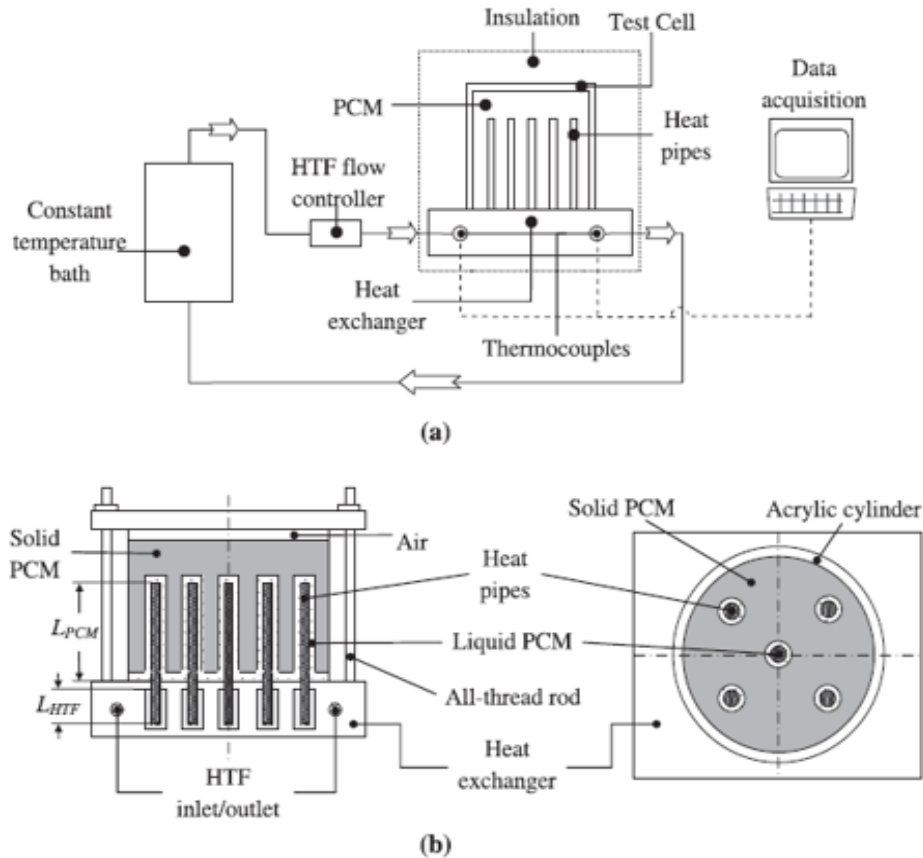


FIGURE 2.6: (a)Schematic of Overall Experimental Setup (b) Detailed Diagram (Reproduced as it is from Robak et.al., [55] )

Another important aspect of performance enhancement of LTESS in the context of arrangement of multi-tubes is the shape and design of the shell. The shape of the shell that compliments the multi-tube arrangement can significantly improve the heat transfer in PCMs as noted by Pourakabar et.al., [58]. They numerically investigated the effects on heat transfer enhancement in N-eicosane assisted by copper foam by using double and quadruple finless HTF tube arrangements in circular and elliptic shells as shown in **Figure: 2.8 (a)**. For melting process in circular shell, they identified vertical double tube arrangement as the optimum configuration while for elliptic shell, the horizontal quadruple tube arranged in diamond shape was highlighted as the optimal configuration. Temporal variation of liquid fraction during melting process is plotted in **Figure: 2.8 (b)**, which

shows that by using two tubes in vertical array enhanced melting rate up to 70%.
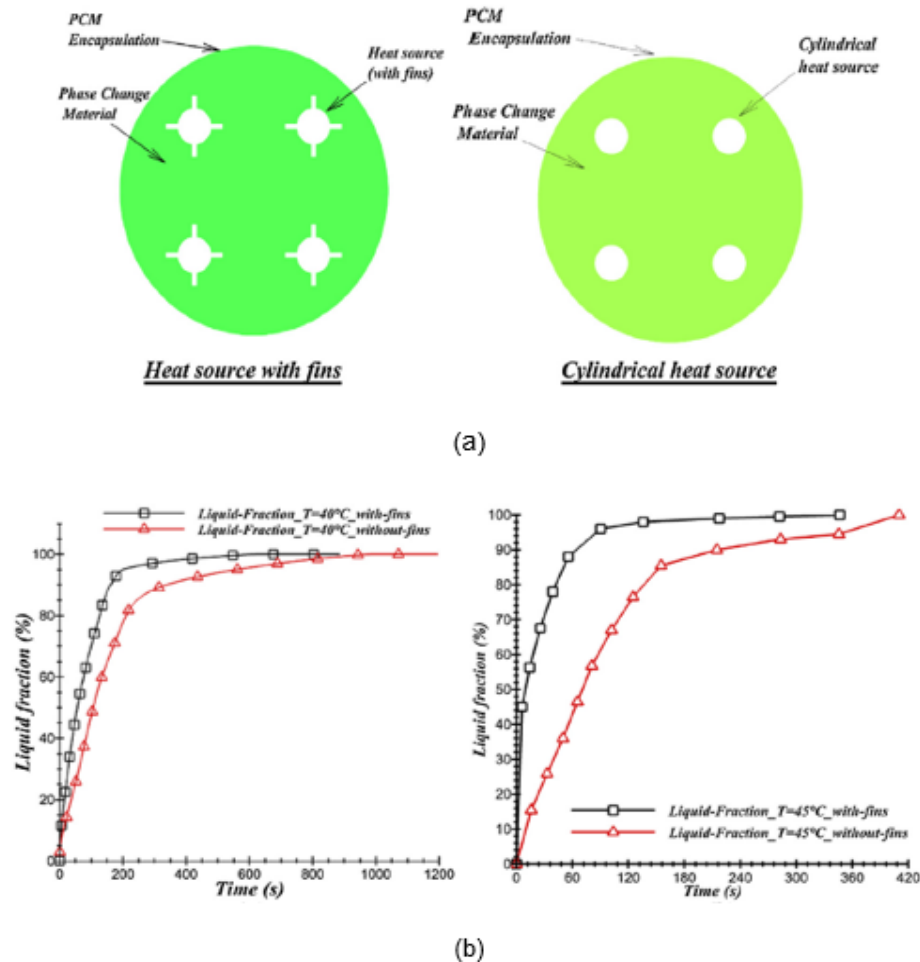


FIGURE 2.7: (a) Physical Models of Cylindrical Heating Resources with and without Fins (b) Evolution of Liquid Fractions of the Studied Configurations at HTF Temperatures 40° and 40°C (Reproduced as it is from Bouhal et.al.,[57])

Faghani et.al., [59], performed numerical simulations to analyze the effect of orientations of circular and elliptical shell and tubes on melting process of heat exchanger. A maximum of 62% reduction in melting time was attained by using elliptical HTF tube placed vertically in elliptical shell which was oriented horizontally. Shin et al., [60] experimentally studied and compared the thermal energy storage performance of spherical and elliptical LTESS by placing 1-octadecanol as PCM. Elliptical shell showed twice the increase in heat transfer rate to that of spherical shell, which consequently reduced charging and discharging times of

system by 50 % and 35 % respectively. Assis et al., [61] experimentally and numerically investigated the melting process of RT-27 (PCM) stored in spherical shells having different diameters. Results were compared for 40mm, 60mm and 80mm shell diameters which showed time saving of 61.1% achieved by shell diameter of 40mm. Li et.al., [62] numerically investigated the melting process of PCM in a spherical shell by studying the effects of the bath temperature, sphere radius, PCM thermal conduction coefficient and spherical shell material. The results showed a reduction of 45.7% in melting time by using the sphere of radius 40 mm by providing bath temperature of 60 °C.
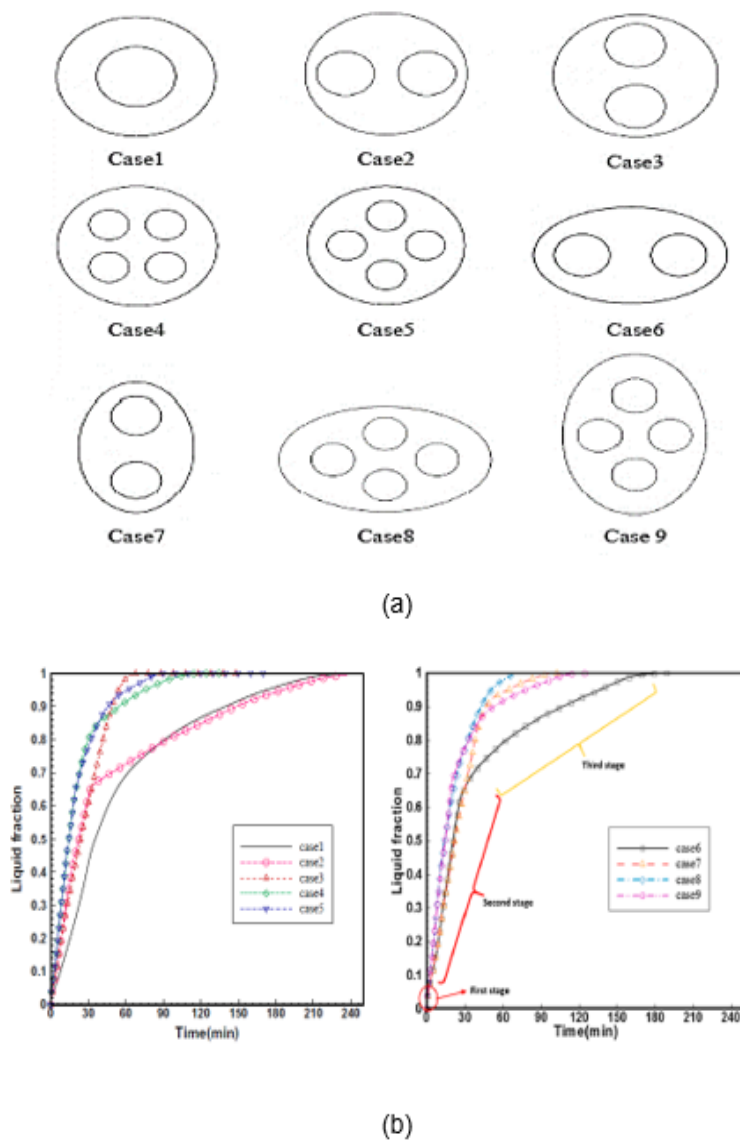


FIGURE 2.8: (a) Schematics of all Investigated Cases (b) Temporal Variation of Liquid Fraction During Melting Process (Reproduced as it is from Pourakabar et.al., [58])

To the best of author's knowledge, a systematic study on splitting of a single finned HTF tube into multiple finned tubes with different multi-tube arrangements along with complimenting shell designs has not been performed yet. A comprehensive quantitative analysis of their effect on heat transfer in the PCM, impact on the overall energy storage rate and total energy capacity of multi-tube LTESS has not been given due attention. Most of the studies deal with the random comparative analysis by predetermining the number of tubes and their arrangements. Although, some studies have focused on the improvement of shape of the shell but only limited to elliptic shells [58],[59],[60],[61]. Therefore, further possibilities of shell design are required to be explored to get maximum advantage out of the buoyancy driven convective currents. In the present study, different designs of horizontal shell and tube type LTESS having multiple HTF tubes with three fins arranged in Y-configuration in different shell geometries are numerically investigated. HTF tube is split up into two, three, four and five tubes and arranged in different configurations. The shell geometry is also modified for further performance enhancement. Effects of multiple HTF tubes in several arrangements are studied on melting characteristics of PCM along with the shell geometry modifications. For this purpose, temperature distribution, energy storage rate, heat transfer rate and flow dynamics of PCM in a LTESS are investigated. Furthermore, the HTF tube temperature is systematically varied in order to investigate its effect on heat transfer and energy storage capacity of LTESS.

# Chapter 3

# Problem Formulation

## 3.1 Domain Configuration and Thermo-Physical Properties

he computational domain of the Base Case consists of a two-dimensional cross-section of a concentric shell and tube heat exchanger as shown in **Figure: 3.1 (a) and (b)**. The tube of copper having inner diameter $D_t$=32.1mm and thickness $t_t$=3mm is placed at the center of a steel shell having inner diameter $D_s$=121mm. Three equally spaced (120°) copper fins of radial length $l_f$=36mm and thickness $t_f$=3mm are attached to the tube as shown in **Figure: 3.1 (b)**. PCM is placed between the spacing of shell and tube. As a phase change material stearic acid is selected as a suitable choice because of its non-toxicity, non-corrosiveness and low melting temperature. During phase change process stearic acid is found to remain thermally and chemically stable. All thermo-physical properties of stearic acid (PCM) are given in **Table: 3.1**. In the current study for shell, tubes and fins, the thermo-physical properties of different materials studied are shown in **Table: 3.2** Seven different bifurcated tubes configurations, shown in **Figure: 3.2**, are investigated in this study. Single concentric tube (Base Case) is split systematically into two, three, four and five tubes which have different configurations. All the dimensions of different multi-tube arrangements are presented in **Table: 3.3**. The

cross-sectional area of HTF tube for any given configuration is calculated by dividing cross-sectional area of Base Case tube ($\text{Ac}_{(t,BC)}$) with number tubes of that given configuration ($N_t$). The length of fins of different configurations are varied while keeping the thickness of the fins ($t_t$) as constant to 3mm. The length of fin of any given case is calculated by dividing the length of the fin of Base Case ($l_f$) by number of tubes of that given case ($N_t$). The diameter of the shell of the Base Case is 121mm. The cross-sectional area of the shell is kept constant for each of the multi-tube configuration. In case 1,2 and 3 two split tubes are placed vertically, horizontally and diagonally. Case 4 and 5 have three tubes in $\Lambda$ and $\Lambda$ arrangements, respectively. Case 6 has four tubes placed in square orientation and case 7 has five tubes placed in cross configuration. In order to keep the quantity of PCM constant, the total surface area of each configuration is kept constant. Thickness of fins for all the cases is also kept constant i.e $t_t$=3mm. Fins for all the cases are arranged in Y configuration having $\Theta$=120° Y configuration shows superior performance characteristics [53]. Hence, single HTF tube with Y-fins configuration is used as Base Case in this study.
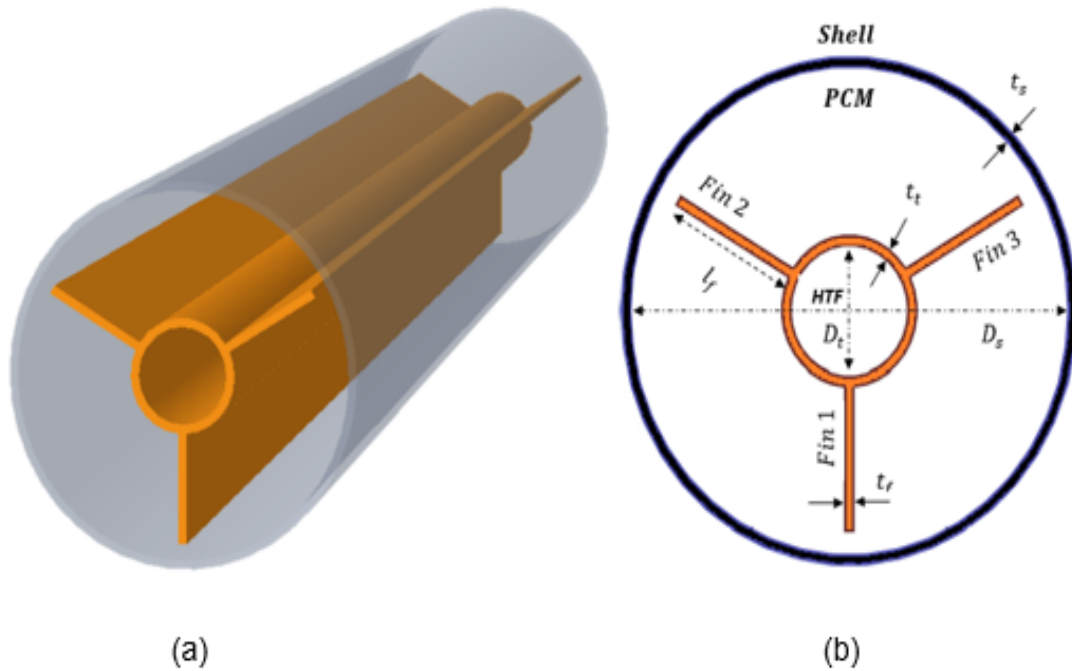


FIGURE 3.1: Computational Domain of LTESS (a) 3-D Model (b) 2-D Cross-Section
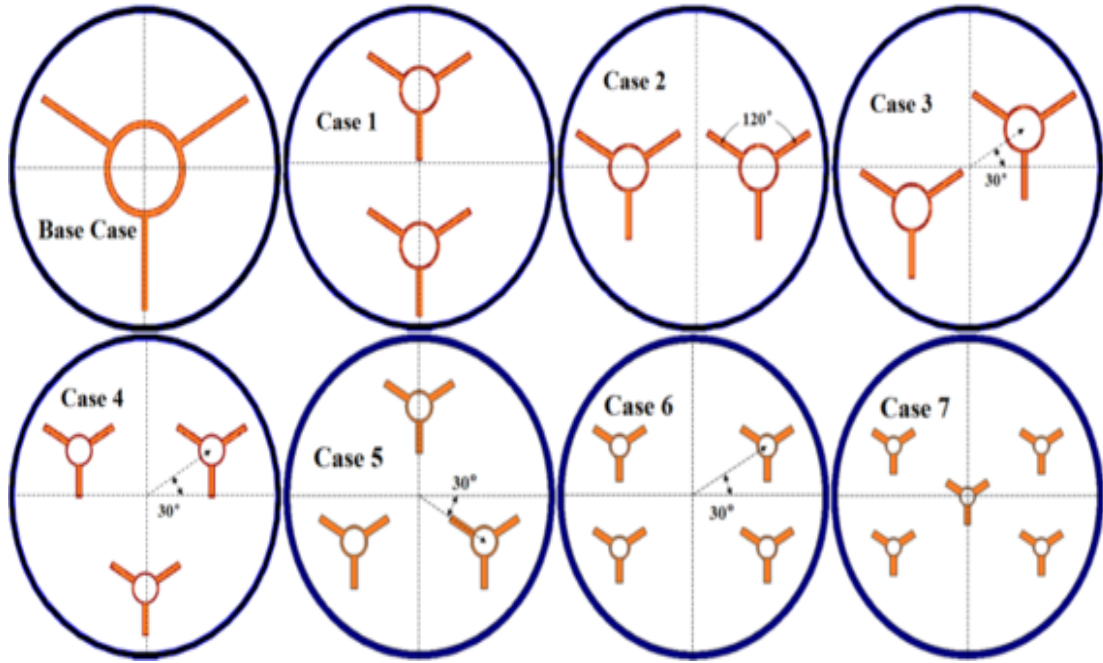
FIGURE 3.2: Schematics of the Base Case and Multitube Cases

## 3.2 Simplifications and Assumptions

In this study, the radiation heat transfer is considered negligible as compared to the effects of natural convection. The outer shell of the LTESS is considered as adiabatic, whereas, the inner surface of the HTF tube is considered isothermal. The buoyancy source term in the governing equations accounts for the density variation effects through Boussinesq approximation.

It allows the density to be treated as mean constant density in the governing equations. Consequently, the change in volume during the phase change process can be neglected. Therefore, 2D, constant PCM volume, enthalpy porosity numerical methodology is adopted to resolve the problem [63]. This approach has been validated against the complex 3D, variable PCM volume, Volume of Fluid approach [64].

Moreover, in this approach instead of explicitly tracking melting interface, the mushy zone as the mixture of solid and liquid PCM is solved in each cell. The solid-liquid mushy zone is treated as a porous medium with porosity equal to the fraction of liquid PCM in each cell. Therefore, the porosity of PCM increases from

0 to 1 as the PCM changes its phase from solid to liquid. When the PCM is solid in a cell the porosity and velocity are considered as zero.

TABLE 3.1: Thermo-Physical Properties of Materials (Reproduced as it is from Khan et.al., [53])

| Properties | Steel | Copper | Stearic Acid |
|---|---|---|---|
| Thermal Conductivity, k(W/m.K) | 16.27 | 387.6 | 0.29 |
| Dynamic Viscosity, $\mu$(kg/m.s) | - | - | 0.0078 |
| Coefficient of thermal expansion, $\beta$(1/K) | - | - | 0.0008 |
| PCM Solidus Temperature, $T_s$(K) | - | - | 327 |
| PCM Liquidus Temperature, $T_l$(K) | - | - | 337 |
| PCM Density, solid, $\rho_s$ (kg/m$^3$) | 8030 | 8798 | 1150 |
| PCM Density, liquid, $\rho_l$(kg/m$^3$) | - | - | 1008 |
| PCM Specific heat, solid, C$\rho_s$ (J/kgk) | 502.5 | 381 | 2830 |
| PCM Specific heat, liquid, C$\rho_l$ (J/kgk) | - | - | 2380 |
| Latent heat of fusion, $L_f$ (kj/kg) | - | - | 186.5 |

TABLE 3.2: Thermo-Physical Properties of Aluminium, Steel, Copper and Brass (Reproduced as it is from Khan et.al., [53])

| Properties | Aluminium | Steel | Copper | Brass |
|---|---|---|---|---|
| Thermal Conductivity (W/m.K) | 202.4 | 16.27 | 387.6 | 109 |
| Density (kg/m$^3$) | 2179 | 8030 | 8798 | 8700 |
| Specific heat (J/kgK) | 871 | 502.5 | 381 | 400 |
| Thermal diffusivity (mm$^2$/s) | 106.6 | 4.03 | 115.6 | 31.3 |
| Thermal effusivity (W/cm$^2$Ks$^{-0.5}$) | 1.96 | 0.81 | 3.61 | 1.95 |

TABLE 3.3: Splitting Criteria of Multi Tubes Cases

| Case | No. of Tubes ($N_t$) | Orientation | Area of Each Tube ($A_{ct,BC}/N_t$) | Tube Diameter ($D_t$) | Total Number of Fins | Length of each Fin ($l_f/N_t$) |
|------|------|------|------|------|------|------|
| Base | 1 | Concentric | **808.871 mm$^2$** | **32.1mm** | 3 | **36mm** |
| 1 | 2 | Vertical | 404.435 mm$^2$ | 22.698 mm | 6 | 18mm |
| 2 | 2 | Horizontal | 404.435 mm$^2$ | 22.698 mm | 6 | 18mm |
| 3 | 2 | Diagonal | 404.435 mm$^2$ | 22.698 mm | 6 | 18mm |
| 4 | 3 | V | 269.623 mm$^2$ | 18.532mm | 9 | 12mm |
| 5 | 3 | Λ | 269.623 mm$^2$ | 18.532mm | 9 | 12mm |
| 6 | 4 | Square | 202.217 m$m^2$ | 16.049mm | 12 | 9mm |
| 7 | 5 | Cross | 161.774 mm$^2$ | 14.355 mm | 15 | 7.2mm |

## 3.3 Numerical Modelling

The buoyancy driven flow during the charging process is produced due to density variation between liquid and solid phases of phase change material. The incompressible, unsteady, laminar flow in this process is described by Continuity equation, Momentum equation and Energy equation which are presented in **eq. (3.1), eq. (3.2) and eq. (3.3)**, respectively.

$$\frac{\partial \rho}{\partial_t} + \frac{\partial \mu_i}{\partial \chi_i} = 0 \tag{3.1}$$

$$\frac{\partial \rho \mu_i}{\partial_t} + \frac{\partial \rho \mu_i \mu_i}{\partial \chi_i} = -\frac{\partial \rho}{\partial \chi_i} = \mu \frac{\partial^2 \mu_i}{\partial \chi_j^2} + \rho g_i + F_i \tag{3.2}$$

$$\frac{\partial \rho h}{\partial_t} + \frac{\partial \rho \mu_i h}{\partial \chi_i} = \frac{\partial}{\partial \chi_i} k \frac{\partial T}{\partial \chi_i} \tag{3.3}$$

Where $\mu$ shows the velocity of the PCM in liquid state, $\mu$ is described as dynamic viscosity, $\rho$ defines the pressure, $\rho$ denotes the density, $g$ is the gravity, and $F_i$ represents the source term for momentum. The momentum source term $F_i$ incorporates the effect of momentum variation of liquid PCM due to buoyancy. According to Darcy's law [51], the source term for momentum could be considered simply as a momentum damping term, as modelled in **eq. (3.4)**.

$$F_i = A_{Mushy} \frac{(1 - \alpha)^2}{\alpha^3 + \xi} \mu_i \tag{3.4}$$

During the phase transition process of PCM, a mushy zone is considered which encompasses both liquid and solid phases of PCM. The velocity damping in mushy zone is controlled by mushy zone constant $A_{Mushy}$ which generally varies between $10^4$ to $10^7$. The larger values of $A_{Mushy}$ induces higher velocity damping which can cause large fluctuations while calculating the solution. In this study, the suitable value of $A_{Mushy}=10^5$ is attained through comparison of experimental and numerical results. A small number $\xi=0.001$ is added in the denominator to $\alpha^3$ in order to avoid the source term to become infinite at $\alpha=0$.

Natural convection is induced in PCM due to density variation caused by temperature difference and gravity. Therefore, variation in density is attained by using Boussinesq model which treats density as function of temperature and is also applicable where natural convection effects are present. In Boussinesq model variation in density are presented as $\rho=\rho_l \diagup (\beta(\text{T-T}_l)+1)$, where $(\beta)$ is thermal

expansion coefficient, $\rho_1$ denotes PCM liquidus density and (T-T$_l$ ) accounts for temperature difference between liquidus temperature of PCM and tube temperature. Moreover, k in **eq. (3.3)** denotes the thermal conductivity, h shows enthalpy and T represents the temperature. Enthalpy of PCM is calculated in three stages with respect to phase of the PCM, (i) when PCM is in sold state below the liquidus temperature (ii) when PCM is neither completely solid nor liquid (iii) when PCM is completely liquid. Variations of enthalpy during above three stages is mathematically represented as shown in **eq. (3.5)**.

$$h = \begin{cases} \int_{T_R}^{T} C_{pS} dT, & T < T_S \\ \int_{T_R}^{T_S} C_{ps} dT + \alpha h_\Delta, & T_S < T < T_S \\ \int_{T_R}^{T} C_{ps} dT + h_\Delta + \int_{T_l}^{T} C_{pl} dT, & T > T_l \end{cases} \tag{3.5}$$

Where $T_R$ is reference temperature taken as $300K$ in present study, $C_{ps}$ and C$_{p1}$ are specific heat of solid and liquid PCM respectively and h$\Delta$ is the PCM latent heat. The variation in $C_p$ between liquid and solid phases of PCM could be taken as linear Rathod et al. [47]. The PCM melting is quantitatively measured in terms of melting fraction denoted by $\alpha$. Melting fraction is calculated by following mathematical relationship in **eq.(3.6)**.

$$h = \alpha = \frac{h_\Delta}{L_f} = \begin{cases} 0 & T < T_S \\ \dfrac{T - T_S}{T_l - T_S} & T_S < T < T_S \\ 1 & T > T_l \end{cases} \tag{3.6}$$

Material enthalpy is calculated by taking sum of sensible enthalpy, h, and latent heat, $\Delta$ H:

$$H = h + \Delta H \tag{3.7}$$

where

$$h = h_{ref} + \int_{T_{ref}}^{T} C_p dT \tag{3.8}$$

and

h$_{ref}$=reference enthalpy

T$_{ref}$=reference temperature

c$_p$=specific heat at constant pressure

The liquid fraction, $\alpha$, can be defined as:

$$\alpha = 0 \, if \, T < T_{solidus} \tag{3.9}$$

$$\alpha = 1 \, if \, T > T_{solidus} \tag{3.10}$$

$$\alpha = \frac{T - T_{solidus}}{T_{solidus} - T_{solidus}} if \, T_{solidus} < T < T_{solidus} \tag{3.11}$$

The latent heat content can be written in the form of latent heat of the material, L:

$$\Delta H = \alpha L \tag{3.12}$$

Latent heat content varies between L (for a liquid) and zero (for a solid).

For melting/solidification problems, energy equation can be written as;

$$\frac{\partial}{\partial_t}(\rho H) + \nabla.(\rho \vec{\nu} H) = \nabla.(k\nabla T) + X \tag{3.13}$$

Where

H=enthalpy

$\rho$=density

$\vec{\nu}$=fluid velocity

X=source term.

## 3.4   Discretization and Interpolation Schemes

The numerical discretization of the governing equations is performed using

Finite Volume Methods in Ansys Fluent 19.0$^\odot$. The spatial discretization of the governing equations requires discretization of diffusive and convective part of the governing equations. The diffusion part of the equations is approximated by second order central differencing scheme, whereas, for convective part, third order MUSCL scheme is employed. MUSCL scheme incorporates central differencing and upwind scheme ensures stability and accuracy of the solution in high convection zones. Pressure velocity coupling is solved by SIMPLE (Semi-Implicit Partially Linked Equations) and the pressure interpolations at the cell faces is performed by PRESTO scheme. Second order implicit scheme is used to perform temporal discretization because of its unconditional stability. The under-relaxation factors used for these computations are 0.3, 1, 1, 0.7, 0.9 and 1 for pressure, density, body forces, momentum, liquid fraction update and energy respectively. For suitable accuracy of solution, convergence criteria is selected to be $10^{-6}$. A brief detail of the schemes and models is described below:

### 3.4.1 Second-Order Upwind Scheme

In order to achieve second order accuracy, multidimensional linear reconstruction approach [65] is used to compute quantities stored at cell faces. In this approach, higher order accuracy is attained at cell faces through a Taylor series expansion of the cell centered solution about the cell centroid. Hence, by selecting second order upwind, the cell face value $\phi_f$ is calculated using the following expression.

$$\varphi_{f,SOU} = \varphi + \nabla\varphi.\overrightarrow{\Upsilon} \tag{3.14}$$

Where $\phi$ and $\Delta\phi$ are the cell centered values and their gradient in upstream cell, and $\overrightarrow{\Upsilon}$ is the displacement vector from the upstream cell centroid to the face centroid as shown in **Figure: 3.3**. In each cell, the gradient $\Delta\phi$ is required to be determined in this formulation by using following methods [66]:

- Green Gauss Cell-Based

- Green Gauss Node-Based

- Least Squares Cell-Based

Second-order upwind is available in the density-based and pressure-based solvers.

## 3.4.2 Third-Order MUSCL Scheme

Third-Oder MUSCL scheme is derived from the original MUSCL (Monotone Upstream-Centered Scheme for Conservation Laws) by adding a blending function into second order upwind scheme and central differencing scheme.

$$\varphi_f = \theta\varphi_{f,CD} + 1(1 - \theta)\varphi_{f,SOU} \tag{3.15}$$

Where $\phi_{f,CD}$ is calculated by using central differencing scheme

$$\varphi_{f,CD} = \frac{1}{2}(\varphi_o + \varphi_1) + \frac{1}{2}(\nabla\varphi_o.\overrightarrow{\Upsilon_0} + \nabla\varphi_1.\overrightarrow{\Upsilon_1}) \tag{3.16}$$

The indices 0 and 1 refer to the cells that have faces f,$\Delta\varphi_0$ and $\Delta\varphi_1$are the reconstructed gradients at cells 0 and 1, and $\overrightarrow{\Upsilon}$ is the vector directed from the cell centroid toward the face centroid as shown in **Figure: 3.3**.

$\varphi_{f,SOU}$ is calculated by second order upwind scheme;

$$\varphi_{f,SOU} = \varphi + \nabla\varphi.\overrightarrow{\Upsilon} \tag{3.17}$$

Where $\varphi$ and $\Delta\varphi$ are the cell centered values and their gradient in upstream cell, and $\overrightarrow{\Upsilon}$ is the displacement vector from the upstream cell centroid to the face centroid.

Central differencing scheme can produce non-physical wiggles and unbounded solutions, which can therefore lead to stability problems and compared to the second order upwind scheme, Third-Order MUSCL potentially improves spatial accuracy by reducing numerical diffusion for all types of meshes [66].
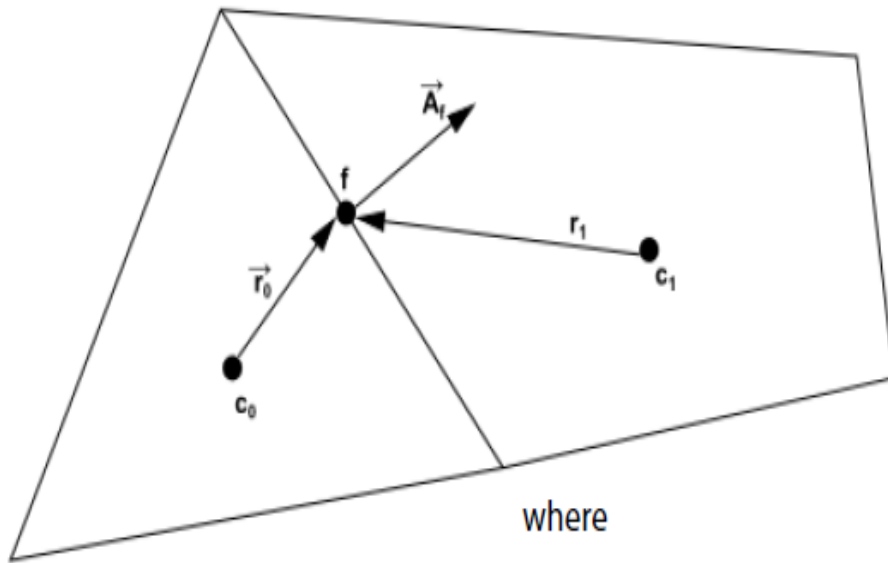
where

$\varphi_f$ = value of $\varphi$ convected through face $f$

$\vec{A}_f$ = area vector of face $f$,

$\nabla\varphi_f$ = gradient of $\varphi$ at face $f$

FIGURE 3.3: Control Volume used to Illustrate Discretization of Scheme (Reproduced as it is from Ansys Fluent R19 Guide [66])

### 3.4.3   Pressure Velocity Coupling Using SIMPLE Algorithm

In SIMPLE (Semi-Implicit Partially Linked Equations) algorithm, relationship between pressure and velocity corrections are used to solve for mass conservation in order to get pressure field.

Face Flux $J_f^*$, is calculated by solving for momentum equation with a guessed pressure filed p*.

$$J_f^* = \widehat{J}_f^* + d_f(p_{c0}^* - p_{c1}^*) \tag{3.18}$$

In order to satisfy the continuity equation, a correction factor $J_f^*$ is added to the face flux $J_f^*$, hence the corrected face flux, $J_f$ becomes;

$$J_f = J_f^* + J_f' \tag{3.19}$$

For SIMPLE algorithm $J'_f$ is postulated as

$$J'_f = d_f(p'_{c0} - p'_{c1}) \tag{3.20}$$

Where $p'$ is the pressure correction for the cell.

### 3.4.4   Pressure Interpolation Scheme

Momentum equations are discretized by solving for the pressure values stored at each cell face of control volume. Interpolation is performed on the cell faces using centered cell values stored at the center. Whereas, pressure-staggered discretization scheme calculates the pressure values stored at the face. This is solved by using staggered grids where pressure and velocity variables are not co-located. More accurate results are obtained by PRESTO discretization since pressure gradient assumptions and interpolation errors on boundaries are avoided [67].

### 3.4.5   Second Order Implicit Temporal Discretization Scheme

Transient simulations involve both temporal and spatial discretization of governing equations. In temporal discretization, every given term of a governing equation is integrated over a time step $\Delta t$. For second order implicit time discretization, any independent variable could be discretized in time as:

$$\frac{\partial \varphi}{\partial_t} = \frac{\varphi_{n+\frac{1}{2}} - \varphi_{n-\frac{1}{2}}}{d_t} \tag{3.21}$$

$$\varphi_{n+\frac{1}{2}} = \varphi_{n+\frac{1}{2}} \gamma_{n+\frac{1}{2}} (\varphi_n - \varphi_{n-1}) \tag{3.22}$$

$$\varphi_{n-\frac{1}{2}} = \varphi_{n-1+\frac{1}{2}} \gamma_{n-\frac{1}{2}} (\varphi_{n-1} - \varphi_{n-2}) \tag{3.23}$$

Where n,n-1,n-2, n+$\frac{1}{2}$,n-$\frac{1}{2}$ are different time levels.

$\gamma_{n+\frac{1}{2}}$ and $\gamma_{n-\frac{1}{2}}$ are bounding factors for each variable at the $n + \frac{1}{2}$ and $n - \frac{1}{2}$ level. Bounded variables include Volume fraction in case of multiphase flows while turbulence kinetic energy, dissipation rate, specific dissipation rate in case of turbulent flows.

### 3.4.6  Least Squares Cell-Based Gradient Evaluation

The gradients are required for constructing scalar values at cell faces and to calculate derivatives of velocity and secondary diffusion terms. In this method it is assumed that solution varies linearly. From the centroid of the cell c0 to cell ci as shown in **Figure: 3.4**, the change in cell values between cell c0 and c$_i$ along the vector $\delta_{ri}$ can be expressed as:

$$(\nabla \varphi)_{c0}.\nabla r_i = (\varphi_{ci} - \varphi_{c0}) \tag{3.24}$$
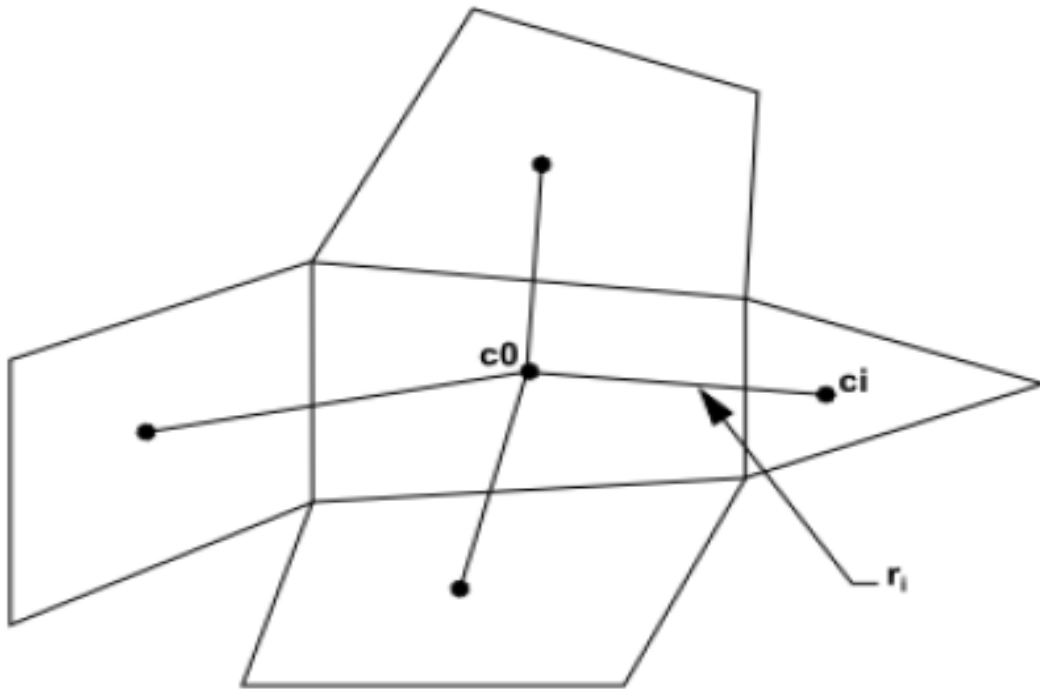


FIGURE 3.4:  Evaluation of Cell Centroid (Reproduced as it is from Ansys Fluent R19 Guide [66])

For each surrounding cell $c_0$, similar equations can be written in compact form:

$$[J](\nabla \varphi)_{c0} = \Delta \varphi \tag{3.25}$$

In the above equation [J] is the coefficient matrix that is a geometric function. To determine the cell gradient ($\nabla_0 = \varphi_x \hat{l} + \varphi_y \hat{j} + \varphi_z \hat{k}$), minimization problem for the system is solved of the non-square coefficient matrix in a least square sense. The above system of linear equations can be solved by decomposing the coefficient matrix which yields a matrix of weights having three components ($W_{i0}^x, W_{i0}^y, W_{i0}^y$) for each cell c0. Therefore, the gradients at the cell centers can be calculated by multiplying the weight factors by the difference vector $\Delta \varphi = (\varphi_{c1} - \varphi_{c0})$,

$$(\varphi_x)_{c0} = \sum_{i=1}^{n} W_{i0}^x . (\varphi_{ci} - \varphi_{c0}) \tag{3.26}$$

$$(\varphi_y)_{c0} = \sum_{i=1}^{n} W_{i0}^y . (\varphi_{ci} - \varphi_{c0}) \tag{3.27}$$

$$(\varphi_z)_{c0} = \sum_{i=1}^{n} W_{i0}^z . (\varphi_{ci} - \varphi_{c0}) \tag{3.28}$$

## 3.5   Important Non-Dimensional Numbers

The important non-dimensional numbers such as, Nusselt number (Nu), Rayleigh number (Ra), Stefan Number (Ste) and Fourier number (Fo) are presented below:

$$Nu = \frac{hD_t}{k_{PCM}}; \tag{3.29}$$

Ste is the ratio of sensible heat to latent heat

$$Ste = \frac{Cp_l(T_{HTF} - T_l)}{L_f}; \tag{3.30}$$

Whereas, Ra is the ratio of buoyancy to viscous forces,

$$Ra = \frac{g\beta(T_{HTF} - T_l)D_t^3}{nu_l(a_{th})_l};$$

(3.31)

and Fo is the ratio of the heat conduction rate to the thermal energy storage rate.

$$F_o = \frac{(k/\rho_l C_{pl})t}{D^2}$$

(3.32)

## 3.6 Initial and Boundary Conditions

The boundary conditions employed in the simulations are presented in **Figure: 3.5**. The inner surface of the HTF (Heat Transfer Fluid) tube is maintained at constant temperature at $T_t$=358 K.

The variation of temperature of the PCM is linked to the variation of temperature of the outer surface of HTF tube by applying coupled boundary condition. Initially, the tube outer surface of heat transfer tube is provided with the temperature of 303 K which is same as that of initial temperature of solid PCM ($T_{PCM}$ (t=0)).

At the shell inner wall, conduction boundary condition is applied. The shell outer surface of LTESS is considered as adiabatic. For the outer surface of the heat transfer tube and inner surface of the shell no slip boundary condition is used.

## 3.7 Grid and Time-Step Independence

In order to avoid numerical errors in the simulation results, time-step independence and grid convergence studies are performed. Four different structured grid resolutions named as Grid 1, Grid 2, Grid 3 and Grid 4 consisting of 10k, 12k, 15k and 20k computational cells, respectively, are investigated for the Base Case.
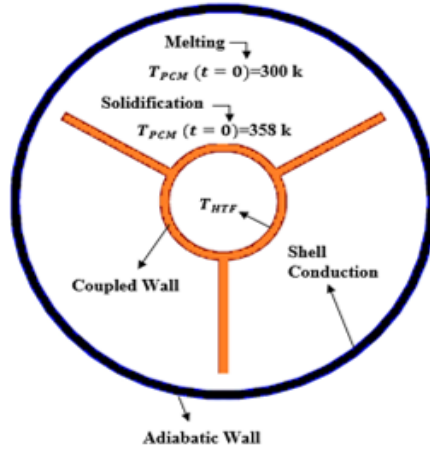
FIGURE 3.5: Boundary Conditions

For all the four grids, temporal variation of melting fraction is shown in **Figure:
3.6**. The results show that after 30 mins the melting fractions start to deviate.
The maximum difference between the melting fraction results for Grid 1 and Grid
4 is 4% while for Grid 3 and Grid 4, this difference difference is less than 2%.
Therefore, Grid 3 with 15k computational cells is selected for the current study.
To investigate the time-step size effects on the solution, comparisons of 0.05s,0.10s,
0.20s, 0.25s and 0.30s are performed. With the current methodology, time-step size
up to 0.25s keeps the solution stable without any significant variation. However,
some instabilities are observed in simulations for time steps size greater than 0.25s.
Hence, time-step size of 0.10s is selected for the current study which provides
reasonable accuracy without increase in the computational cost.
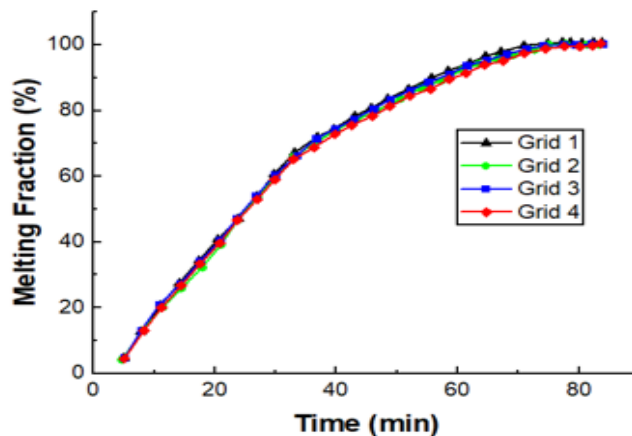


FIGURE 3.6: Melting Fraction (%) Plotted Against Time for Different Grid
Resolutions

# 3.8 Verification and Validation of Numerical Methodology

## 3.8.1 Experimental Setup

The experimental setup of the Base Case LTESS is shown in **Figure: 3.7**, It consists of a shell and tube type LTESS with three longitudinal fins installed in Y-configuration, cold water reservoir, hot water reservoir with electric coils heater, circulation pump for hot water, temperature controller (electronic), flow rate meter and manually operated flow control valves. Water is used as heat transfer fluid (HTF) whereas stearic acid is used as PCM.

To ensure fully developed flow at the inlet of the LTESS, HTF tube length is extended enough at the inlet. A constant temperature of HTF is maintained by using three 1.5kW heating elements each of which is attached to temperature controller. Hot water is circulated through the HTF tube using 372 W pump providing a flowrate of 0.441 kg/s having variation of $\pm$ 0.018 kgs$^{(-1)}$ .

The temperature of the PCM is measured at two different cross sections by placing six k-type thermocouples with an error in range of $\pm 1$ K at a distance of 25 mm from the shell in between the fins as shown in **Figure: 3.7 (a)**. The temperature drop across the LTESS is measured by installing two additional thermocouples at the outlet and inlet of the heat storage system. The accuracies of temperature controllers and thermistor (temperature control of reservoir) are $\pm$ 0.1K and $\pm$ 0.5K.

# 3.9 Comparison of Experimental and Numerical Results

It is important first to justify the assumption of simulating LTESS as a 2-D model. Therefore, for Base Case the temperature differences of the HTF at the inlet and outlet of the HTF tube are experimentally recorded during melting of PCM.

(a)

1,2,3,4,5 Manually operated valves
6. Geyser inlet
7. Geyser outlet
8. Cold water storage
9. Thermocouple module
10. Thermocouples (TC1...TC10)

11. Temperature controller
12. Rota meter
13. Thermocouple readings
14. PCM inlet vent
15. PCM outlet vent
16. Circulation pump
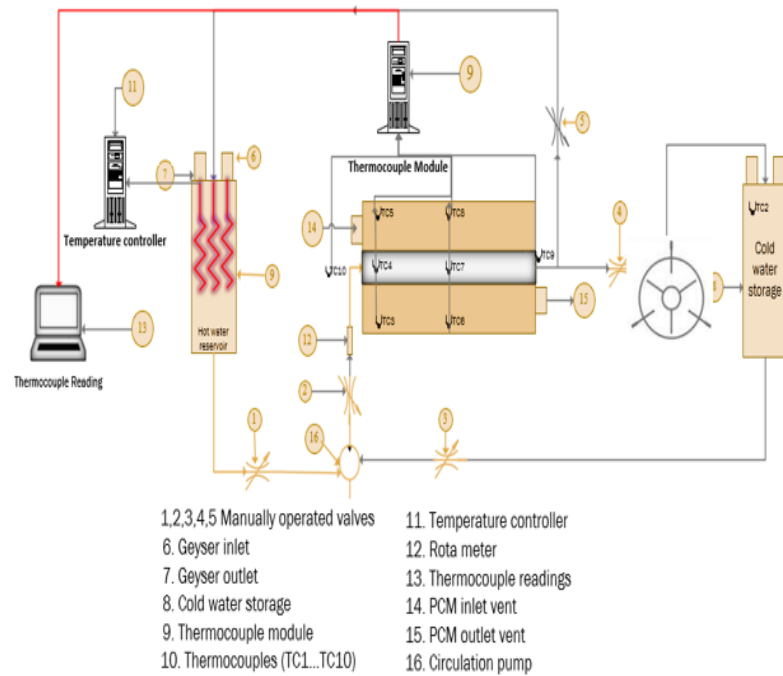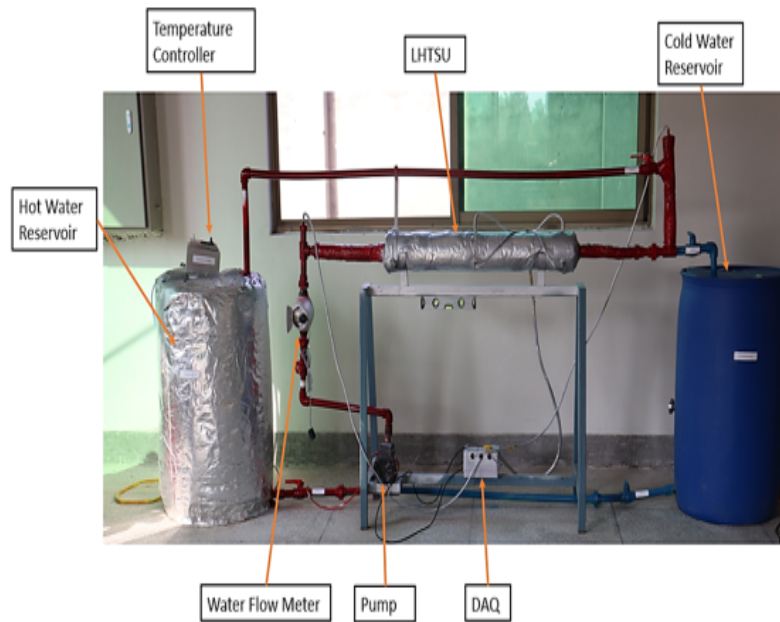


(b)

FIGURE 3.7: (A) Schematic of the Experimental Setup (B) Physical Setup of the Experimental Facility

Average temperatures at inlet and outlet of HTF tube for the Base Case are shown in **Figure: 3.8** that remains almost constant at 358K. For t < 5min, it is observed

that the maximum instantaneous temperature difference between the inlet and outlet of HTF tube is 4 K. This initial axial temperature drop across the HTF tube occurs due to the large temperature gradient available between the internal and external surface of HTF due to the presence of solid PCM. For t > 5min, the axial temperature drop becomes relatively small due to the formation of an envelope of melted PCM around the external surface of HTF tube. Therefore, for the complete cycle, the average variation in the temperature difference is ±0.51 K which is within the error range of ±1 K of thermocouples. Therefore, the variation of HTF temperature in the axial direction can be neglected and consequently the consideration of two-dimensional numerical analysis of LTESS is justified.

Another vital aspect to be considered is the total heat loss from the LTESS. The heat loss from the LTESS is calculated by considering the radial conduction through the shell and insulation along with external convection due to ambient air. The thickness of steel shell and glass wool are 3mm and 40mm. The ambient heat transfer coefficient is considered to be 5W\m²k. The maximum heat loss from the system will occur when fully melted PCM is at a steady state HTF temperature. Therefore, the maximum heat loss at the steady state temperature is calculated to 67.9 kJ at a rate of 18.8W. Considering that the latent heat of fusion of stearic acid is 186.5 kJ/kg, the total heat loss of LTESS is relatively small. Pressure drop in a straight pipe section can be calculated through major loss relationship [68].

$$\Delta p = f \frac{l}{D} \frac{\rho V^2}{2} \tag{3.33}$$

Where density, $\rho$ of water as HTF is taken as 968.61 kg\m³ at 85 $°C$ and friction factor f for a smooth pipe is calculated using explicit modified Colebrook Formula given as

$$\frac{1}{\sqrt{f}} = -1.8 log \left[ (\frac{\varepsilon \setminus D}{3.7})^{1.11} + \frac{6.9}{Ra} \right] \tag{3.34}$$

**Table: 3.4** shows the pressure drop across different split tube arrangements. It can be seen that by increasing the number of tubes pressure drop also increases which will result in requirement of more pumping power in order to keep the desired flowrate (372 W) as of single tube configuration.

For 5 split tubes configuration, pressure drop is maximum which is equivalent to 12.975 Watts, that shows additional requirement of pumping power over 372 Watts for the existing system.
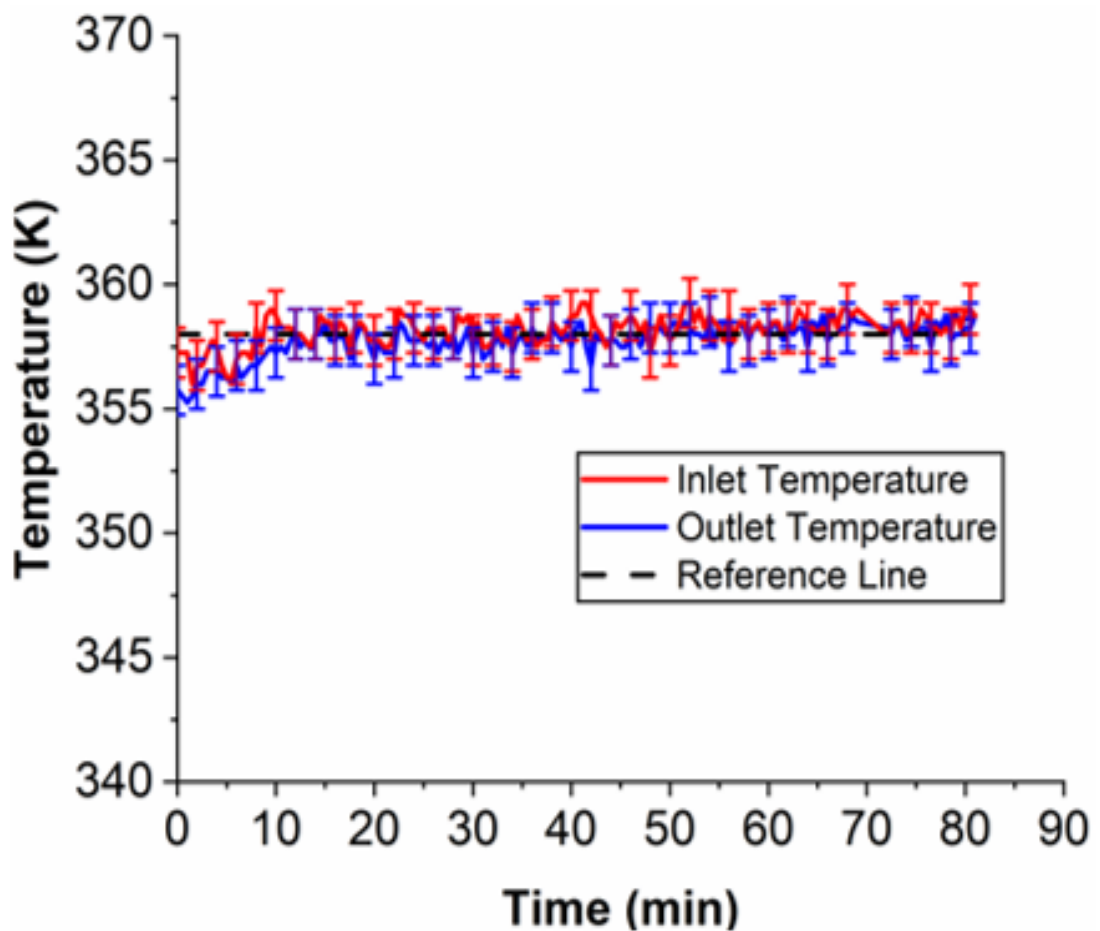


FIGURE 3.8: Experimental Results of Temperatures at Inlet and Outlet for Base Case

To validate the numerical methodology, present numerical results are compared with the results of experiments obtained for the Base Case for HTF temperature of 358 K as shown in **Figure: 3.9**. During simulations, numerical data is recorded at three temperatures probes positioned in LTESS imitating the thermocouples locations of the experimental setup. The simulation results for the melting fraction and average temperature show good comparison with the results obtained by experiments. Initially, rise of temperature is gradual but linear due to weak effects of natural convection. At t=15 min, a maximum temperature difference of 1.1% can be observed between numerical and experimental results.

TABLE 3.4: Experimental Results Of Inlet and Outlet Temperatures for Base Case

| Case | No. of Tubes | Area of Each Tube | Tube Diameter | Flow Velocity | Reynolds No. (Ra) | Friction Factor (f) | Pressure Drop | Total Power Loss (Watts) | % Power Loss |
|------|------|------|------|------|------|------|------|------|------|
|      |      | 11 | 11 | 11 |      |      | 11 |      |      |
| Base | 1 | 808.871 | 0.0321 | 0.5628 | 19,664 | 0.026 | 123.61 | 0.056 | 0.02 |
| 1 | 2 | 404.435 | 0.0227 | 1.1257 | 27,809 | 0.024 | 642.07 | 0.585 | 0.16 |
| 2 | 2 | 404.435 | 0.0227 | 1.1257 | 27,809 | 0.024 | 642.07 | 0.585 | 0.16 |
| 3 | 2 | 404.435 | 0.0227 | 1.1257 | 27,809 | 0.024 | 642.07 | 0.585 | 0.16 |
| 4 | 3 | 269.623 | 0.01853 | 1.6887 | 34,061 | 0.023 | 1,686.35 | 2.303 | 0.62 |
| 5 | 3 | 269.623 | 0.01853 | 1.6887 | 34,061 | 0.023 | 1,686.35 | 2.303 | 0.62 |
| 6 | 4 | 202.217 | 0.01605 | 2.251 | 39,331 | 0.022 | 3,347.73 | 6.097 | 1.64 |
| 7 | 5 | 161.774 | 0.01436 | 2.814 | 43,972 | 0.021 | 5,699.57 | 12.975 | 3.49 |

This difference diminishes to 0.8% at t=20 min and subsequently to 0.4% at t=25 min. For the initial 25 minutes, melting fraction remains zero in both experimental and numerical results because temperature is below the PCM liquidus temperature at the measurement locations. However, at t > 25 mins, a sudden increase in the temperature for both numerical and experimental results is observed due to dominating effects of convection in the upper half region of LTESS which subsequently augments the PCM melting rate. At this point, the numerical results compare reasonably well to experimental results.
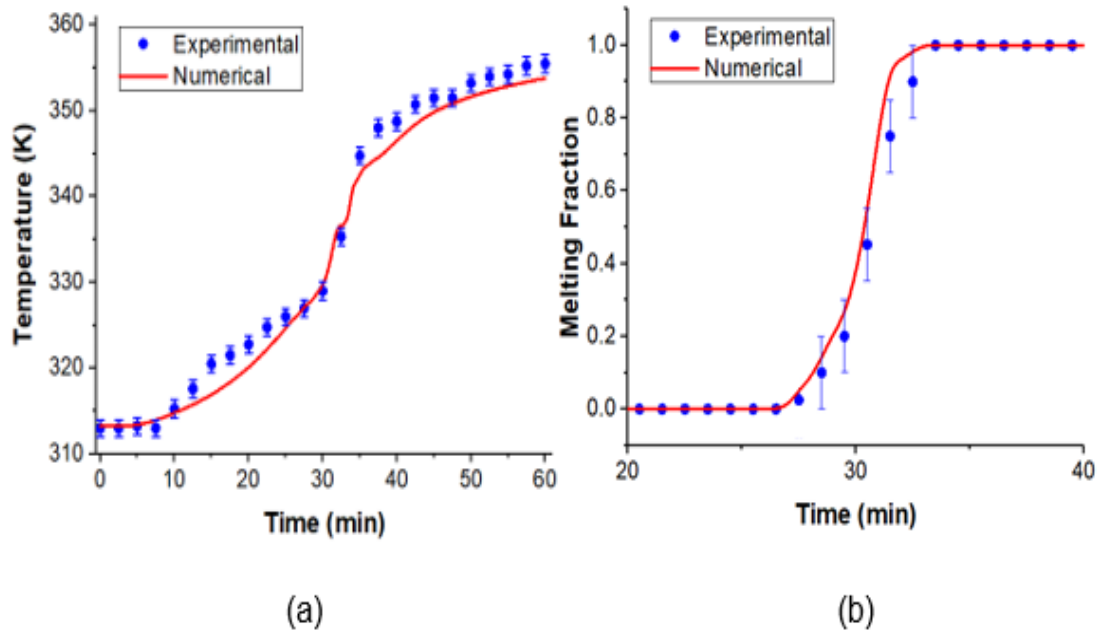
FIGURE 3.9: Comparison of Experimental and Numerical Results of (A) Average Temperature (B) Melting Fraction for the Base Case LTESS

After the complete melting of PCM in the upper half region of LTESS, rise of temperature becomes slower due to weak natural convection effects in the lower half portion of LTESS. The complete melting process at the given locations occur at $25 < t < 35$. The accurate prediction of the melting process by numerical computations validates the adopted numerical methodology.

## 3.10 Results Comparison with Literature

For further validation of our numerical methodology adopted in this study, results are compared to those in literature. Numerical results of Al- Abidi et al.,[69] are compared with the current methodology for the melting fraction. They used RT82 as a PCM which was placed in the annulus of copper shell in a horizontal LTESS. Temperature of 300K is provided to the PCM contained in shell whereas constant temperature of 363K is applied at copper tube containing HTF. Comparison of results of current methodology with the results of Al- Abidi et al. ,[69] are shown in **Figure: 3.10 (a)**, which match with Al- Abidi et.al., [69] showing reasonable

accuracy.

To predict accuracy, current numerical methodology is validated with experimental results of Gau et. al., [70] for studying melting characteristics with consideration of natural convection. Gallium is used as PCM contained in a rectangular cavity whose width and height are 90mm and 45mm respectively.

Thermophysical properties of Gallium are taken from ref [71]. Initial temperature of the gallium is 2K below the melting temperature and left wall is kept at constant temperature of 8K higher than melting temperature of gallium.

The temporal evolution of the shape of the melting front is recorded at three different time intervals as presented in **Figure 3.10 (b)**. It can be observed that both numerical methodologies over predict the melting front propagation in comparison to experimental results. This discrepancy is attributed to the fact that the desired wall temperature was not attained for first quarter of the total melting time during the experiments [72] which induced a lag in the melting front. However, the overall trend of the melting front is captured accurately by the present numerical methodology as compared to both experiments and numerical results of [73,70].
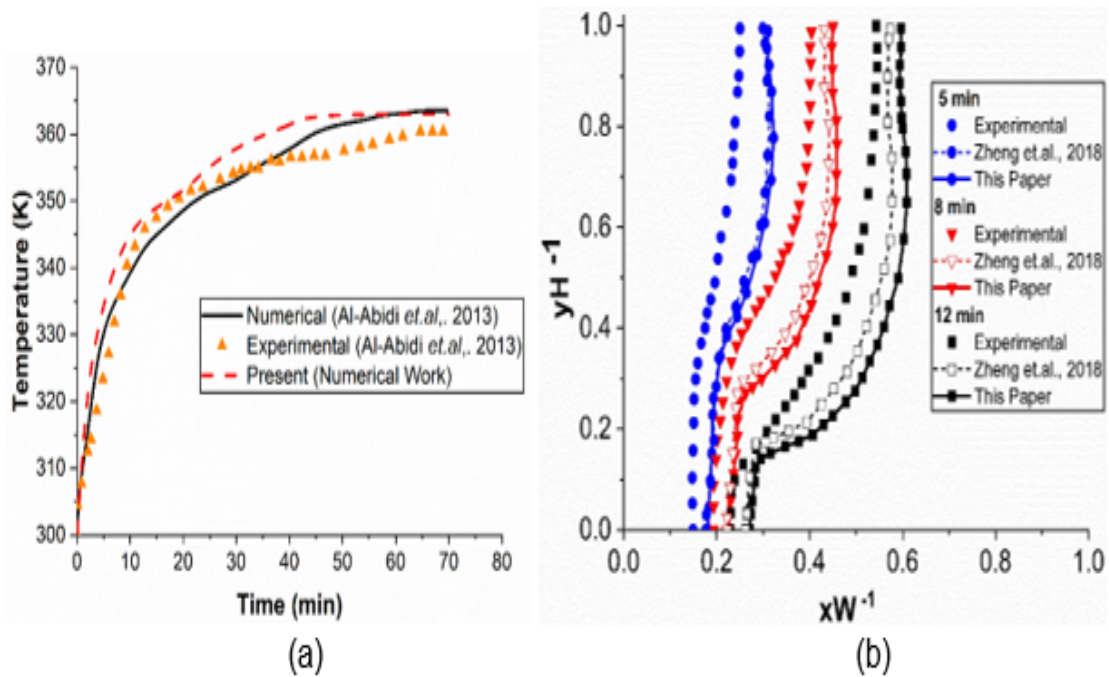


FIGURE 3.10: Present Numerical Methodology Validation with Literature (A) Melting Fraction (B) Interface Capturing Capability

# Chapter 4

# Results and Discussion

## 4.1 Splitting of Heat Transfer Tubes

In this study, the effects of the splitting of HTF tube on the thermal performance of shell and tube LTESS are investigated. The HTF tube is split into a number of smaller tubes keeping the PCM volume constant and arranged in different patterns inside a cylindrical shell. Different performance indicators are defined to analyze the performance of the proposed multitube designs on the melting enhancement by comparing the results against the base case.

### 4.1.1 Effect of Splitting Tubes on Melting Process

Temporal variation of the melting fraction for cases 1 - 7 is presented in **Figure: 4.1**. During the initial stages, i.e., t < 5 mins, all the cases have almost identical melting fractions and equal to that of the base case because conduction is the dominant mode of heat transfer from HTF tube to the solid PCM. After 5 mins, all the multitube cases start to perform better resulting in the higher melting fractions despite the fact that the heat transfer is still by conduction. The reason being the several heat sources distributed inside the shell at different locations. A noticeable increase in the melting rate is observed for the multitube tube cases during 10 < t

49

< 30 mins because the convective currents developed in the melted PCM agitates the melting PCM front and therefore enhance the melting process. More the number of tubes, stronger are the convection currents and faster is the melting. The melted PCM starts rising towards the shell due to buoyancy effects forming the convection circulation zones, which subsequently melts the whole PCM quickly in the upper portion of the shell. The portion of the shell below the HTF tubes is still a pool of high density solid PCM. This instance is defined as Inflection Point almost at t=30 min for Base Case. The inflection points of each multi-tube case is different and falls within the time interval of 20 min<t<40 min as highlighted in zoomed-in portion in **Figure 4.1**. After this point the melting rates slow down as represented by the decreased slopes of the melting fraction lines for all the cases because conduction is again the dominant mode of heat transfer. It is observed that the melting rates of the multi-tube cases decrease drastically as compared to the Base Case except for the cases 1 and 4. This is due to the fact that the fin lengths for the multitube cases are smaller as compared to the base case in order to keep the PCM volume constant. Cases 1 and 4 have HTF tubes situated in the lower portion of the shell with the fin extended near to the shell as it is in the base case. For the rest of the multitube cases the lower portion of the shell is neither having any HTF tube nor any fin to melt it, therefore, it takes long time to melt the pool of solid PCM there through conduction. Although, all the multitube cases perform better during the convection dominated heat transfer region but after the inflection point the melting rates of these cases are so slow that their total melting time increase as compared to the base case except for the cases 1 and 4 as shown in **Figure: 4.2**. It is shown that case 1 and case 4 completed their melting in 60 and 65 mins, respectively, which is a considerable gain as compared to the melting time of the base case i.e. 83 mins. Hence, case 1 and case 4 are selected as the optimum cases to further explore the improvement avenues.

It is important to appreciate the significance of the arrangement of multiple tubes because the contact area between the PCM and HTF tubes increase by a factor of $\sqrt{N_t}$ As$_{(t,BC)}$-N$_t$ $(3t_f\text{L})$. However, melting rate of Case 6 and Case 7 reduce in comparison to Case 1 and 4, regardless of increase in their surface area. The

Case 1, 2 and 3 have same surface area but the performance of Case 1 is superior to other cases. Similarly, Case 4 enhances the melting process significantly in comparison to Case 5. Therefore, the placement of HTF split tubes play a very important role in thermal energy storage performance of LTESS.
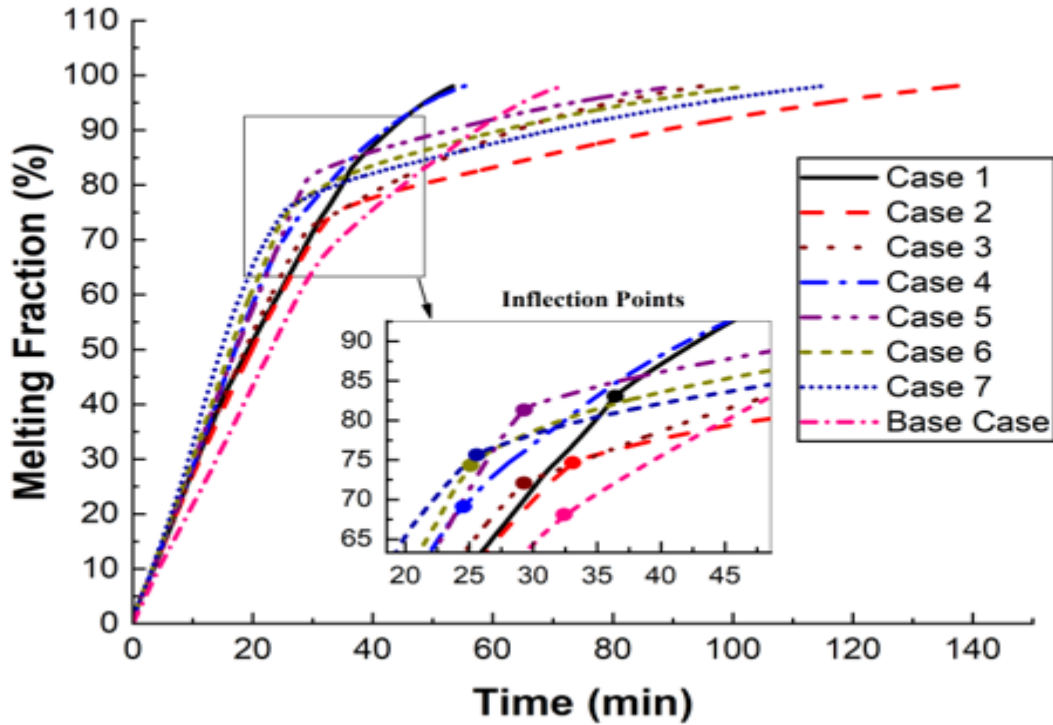


FIGURE 4.1: Comparison of Melting Fraction

To get a further insight into the melting phenomena, the contour plots of melting fraction for all multitube cases are shown in **Figure: 4.3** along with the base case at different time instances during the PCM melting. Each column represents a separate case whereas rows represent different time instances. At t=8.33 mins, heat is conducted from the walls of tubes and fins to the solid PCM resulting in its melting. The molten PCM forms a thin layer which envelopes the heat transfer surfaces. At t=16.66 mins natural convection starts to assist heat transfer process resulting in the rise of melted PCM due to buoyancy effect. The convection effects accelerate the melting process and by the time t=33.33 mins all the PCM in the upper portion of the shell, i.e., above the HTF tubes, gets melted for all the cases. This is referred to as inflection point in **Figure: 4.1**, after which the remaining PCM in the lower portion of shell gets melted due to conduction heat transfer.

The base case has a fin extended in the lower portion of the shell which assists in the melting of solid PCM settling down. Similarly, for cases 1 and 4 designs, HTF tube with fins located in the lower portion of the shell melt the solid PCM by conduction heat transfer faster as compared to the base case. For rest of the cases, there is no heat transfer surface, i.e., neither HTF tube nor a fin, extending directly into the lower pool of solid PCM. Therefore it takes long time, more than the base case, to completely melt the PCM in lower portion for these cases as shown in **Figure: 4.2**.
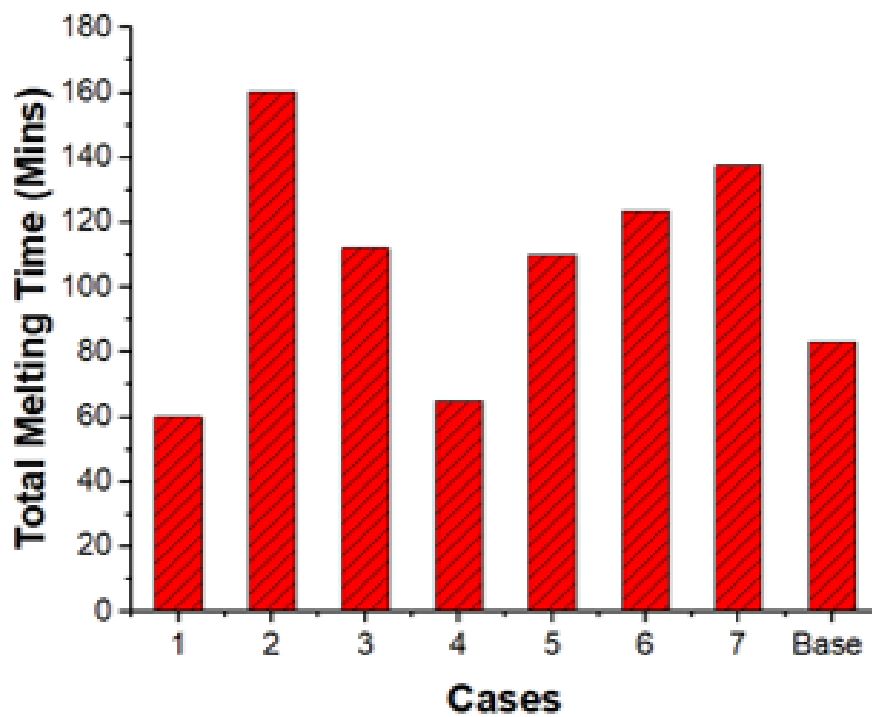


FIGURE 4.2: Complete Melting Time

## 4.1.2 Effect of Multiple Htf Tubes on Temperature Distribution

Time-based variations of the average temperature of phase change material for the base case and the seven multitube cases are shown in **Figure: 4.4**. It is observed that for very short initial times the average temperature rise of the PCM is same for all the cases. After that period, i.e., t > 5 min, a variation is observed in the
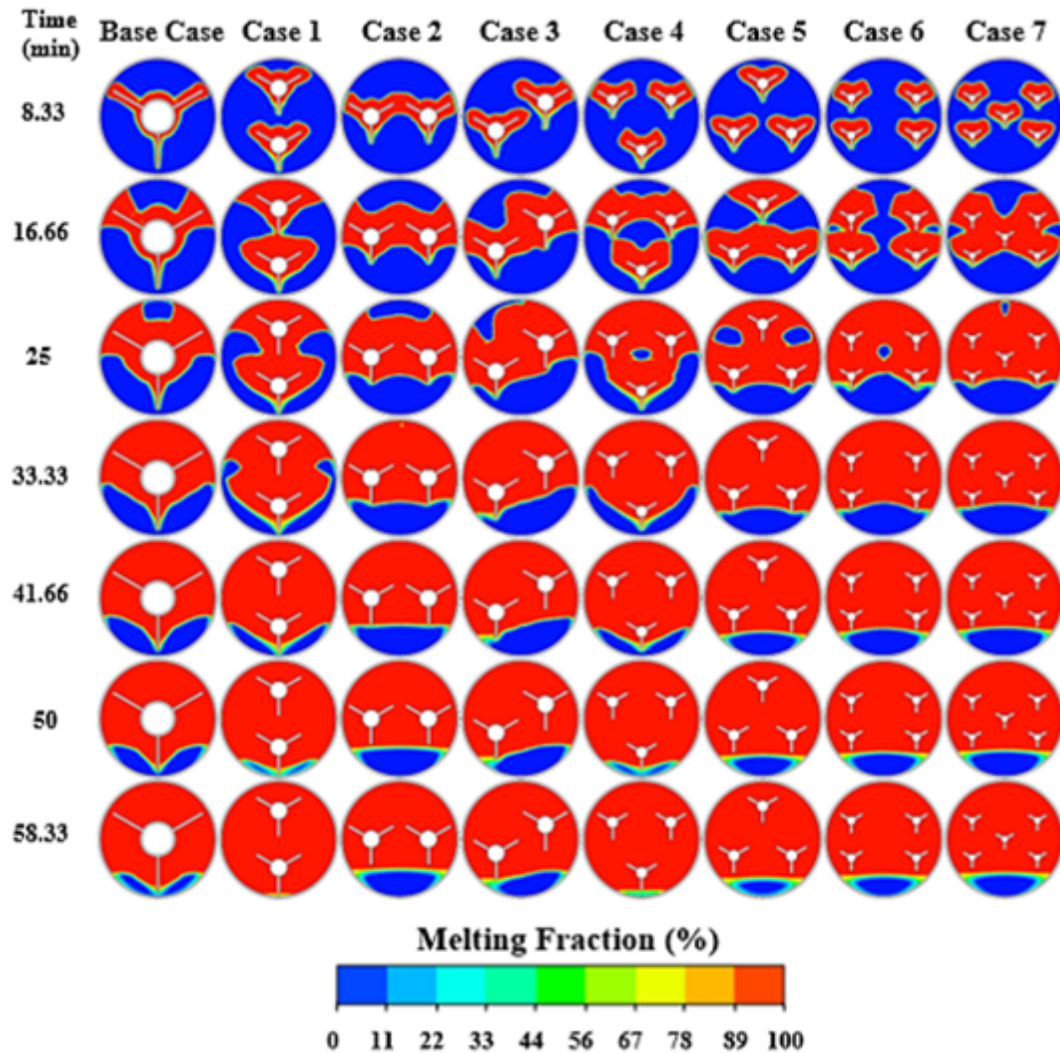
FIGURE 4.3: Melting Fraction Contours

average temperatures; more the number of tubes higher is the average temperature of the PCM. The reason being the fact that in case of more tubes the larger heat transfer surface is exposed to the cooler PCM and therefore more temperature gradients result in the more heat transfer, i.e., higher average temperatures. The average temperatures continue to rise following the same pattern until all the PCM above the HTF tubes gets heated and melted by the combined actions of conduction and convection. The temperatures of the PCM reach the temperature of the HTF locally, i.e., 358 K; this condition is achieved at t 40 min as represented by sudden change in the slopes of the temperature profiles. The heat is then transferred slowly through the conduction mode of heat transfer to the solid pool of PCM lying at the bottom of the shell. Eventually, after sufficient time the whole

PCM body gets melted and average temperatures reach the temperature of the HTF globally, i.e., 358 K. Cases 1 and 4 stand exception as these designs contain a HTF tube near the bottom of the shell and therefore continuously transfer heat to the solid pool of PCM lying at the lower portion of the shell. Therefore, the average temperature rise follows an almost constant slope until it reaches 358 K. The slope does not change significantly as it happens for the other multitube designs.
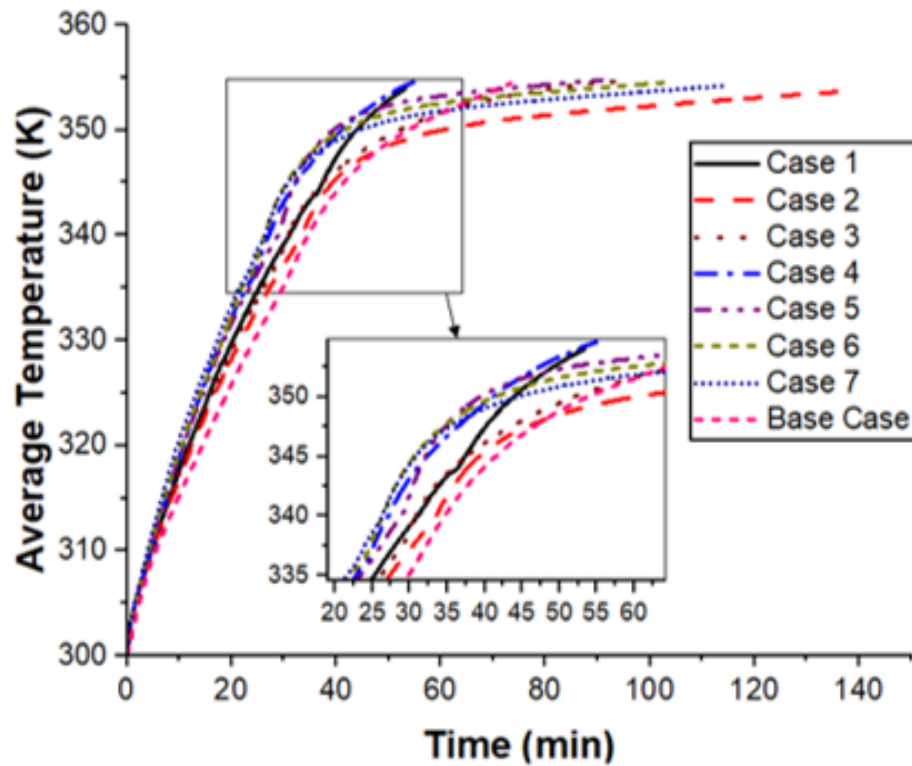


FIGURE 4.4: Comparison of Average Temperature

In order to reinforce the physical understanding of the phenomena, the contour plots of temperature for all the multitube cases along with the base case are presented in **Figure: 4.5**. The columns represent different cases whereas the rows show various time instances. Initially, the temperature of the PCM in contact with the heat transfer surfaces starts rising and continues to rise till melting temperature of PCM is reached. At this temperature all the heat supplied is consumed in changing the phase of the PCM converting the solid PCM in to the liquid. This

process continues till all the PCM above the HTF tubes gets melted. Further addition of heat results in the rise of the average PCM temperature until it reaches HTF temperature, i.e., 358 K. During this process, the heat is continuously conducted to solid pool of PCM settling in the lower section of the shell below the HTF tubes.
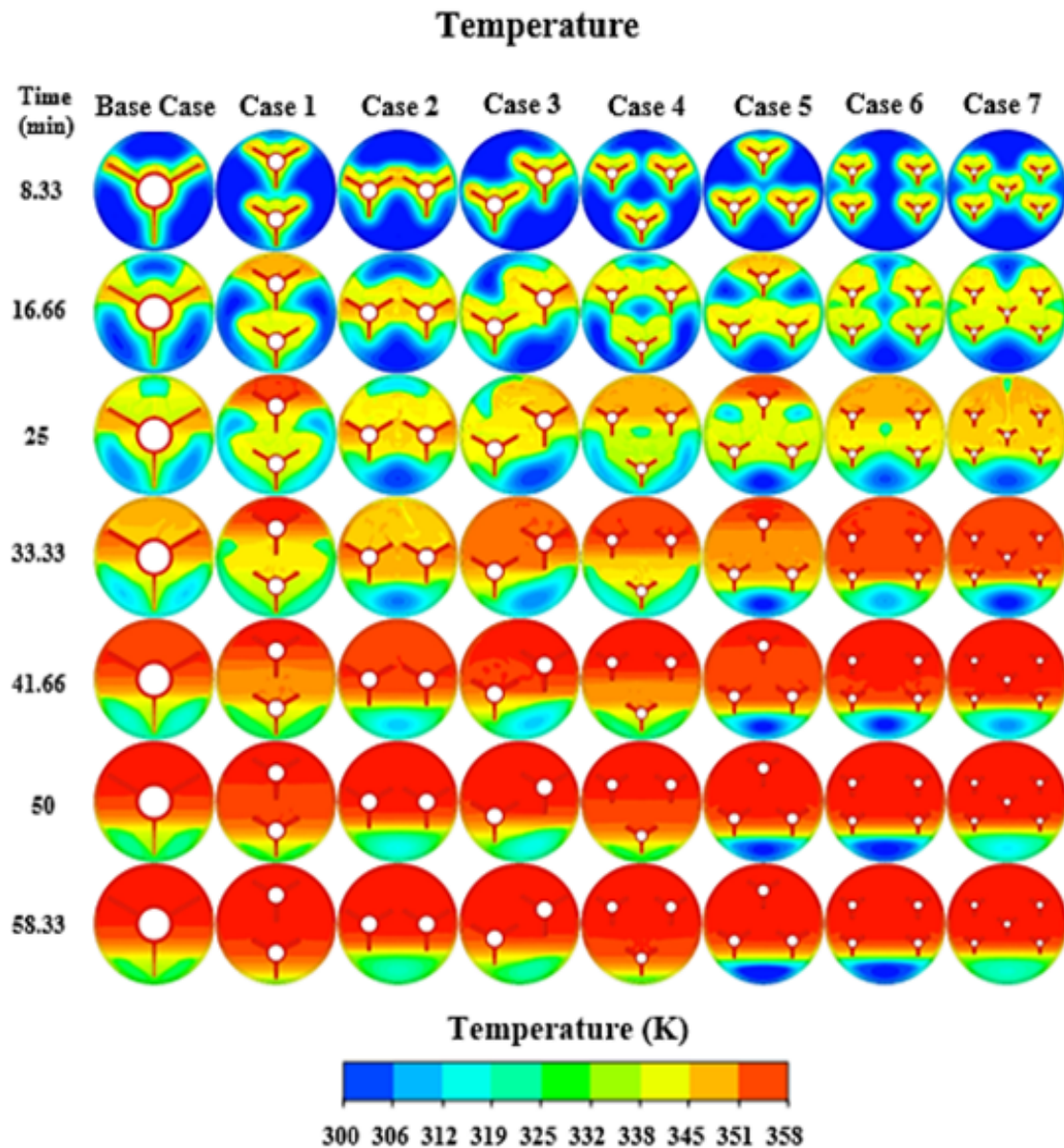


FIGURE 4.5: Temperature Contours

Case 1 and case 4 perform differently in the sense that there exists a HTF tube in the lower portion of the shell which assists in the rapid increase of the PCM temperature causing it to melt quickly as compared to the other multitube cases. Furthermore, it can be seen from the temperature contour plots at 58.33 minutes

that the whole PCM body approximately attains uniform average temperatures for cases 1 and 4. The rest of the multitube cases also attain the maximum temperatures of 358 K but not uniformly distributed rather concentrated in the upper portion of the shell containing the HTF tubes. Designs of Case 1 and case 4 prove to be superior as compared to the base case and other multitube designs as it result in faster melting and uniform average temperatures.

### 4.1.3   Melting Enhancement Ratio and Time Saving

Two performance parameters are defined to quantitatively assess the performance of the multitube designs as compared to the base case. Percentage enhancement ratio ($E_R$), as defined in **eq. (4.1)**, is the difference between the melting fraction of new design and that of the base case at the same instance of time t.

$$E_R = \frac{\bar{\alpha}_i(t) - \bar{\alpha}_1(t)}{1.0} \times 100\% \tag{4.1}$$

The percentage time saving ($t_{ms}$), as defined in **eq. (4.2)**, measures the time saved in percentage by a certain design for the complete melting of PCM as compared to the base case.

$$t_{ms} = \frac{t_{m,max} - t_m}{t_m, max} \times 100\% \tag{4.2}$$

where ($t_{m,max}$) and $t_m$ represent the time require1d for the complete melting of PCM by the proposed new design and the base case, respectively. The increase in $E_R$ indicates improvement of melting performance by using different multitube configurations in comparison to the base case. The temporal evolution of the percentage enhancement ratio for cases $1 - 7$ is plotted in **Figure: 4.6**. For all the cases at time t < 5 mins, $E_R$ remains identical because initially dominant heat transfer mode is conduction and the natural convection effects are negligible. However, for time t > 10 mins, convection heat transfer kicks in where role of multiple tubes is significant. Two peaks are noticed in the enhancement ratio

percentage at t 17 min corresponding to the case 6 and 7 showing a value of 26% and 30%, respectively. This is because their melting rate is high in the initial phase due to splitting of single HTF tube into four and five tubes which provide more distributed heat sources present among the shell for melting of PCM. However, a sudden decrease is observed at t=22 mins in these cases because of complete melting in upper portion of LTESS due to natural convection and buoyancy. Rest of the cases show intermediate performances reporting the values of $E_R$ as: 16% for case 4, 14% for case 2, 16% for case 4, 9% for case 3 and 7% for case 1. Case 1 and case 4 show improved performance till complete melting because of a HTF tube placed in the bottom region of the shell. Hence, case 1 and case 4 are selected for further analysis because of their enhanced performance characteristics compared to all other cases.

Percentage time saving for all the multitube designs are represented in **Table: 4.1**. Case 1 and case 4 show percentage time saving of 27.7% and 21.7% when compared to the base case. This leads to the conclusion that the multitube cases with two tubes arranged vertically and three tubes in V-arrangement increase melting rate and enhancement ratio that consequently reduce melting time of the PCM with respect to the base case.
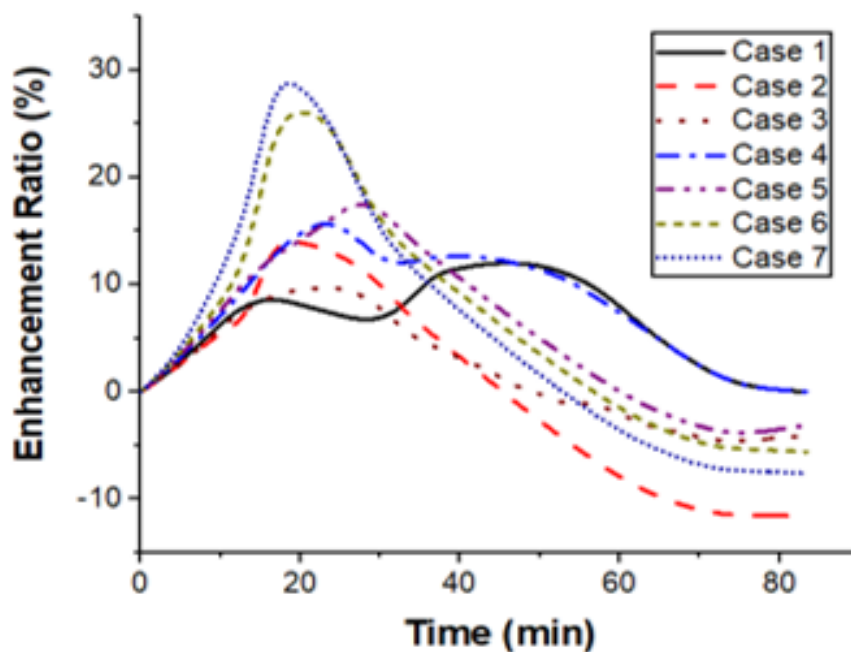


FIGURE 4.6: Enhancement Ratio During Melting Process

TABLE 4.1: Time Saving Percentages of All Cases with Respect to Base Case

| Case | Complete Melting Time (mins) | Time Saving (%) |
|------|------------------------------|-----------------|
| Base | 83 | - |
| 1 | 60 | 27.71084 |
| 2 | 160 | -92.7711 |
| 3 | 112 | -34.9398 |
| 4 | 65 | 21.68675 |
| 5 | 110 | -32.5301 |
| 6 | 124 | -49.3976 |
| 7 | 138 | -66.2651 |

## 4.1.4 Flow Patterns During Phase Transition Process of PCM

To understand the development and progression of the melting front in the PCM, detailed analysis of the velocity contours and streamlines is performed for cases 1 and 4 and compared with the Base Case as shown in **Figure: 4.7**. Cases 1 and 4 are selected because of their better performance indicators and to explore further improvement avenues.

At time t=8.33 mins, all the cases almost develop similar patterns of streamlines and velocities around the tubes and fins because of conduction dominant zone. Small vortex pairs begin to form on the upper surface of fins, whereas, HTF tube generates relatively large vortex pairs. Later, at t=16.66 mins, the melted PCM around fins and HTF tube starts rising due to convective currents generated due to buoyancy effects which expands these vortices towards the upper region of shell and accelerates the flow. This phenomenon continues till t=33.33 mins when all the PCM gets melted and velocities start to slow down. It can be seen that for the Base Case, at t=41.66 mins, large vortices are trapped in between the upper two fins of the Y-fin design and cannot transfer the momentum of these vortices to the lower portion where the PCM is still in the solid phase. This results in the damping out of the vortices resulting in some decreased velocities. In contrast, for the cases 1 and 4, the splitting and the intelligent placement of the tubes creates favorable conditions for the transfer of the momentum generated by vortices to melt the PCM lying at the bottom of the shell. Sufficiently large velocities still

exist near the solid PCM for cases 1 and 4 as shown in the time frames t=50 –
58.33 mins. At t=58.33 mins, Case 1 and Case 4 achieve almost complete melting
due to enhanced heat transfer and velocity recirculation which are formed around
the tubes and fins.
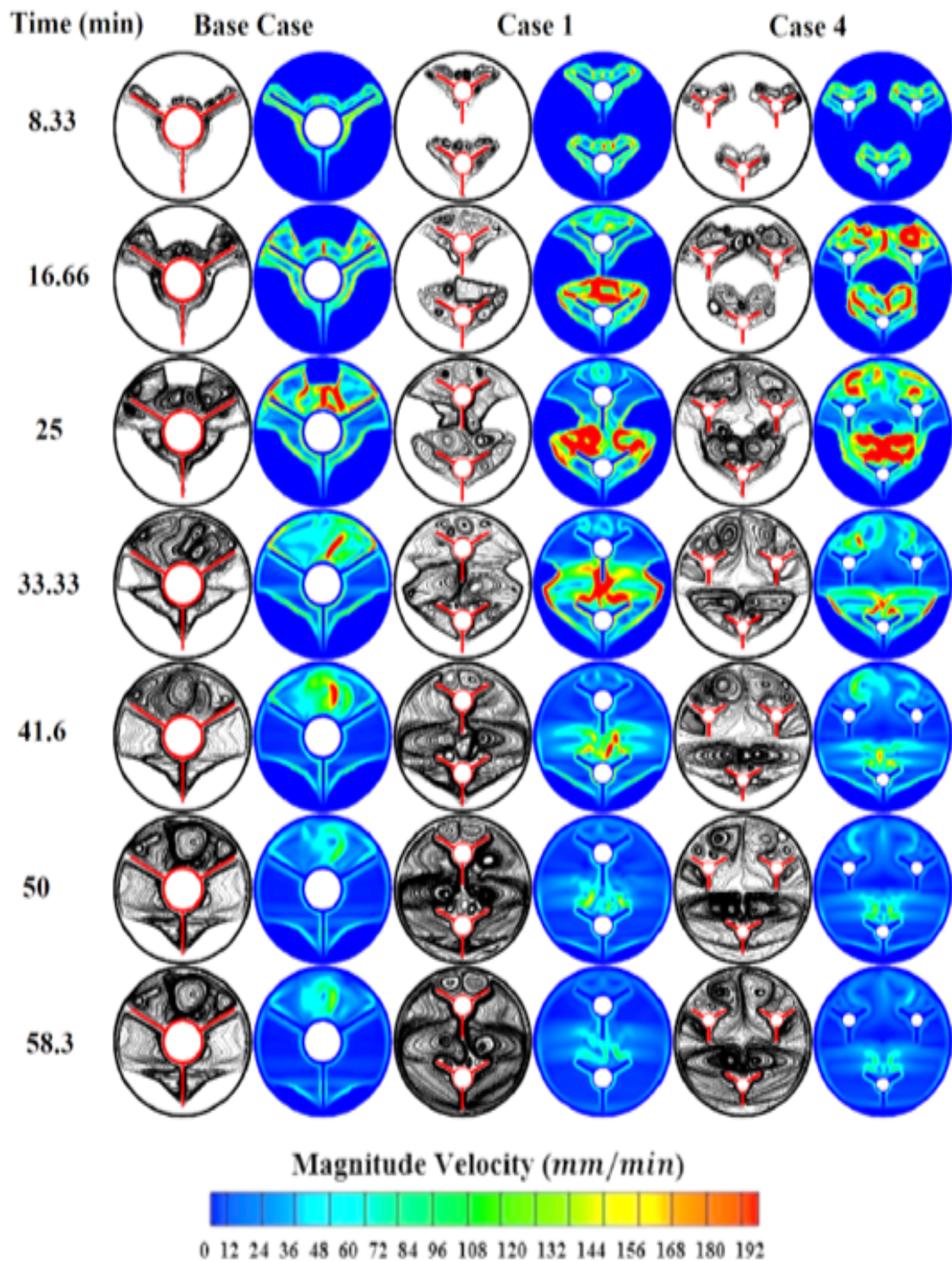


FIGURE 4.7: Streamlines and Velocities Contours

## 4.1.5   Comparison of Energy Storage

An important aspect of LTESS design is thermal energy storage rate. Energy storage is a combination of sensible and latent thermal energies. Prior to melting, sensible thermal energy is stored in solid PCM by elevating its temperature, whereas, latent energy is stored during the phase transition process of PCM (solid to liquid). After complete melting of the PCM, heat is again stored as sensible energy, as liquid PCM temperature rises again. . Energy storage rate is defined as:

$$\frac{\Delta E}{\Delta t} = \frac{M_{pcm}(h_{i+1} - h_i)}{t_{i+1-t_i}} \tag{4.3}$$

Where $M_{pcm}$ is the mass of PCM stored in 1m length of LTESS, $h_{(i+1)}$, $h_i$ are specific enthalpies at time instances of $t_{(i+1)}$, $t_i$, respectively. The rate of thermal energy storage of LTESS having 1 m length is demonstrated in **Figure: 4.8 (a)**. It can be observed that, initially, the rate of energy storage is high due to large temperature difference between the HTF and the solid PCM. The rate of energy storage decreases sharply as the PCM melts around the heated surfaces and decreases the temperature gradient. This is because, for a short initial time, dominant mode of heat transfer is conduction. Afterwards, the buoyancy effects kick in and initiate flow of thermal boundary layer due to density difference creating convective currents. Heat transfer rate between the solid PCM and liquid PCM around the HTF tube increases due to effects of natural convection. Therefore, the liquid PCM dissipates heat which results in an increase of temperature difference between the PCM and heated surfaces. For cases having more tubes, energy storage rate is higher during initial 20 mins due to provision of more split heat sources. But after 25 mins an abrupt decrease in energy storage rate for all the cases is observed. Later, during the interval 25<t<50 mins, Case 1 performs better than all other cases and supplies constant rate of energy to melt the PCM, after 50 mins the Base Case overtakes Case 1 because the larger lower fin of the Y-design continues to supply heat to the cool solid PCM settling at the bottom

of the shell. At t=60 mins, Case 1 and Case 4 have melted all the available PCM and the average temperature reaches the HTF temperature, i.e., 358 K, due to which the energy storage rate quickly decreases. Rest of the cases still have some solid PCM lying at the bottom of shell and therefore transfer energy slowly at a constant rate. Average thermal energy storage rates of case 1, case 4 and Base Case are 974 W, 902 W and 729 W. Therefore, Case 1 and Case 4 have improved the energy storage rates by 33.6% and 23.7%. However, loss of energy in terms of pressure drop across case 1 and case 4 are 0.585 and 2.303 Watts, which shows that gain of energy is lot higher than the losses occurring due to pressure drop, hence these losses can be neglected.

Time history of the energy storage (kJ) for all the cases are plotted in **Figure 4.8 (b)**. Initially, all the cases show similar behavior of energy storage over time because of conduction dominant phenomenon. After t=2.5 mins, the results start to deviate due to the multitube arrangements and the buoyancy driven convection effects. More are the number of tubes, stronger are the convective currents. During the interval 2.5<t<40 mins, all the cases show almost linear trend of energy storage. Once all the PCM above the HTF tubes gets melted, the energy storage with time slows down as represented by decrease in the slope of the energy storage curve. However, Case 1 and Case 4 show constant behavior because both these designs have HTF tube lying near the bottom of the shell which continuously supply energy to the PCM lying at the bottom.

## 4.1.6   Important Design Parameters of LTESU

Case 1 with two vertical tubes and Y-configuration of fins is considered as the optimum split tubes arrangement which declares highest enhancement ratio, shortest PCM melting time and highest rate of energy storage during melting process. However, other design parameters are also important to be considered in order to investigate their effect on melting performance of LTESS. These important parameters include thermo-physical properties of fins and temperature which directly affect the energy storage and melting time of the system.
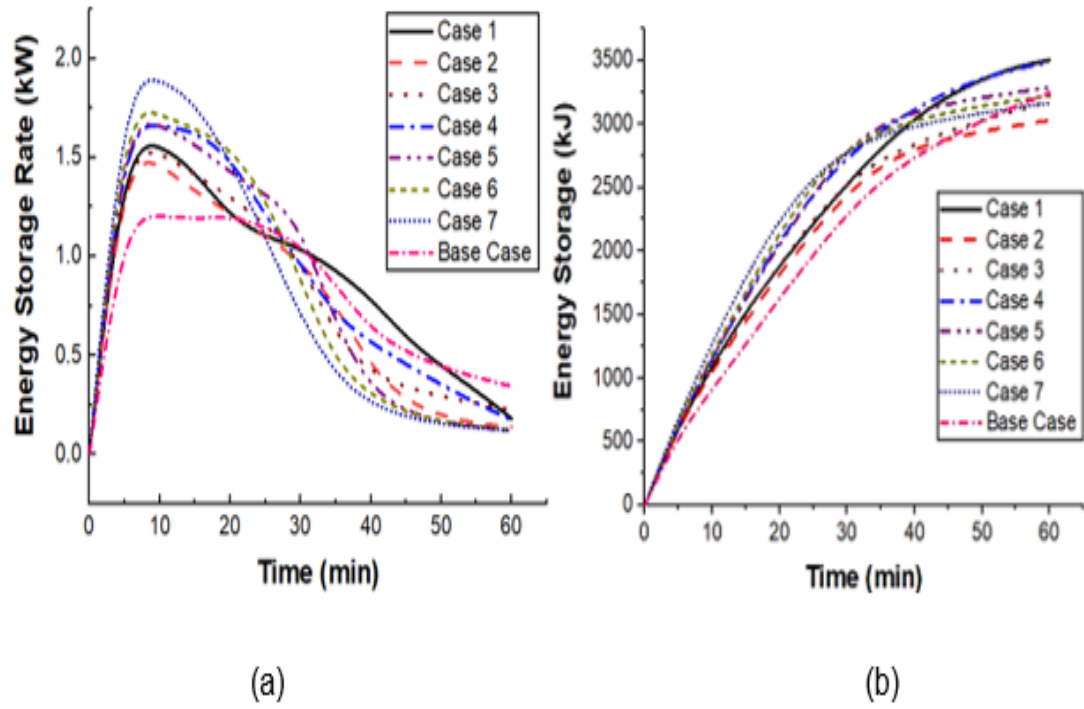
FIGURE 4.8: Rate of Thermal Energy Storage (b) Thermal Energy Storage

## 4.2 Effect of Thermo-Physical Properties of Fins

Time-based evolution of melting fraction of PCM is depicted in **Figure: 4.9**, to investigate the effects of thermo-physical properties of fins on melting performance of LTESS. Thermo-physical properties including thermal effusivity and diffusivity for different materials of Brass, Steel, Copper and Aluminium are shown in **Table: 5**. For penetration of thermal energy in the material, thermal diffusivity $a_{th} = k/\rho C_p$) is responsible whereas, the ability of a material to exchange thermal energy between the surrounding and surface is related by thermal effusivity $e_{th} = \sqrt{k\rho C_p}$. The results obtained in the **Figure: 4.9** show that the fins of copper have the highest melting rate with respect to other fin materials used. This is because of higher thermal diffusivity of copper fins due to which thermal energy penetrates faster from HTF tube through fins. Better heat transfer from HTF tube and fins to PCM is attained due to high thermal effusivity of copper which consequently reduces melting time of LTESS. Therefore, it is proposed to use fin material of copper which has higher thermal effusivity and diffusivity. It is determined from

the analysis of melting rates of PCM, that fin materials having high effusivity and diffusivity should be used. For the current study, analysis is performed with the copper fins attached to two split tubes arranged vertically among LTESS that are selected as best case to select optimum fins material.
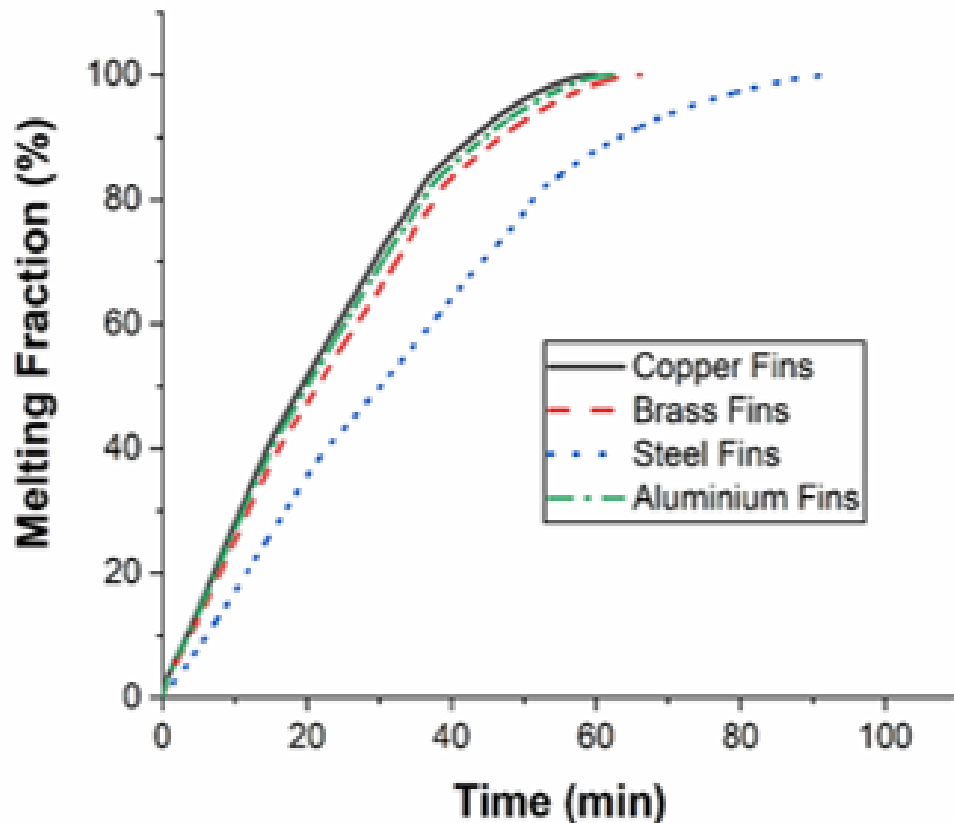


FIGURE 4.9: Melting Fraction of Different Fin Materials

## 4.3 Effect of Temperature of Htf on Heat Transfer Characteristics and Melting of PCM

To investigate the effects of the HTF temperatures on the heat transfer and melting behaviors of PCM in LTESS, non-dimensional Stefan (Ste), Nusselt (Nu), Rayleigh (Ra) and Fourier ($F_o$) numbers are plotted in **Figure: 4.10** and **Figure: 4.11**. Split tube case 1, is studied in comparison with the base case with

varying HTF temperatures, $T_{HTF}$.

The HTF temperature is varied in the range 338 K $\leq T_{HTF} \leq$ 378K which corresponds to the Stefan number and Rayleigh numbers to vary in the range (0.0063 $\leq$ Ste $\leq$ 0.51) and (0.466×10$^6$ $\leq$ Ra $\leq$ 1.9×10$^7$), respectively. The variations of Ste and Ra for different HTF tube temperatures (338K$\leq T_{HTF} \leq$ 378K) are listed in **Table: 4.2**. A wide range of Stefan (0.0063$\leq$ Ste $\leq$ 0.51) numbers and Rayleigh numbers(0.466×10$^6$ $\leq$Ra $\leq$ 1.9×10$^7$) are covered by varying HTF tube temperatures for Case 1 (two tubes placed vertically with Y-fins).

It can be seen in **Figure: 4.10** that during melting process, for small Stefan number, Fourier number is quite large due to very small gradients of temperature between PCM and the HTF and conduction dominance.

As the HTF temperature increases, consequently the Stefan number also increases with the increase in temperature gradient between the HTF and the PCM, which results in a sharp decrease in the Fourier number. This decreasing trend slows down for Ste>0.133.

This decrease is related to the boundary layer thickness of the melted PCM around tube and fins. Higher Stefan number leads to a thicker boundry layer which acts as a barrier to the conduction heat transfer. However, the convection heat transfer starts playing dominant role as the liquid PCM layer enveloping the heated surfaces start to rise and enhance melting.

For variation of Stefan number with Fourier number during melting process, correlations are in **eq. (4.4)** for Case 1 and Base Case at different temperature ranges as given below:

$$Fo = c_1(Ste)^{-c_2} \qquad 338 \leq T_{HTF} \leq 378 \qquad (4.4)$$

where $c_1$= 0.118 and $c_2$=0.556 for Case 1s and 4s, while for Base Case $c_1$=0.225 and $c_2$=0.453.

In order to investigate the convective heat transfer effects in relation to the conduction process, average Nusselt number ($\overline{Nu}$) is plotted against the Rayleigh

Number as depicted in **Figure: 4.11**. Rayleigh number is the ratio of the buoyancy to the viscous forces, whereas, the average Nusselt number $(\overline{Nu})$ is defined as follows

$$\overline{Nu} = \frac{\overline{h_c} D_t}{K_{PCM}} = \frac{\overline{Q_E}}{\pi k_{PCM} |T_{HTF} - T_{PCM}|} \tag{4.5}$$

where $\overline{Q_E}$ calculated by dividing the total energy stored by the PCM by the complete melting time, and $\overline{h_c}$ denotes average heat transfer coefficient. For case 1, $(\overline{Nu})$ against different Ra for melting process has also been given in **Table: 4.2**. For melting processes, variation of average Nusselt numbers at different Rayleigh numbers have been plotted in **Figure: 4.11**. As the temperature of the HTF increases, Rayleigh number also increases which results in an increase of buoyancy forces. The buoyancy forces cause the rise of liquid PCM thereby increasing heat transfer due to convection and ultimately the average Nusselt number $(\overline{Nu})$ as represented in **Figure: 4.11**. Initially, $(\overline{Nu})$ increases sharply but it becomes almost linear after Ra> $9.78 \times 10^6$ For melting process, correlations for Nusselt number in relationship with Rayleigh number are shown in **eq. (4.6)** for Case 1 Base Case.

$$\overline{Nu_m} = c_1 (Ra)_2^c, 338k \leq T_{HTF} \leq 378K \tag{4.6}$$

where $c_1$= 0.0111 and $c_2$=0.4608 for Case 1 while for Base Case $c_1$=0.0147 and $c_2$=0.4232.

On analysis of all the melting process of PCM by splitting single concentric tube(Base Case) into multi tubes (Case 1 to 7) and their different relative arrangements show that Case 1 and Case 4 can be selected as the optimum cases which demonstrate considerable reduction in melting time, enhanced melting rate performance, temperature distribution among shell and better energy storage rates over other cases. To further improve their performance in melting process, these optimum cases i.e.
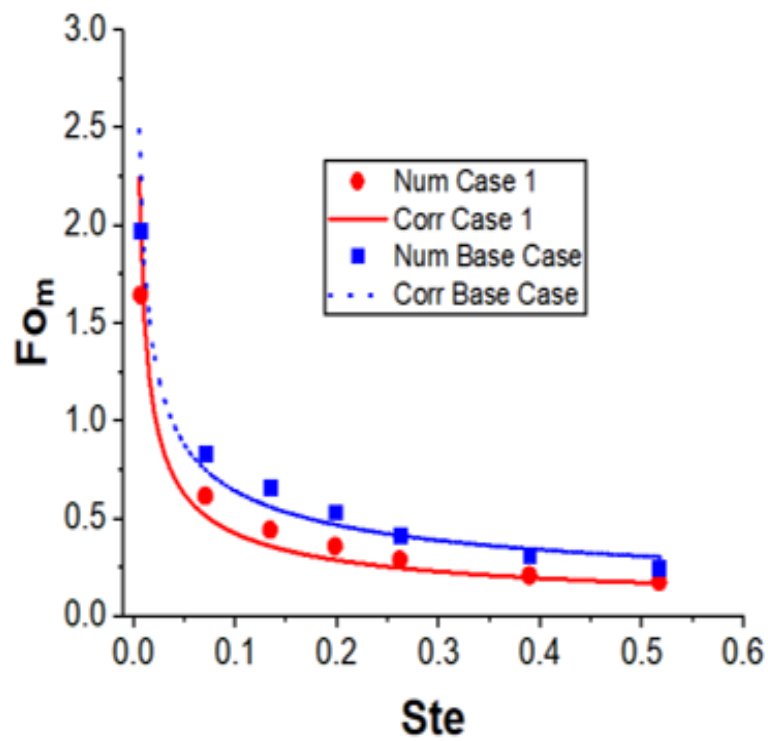
FIGURE 4.10: Stefan Number in Relation with Fourier Number for Melting Process
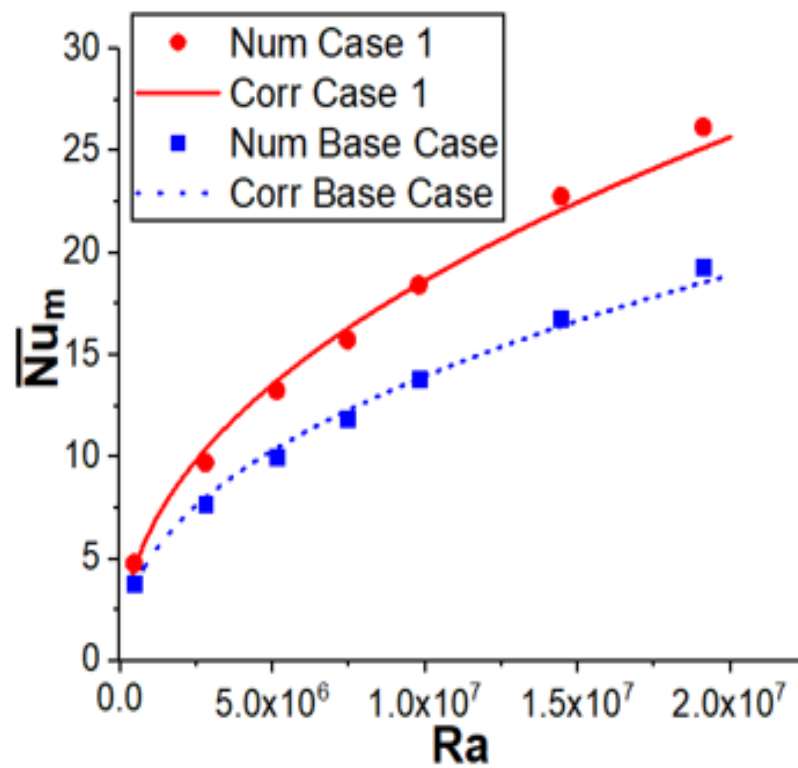


FIGURE 4.11: Relation of Nusselt Number with Rayleigh Number During Melting Process

TABLE 4.2: Non-Dimensional Parameters for Different HTF Temperatures for Case 1

| $\mathbf{T}_{HTF}$(K) | *Ste* | Fo | Ra | Avg.Nusselt Number |
|---|---|---|---|---|
| | | Melt. | Melt. | Melt. |
| 338 | 0.00638 | 1.54555 | $0.466 \times 10^6$ | 4.77 |
| 343 | 0.07019 | 0.69691 | $2.796 \times 10^6$ | 9.72 |
| 348 | 0.13399 | 0.47403 | $5.12 \times 10^6$ | 13.23 |
| 353 | 0.19780 | 0.39114 | $7.45 \times 10^6$ | 15.34 |
| 358 | 0.261608 | 0.30137 | $9.78 \times 10^6$ | 18.4 |
| 368 | 0.38922 | 0.22075 | $14.4 \times 10^6$ | 22.76 |
| 378 | 0.51683 | 0.1768 | $19.11 \times 10^6$ | 26.17 |

Case 1 and Case 4 are now explored by varying their shell geometries to study the effect of changing shell shape on performance parameters with respect to the Base Case (single concentric tube with Y-arrangement fins).

## 4.4 Effect of Shell Design Modifications

The cylindrical shell designs are modified for cases 1 and 4 to further improve the melting and heat storage performances. The modifications of shells are carried out while observing the melting processes of Case 1 and 4. The shells are designed to not only avoid un-melted pool of PCM at the bottom of LTESS. As a reference, the configurations of HTF tubes and the distance of bottom fin and shell are kept constant as in original multi-tube cases with circular shells. The provision of large convection heat transfer area accelerates the melting process. The effective shell volume is also kept constant in order to keep amount of PCM constant in all cases. An elliptic shell design is proposed for Case 1 having two tubes arranged vertically and the design is named as Case 1s as shown in **Figure: 4.12 (a & b)**. The elliptic shell has major and minor diameters of $D_{maj}$=155.046 mm and $D_{min}$=94.43 mm and shell has thickness of $S_t$=3 mm. Two heat transfer tubes are placed vertically keeping the position of tubes and fins same as it was in case 1 and fixing bottom fin edge of lower tube at distance of 2.75 mm from the lower

edge of ellipse. The selection of the major and minor diameters for elliptic shell is based on the criteria to enhance natural convection currents assisted by buoyancy effects.

A triangular shell with fillet edges is proposed for Case 4 having three tubes arrangement in V shape and the design is named as Case 4s as shown in **Figure: 4.12 (c & d)**. The triangular shell has three sides of the same length i.e $L_s$=129.768 mm, with an included angle $\theta$=60° between two adjacent sides forming an equilateral triangle with rounded corners. The chord length of rounded corners ($S_1$) and length of sharp corner edge ($S_2$) are 17.321mm with a fillet radius (r) of 10mm. The corners of triangular shell are rounded in order to avoid un-melted zones of PCM. Three heat transfer tubes are placed in V-configuration keeping the position of tubes and fins same as it was in Case 4 and the bottom fin edge of lower tube is fixed at distance of 6.5 mm from the bottom of the triangular shell. PCM is filled in the space between the shell and tubes. The thickness of fins is kept constant, i.e., $t_t$=3mm.



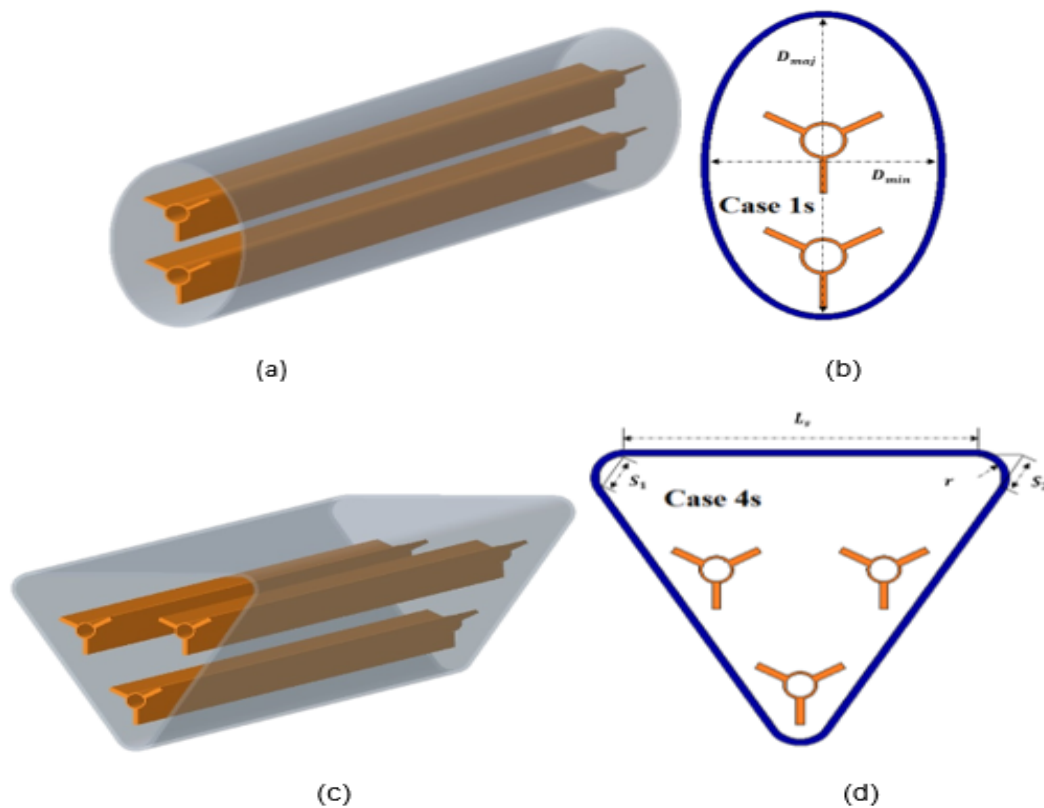FIGURE 4.12: Computational Domain of LTESS of Elliptic (a) 3D (b) 2D; and Triangular (c) 3D (d) 2D

## 4.4.1 Effect of Shell Modification on Melting Process and Temperature Distribution

To explore and analyze the performance of the modified shell cases, the line plots of melting fraction and temperature for the relevant cases are presented in **Figure: 4.13**. It can be seen that the melting fraction plots of the modified shell cases start to deviate from the corresponding cylindrical shell results after t=20 mins. This can be explained using the contour plots of melting fraction as shown in **Figure: 4.14 (a)**. At t=18 mins, both the cylindrical and the modified shell designs have the same amount of solid PCM but the modified shells are so designed that more PCM is now placed above the HTF tubes. Therefore, the convective currents generated due to buoyancy effects melt the solid PCM lying above the HTF tubes at a faster pace as compared to the cylindrical shell which melts the solid PCM lying below the HTF tubes by conduction. As a result, all the PCM gets melted for the modified designs at t=42 mins, whereas, cylindrical shell designs still contain solid PCM.

The average temperatures are not much affected by the shell design modification as shown in **Figure: 4.13 (b)**. However, it is observed from the contour plots of temperature, **Figure: 4.14 (b)**, that the temperature distribution is uniform in the modified shell designs as compared to the cylindrical shell designs. This is because of the intelligent shell designs; more PCM is filled above the HTF tubes and gets melted due to the convection heat transfer. The convective currents efficiently mix the PCM thereby generating uniform temperatures. In contrast, for the cylindrical shells, the PCM above the HTF tubes gets melted and the melted PCM further heats up, whereas, the solid PCM lying below the HTF tube slowly receives heat by conduction and takes long time to melt.

Complete melting time of the PCM for the cylindrical and modified shell designs are compared with the Base Case as shown in **Figure: 4.15**. Case 1s and Case 4s completely melt their PCM in 42 mins and 41 mins, respectively. This is a significant time reduction as compared to the Base Case which takes 83 minutes to completely melt the PCM. This is achieved due to better shell designs where

most of the PCM is above the HTF tubes and the convective currents assist in the faster melting of the PCM.
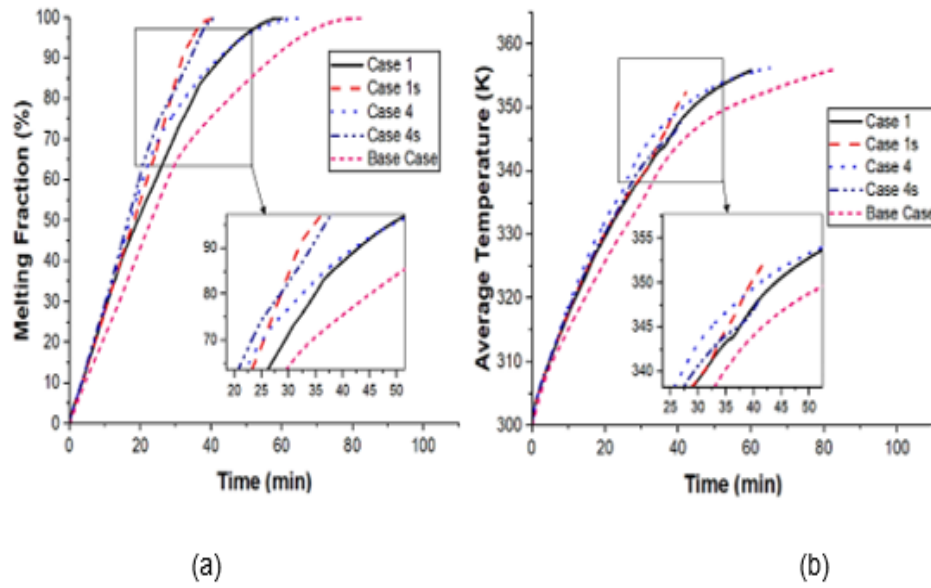


FIGURE 4.13: Different Shell Configurations Comparison of LTESS (a) Melting Fraction (b) Temperature (c) Complete Melting Time
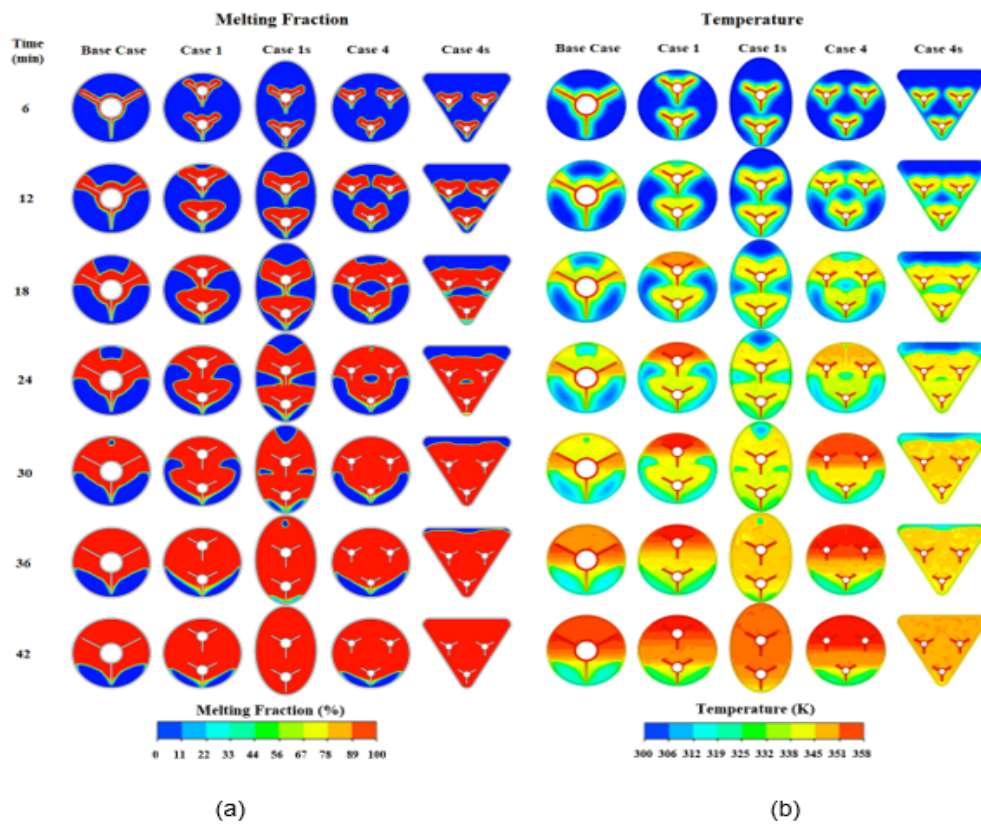


FIGURE 4.14: Melting Fraction and Temperature Contours
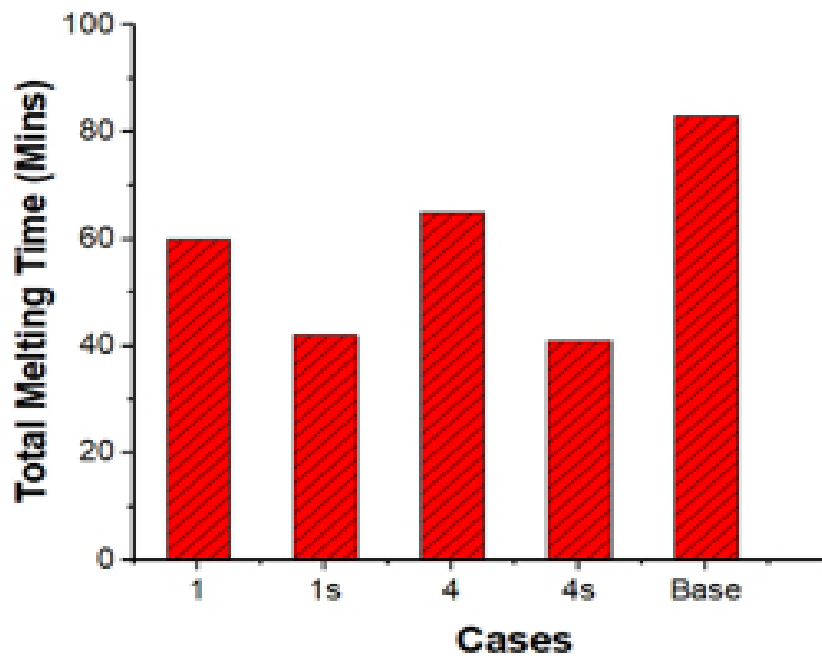
FIGURE 4.15: Comparison of Complete Melting Time for Different Shell Configurations of LTESS

## 4.4.2 Flow Patterns During Phase Transition Process of PCM

The effect of shell design on flow characteristics of melted PCM are elaborated by analyzing temporal evolution of velocity contours and streamlines of Base Case, Case 1s and Case 4s as presented in **Figure: 4.16**. At time t=8.33 mins, all the cases almost develop similar patterns of streamlines and velocities around the tubes and fins because of conduction dominant zone. Small vortex pairs begin to form on the upper surface of fins, whereas, HTF tube generates relatively large vortex pairs. Later, at t=16.66 mins, the melted PCM around fins and HTF tube starts rising due to natural convective currents generated due to buoyancy effects. The buoyant forces initiate upward movement of these vortices and causes acceleration in PCM melting. This phenomenon continues till t=33.33 mins when most of the PCM melts and velocities of melting front slow down. It can be seen that for the Base Case, at t=33.33 mins, large vortices are trapped in between the upper two fins of the Y-fin design and cannot transfer the heat to the un-melted

portion of PCM. Therefore, weak convention effects decelerate the melting process and thermal performance of heat storage reduces. In contrast, for the cases 1s and 4s, the intelligent placement of split tubes and shell shapes modifications create favorable conditions for the transfer of the momentum generated by vortices to melt the PCM even at the bottom of the shell. Large vortex pairs with high velocities can be seen travelling upwards for Case 1s and 4s due to intensified effects of natural convection as shown for 3.33 mins≤t≤41.66 mins. At t=42 mins and 41 mins, Case 1s and Case 4s, respectively, achieve almost complete melting due to enhanced heat transfer and velocity recirculation which are formed around the tubes and fins assisted by the shell geometries.



FIGURE 4.16: Streamlines and Velocities Contours

### 4.4.3 Comparison of Energy Storage

The effects of the modified shell designs on the energy storage rate are analyzed by comparing the results of cylindrical and modified shells based LTESS of 1 m length. The results are presented in **Figure: 4.17**. The Base Case results are also plotted for reference. The energy storage rates for the Case 1 and Case 1s start to deviate from each other after 10 mins with the modified shell having higher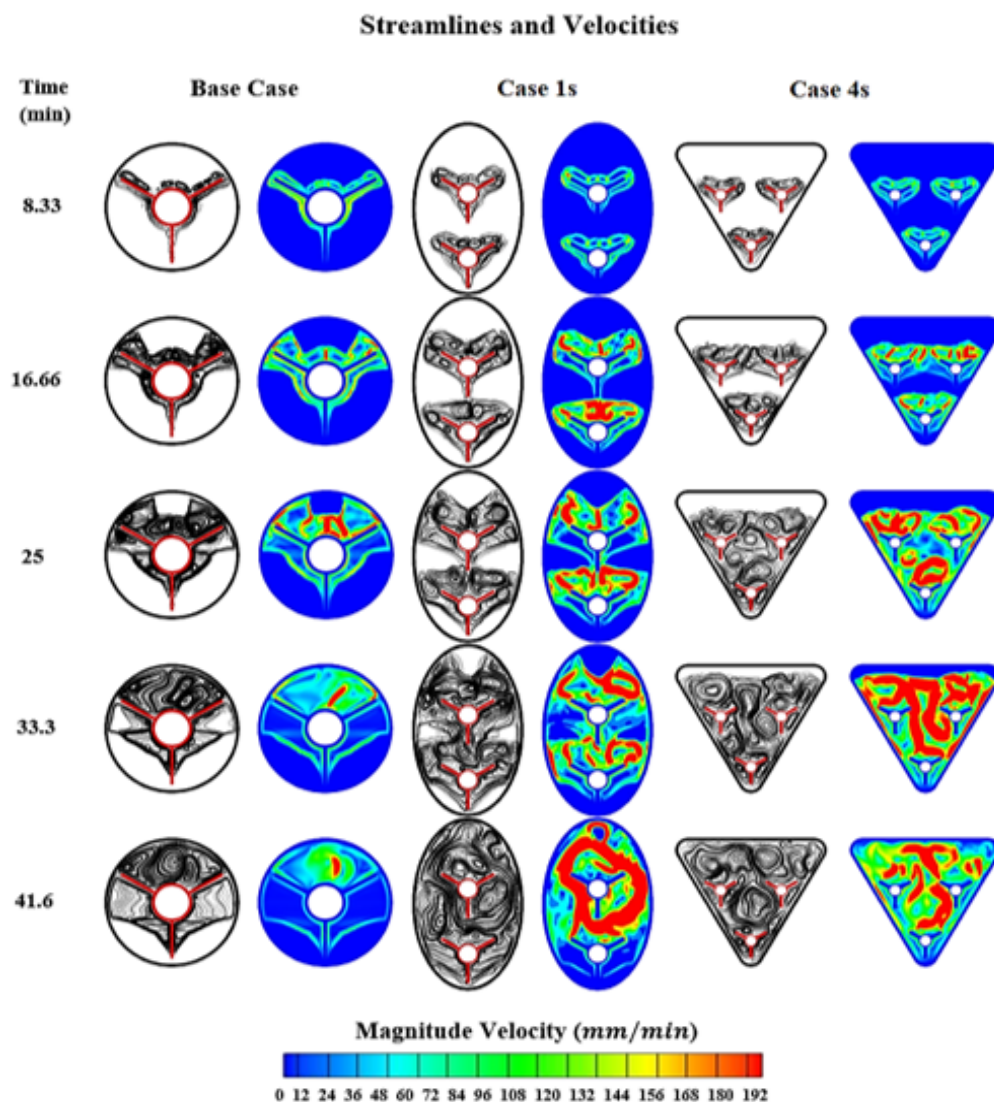 energy storage rate as compared to the cylindrical shell. However, for the Case 4 and Case 4s energy storage rates are same for both the cases till 18 mins. This is due to the placement of HTF tubes relative to the adiabatic shell and consequently the temperatures attained throughout the shell. A detailed analysis can be made using the contour plots of melting fraction and temperature as shown in **Figure: 4.14 (a & b)**. Comparing the HTF tubes for Case 1 and Case 1s, it can be seen that Case 1 has both the lower and upper tubes lying close to the adiabatic shell. The rising plume of the liquid PCM comes in contact with the shell and therefore gets trapped there. The temperature of the PCM in liquid state starts to rise locally resulting in a decrease of the temperature gradient. Consequently, the heat transfer and the energy storage rate also decrease. After that, the heat is propagated downwards through conduction mode as shown during time interval 18 – 42 mins in **Figure: 4.14 (b)**. In contrast, Case 1s has the upper tube located sufficiently below the shell top surface, therefore, the melted liquid PCM continues to rise creating strong convective currents. The temperature of the PCM increases uniformly and the temperature gradient decreases slowly. This results in an almost constant rate of heat transfer and energy storage rate. This trend continues till 30 mins when only a small amount of solid PCM is left away from the heated surfaces. Temperatures again start to rise locally reducing the gradients and therefore the heat transfer rates. Conduction again dominates the heat transfer process to heat up the solid PCM away from the heated surfaces and finally melts it. The reasoning explained above also justifies the trends of Case 4 and Case 4s. Specifically, after 30 mins, Case 4s significantly performs better than Case 4. This can be explained using the temperature contour plots shown in **Figure: 4.14 (b)**. The upper two tubes for Case 4 are surrounded by high temperature melted PCM which reduces

the heat transfer rate because of low temperature gradient. In contrast, all three tubes of Case 4s are surrounded by comparatively low temperature melted PCM. Therefore, rate of energy transfer is more due to large gradient of temperature. Average rates of energy storage of cases 1s, 4s and the Base Case are 1354 W, 1347 W and 729 W revealing the modified designs far better on energy storage index as compared to the Base Case.

The variation of energy storage with time for the cylindrical and modified shell cases is presented in **Figure: 4.17 (b)** as compared with the Base Case. These results are explained in connection with the energy storage rate results shown in **Figure: 4.17 (a)**. The energy storage rate of the Base Case is lowest over time; therefore, it stores the lesser amount of energy in a given time as compared to all other cases. Similarly, cases 1s and 4s having modified shells have higher energy storage rates than their cylindrical counterparts, therefore, these cases store more energy over time as compared to cases 1 and 4.

The comprehensive analysis of the modified shell cases, i.e., cases 1s and 4s, reveal that these are the best possible choices among all the multitube designs. These perform better in all the performance indicators resulting in faster melting, uniform temperature attainment and higher energy storage rates.
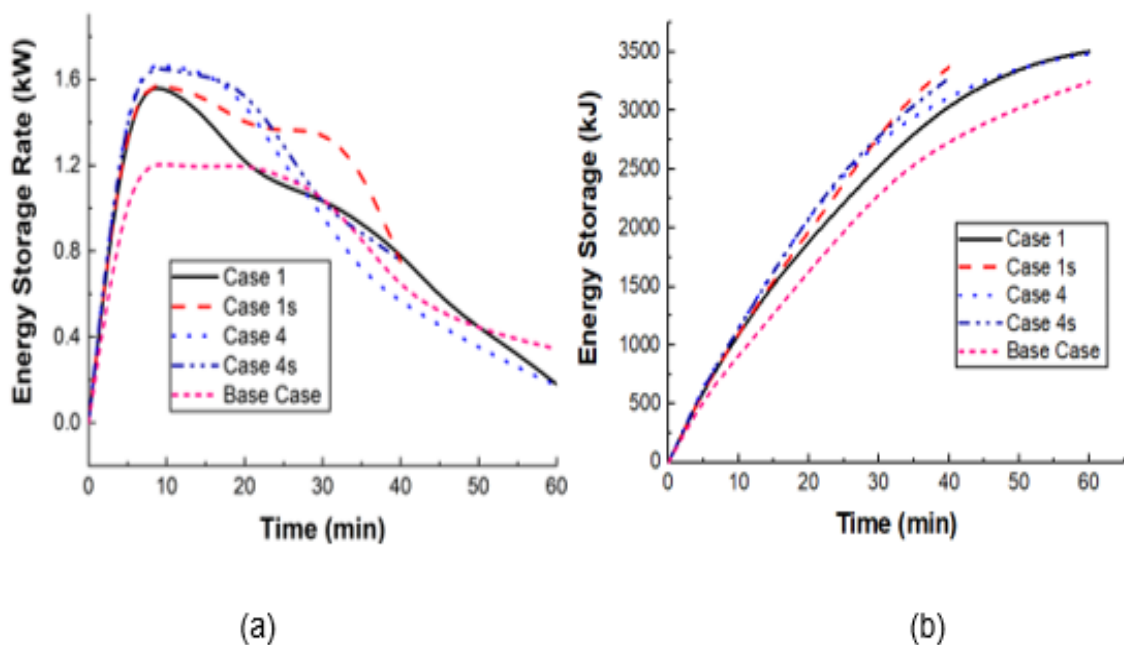


(a)          (b)

FIGURE 4.17: (a) Rate of Thermal Energy Storage (b) Thermal Energy Storage

# 4.5 Effect of HTF Temperature on Heat Transfer Characteristics and Melting of PCM

For shell modified case i.e case 4s, further investigation is performed to study the effects of the HTF temperatures on the heat transfer and melting behaviors of PCM, similarly as it is done for case 1, non-dimensional Stefan (Ste), Nusselt (Nu), Rayleigh (Ra) and Fourier ($F_o$) numbers are plotted in **Figure: 4.18** and **Figure: 4.19**. Split tube case 4s with triangular shell modification, is selected for comparison with the base case by varying HTF temperatures, $T_{HTF}$. The HTF temperature is varied in the range 338K≤ $T_{HTF}$ ≤378K which corresponds to the Stefan number and Rayleigh numbers to vary in the range (0.0063≤ Ste ≤0.51) and (0.466×$10^6$ ≤ Ra≤1.9×$10^7$ ), respectively. The variations of Ste and Ra for different HTF tube temperatures (338K≤$T_H TF$ ≤378K) are listed in **Table: 4.3**. A wide range of Stefan (0.0063≤Ste≤0.51) numbers and Rayleigh numbers (0.466 ×$10^6$ ≤Ra≤1.19×$10^7$ ) are covered by varying HTF tube temperatures for Case 1s and 4s. It can be seen in **Figure: 4.18**, that during melting process, for small Stefan number, Fourier number is quite large due to very small gradients of temperature between the PCM and HTF and conduction dominance. As the temperature of HTF increases, consequently the Stefan number also increases with the increase in temperature gradient between the HTF and the PCM, which results in a sharp decrease in the Fourier number. This decreasing trend slows down for Ste>0.133. This decrease is related to the boundary layer thickness of the melted PCM around tube and fins. Higher Stefan number leads to a thicker boundry layer which acts as a barrier to the conduction heat transfer. However, the convection heat transfer starts playing dominant role as the liquid PCM layer enveloping the heated surfaces starts to rise and enhances melting.The correlation for non-dimensional complete melting time of PCM (Fo) as a function of HTF temperature based Stefan numbers is presented in **eq. (4.7)** for Case 1s, 4s at different temperature ranges. Whereas, for Base Case correlation is already shown

in **eq. (4.4)**.

$$Fo = c_1(Ste)^{-c_2} \qquad 338 \leq T_{HTF} \leq 378 \qquad (4.7)$$

Where $c_1$=0.105 and $c_2$=0.5 for Case 1s and 4s.

In order to investigate the convective heat transfer effects in relation to the conduction process, average Nusselt number $(\overline{Nu})$ is plotted against the Rayleigh Number for melting process, as shown in **Figure: 4.19**. $(\overline{Nu})$ against different Ra for both melting process is also given in **Table 7**. $(\overline{Nu})$ as plotted in **Figure: 4.19**. Initially, $(\overline{Nu})$ increases sharply but it becomes almost linear after Ra> $9.78 \times 10^6$. For melting process of case 1s and 4s, correlation for Nusselt number in relationship with Rayleigh number is shown in **eq. (4.8)** ,whereas for Base Case correlation of melting process is already presented in **eq. (4.6)**.

$$\overline{Nu_m} = \left\{ \begin{array}{cc} c_1 \ (Ra)^{c_2}, & 338K \leq T_{HTF} \leq 378K \end{array} \right. \qquad (4.8)$$

where $c_1$=0.0163 and $c_2$=0.4571 for Case 1s and 4s.
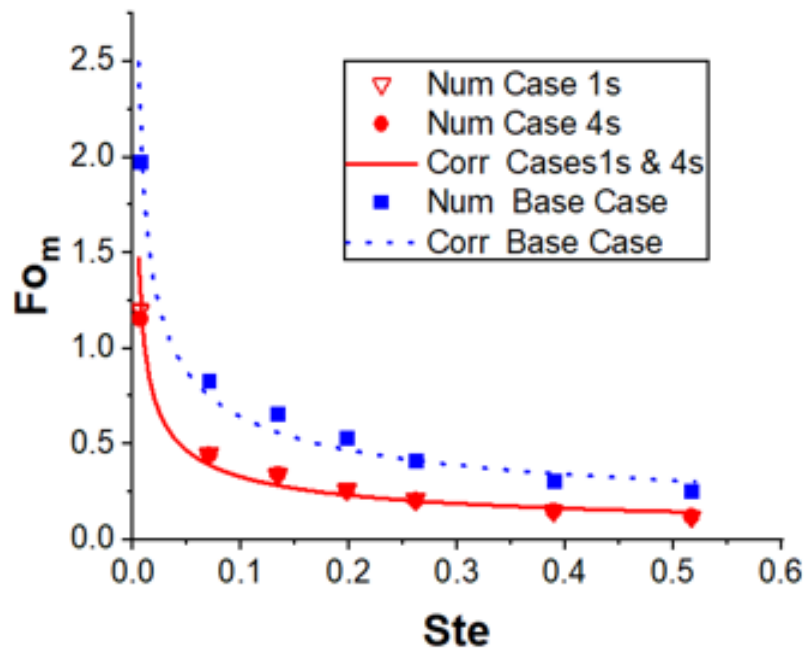


FIGURE 4.18: Relationship of Stefan Number with Fourier Number for Melting Process
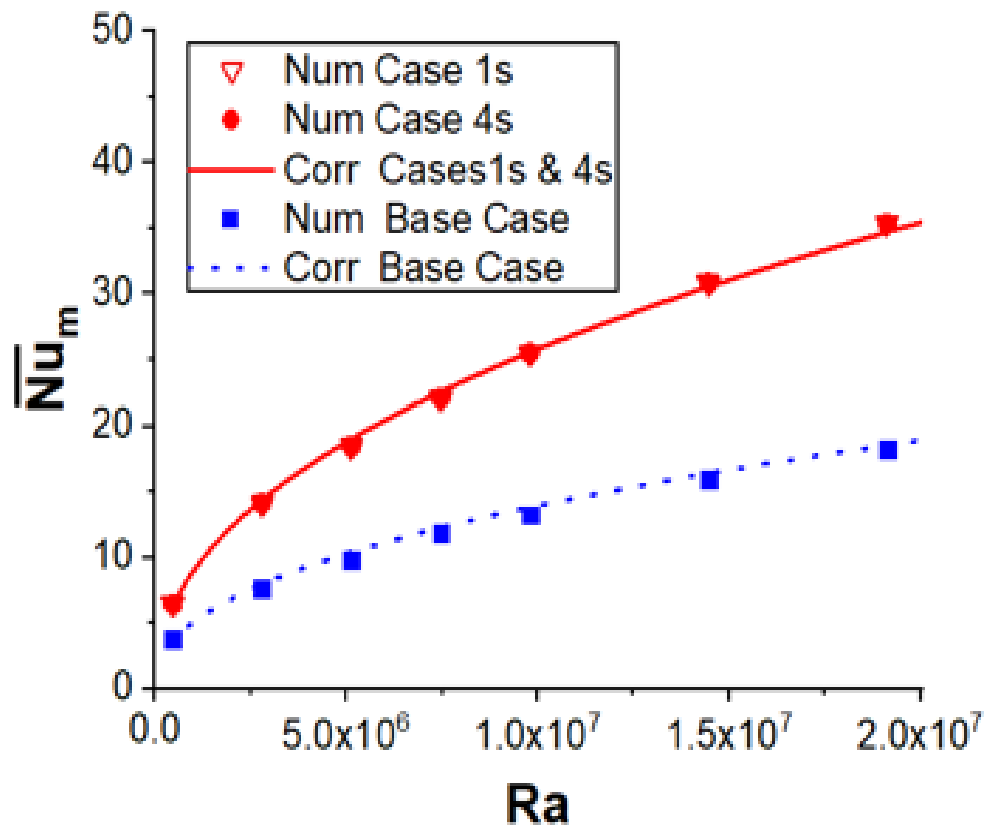
FIGURE 4.19: Relationship of Nusselt Number with Rayleigh Number for Melting Process

TABLE 4.3: Non-Dimensional Parameters for Different HTF Temperatures for Case 1s,4s

| $T_{HTF}$(K) | *Ste* | Fo | Ra | Avg. Nusselt Number |
|---|---|---|---|---|
| | | Melt. | Melt. | Melt. |
| 338 | 0.00638 | 1.1385 | $0.466 \times 10^6$ | 6.48 |
| 343 | 0.07019 | 0.47189 | $2.796 \times 10^6$ | 14.13 |
| 348 | 0.13399 | 0.32648 | $5.12 \times 10^6$ | 18.49 |
| 353 | 0.197802 | 0.221 | $7.45 \times 10^6$ | 22.09 |
| 358 | 0.261608 | 0.2061 | $9.78 \times 10^6$ | 25.51 |
| 368 | 0.38922 | 0.15278 | $14.4 \times 10^6$ | 30.84 |
| 378 | 0.51683 | 0.12138 | $19.11 \times 10^6$ | 35.35 |

# Chapter 5

# Conclusion and Future Work

The effects of splitting the single HTF tube into several smaller tubes and shell modifications on the thermal performance of horizontal shell and tube LTESS are studied in this thesis. In the first step, seven different designs with 2 – 5 HTF tubes with cylindrical shell are investigated and results are analyzed using different performance parameters in comparison with the Base Case. It is observed that Case 1 having two tubes arranged vertically and Case 4 having three tubes arranged in V-shape perform better as compared to the Base Case on the indicators of enhancement ratio, time saving, total melting time and energy storage rate. The reason is that the multiple heat transfer tubes are scattered in the shell and create strong convection currents and agitation to melt the PCM quickly.

The total melting times for Case 1 and Case 4 are 60 and 65 mins, respectively, as compared to 83 minutes required for the Base Case. This represents significant improvement depicting time saving of 27.7% and 21.7% for Case 1 and Case 4, respectively, compared to the Base Case. The corresponding average energy storage rates also increase by 33.6% and 23.7%, respectively. In the second step, the melting performance of Case 1 and Case 4 is further improved by intelligently modifying the shells and making them elliptic and triangular; these designs are named as Case 1s and Case 4s, respectively. The modified shell cases perform even better than the corresponding cylindrical shell cases. This is because in the new designs more PCM is placed above the HTF tubes which melts quickly due

to the strong convective currents. The performance parameters register further improvements compared to the Base Case.

The total melting times for Case 1s and Case 4s are 42 mins and 41 mins, respectively, which show time saving of 49.4% and 50.6% as compared to the Base Case. The average energy storage rates for Case 1s and Case 4s also increase by 85.7% and 84.8%, respectively, compared to the Base Case. The modified shell cases also distribute heat uniformly throughout the PCM in the unit resulting in the uniform temperature distribution and smooth energy transfer rates. On the basis of overall performance, cases 1s and 4s are considered as the best configurations. Finally, these best options are furtherer analyzed by varying the HTF temperature and observing the non-dimensional Stefan (Ste),Fourier (Fo), Nusselt (Nu) and Rayleigh (Ra) numbers. As the Stefan number is increased by increasing the HTF temperature, the total melting time decreases, i.e., faster melting. This is because an increase in the HTF temperature increases the buoyancy forces, i.e., the Rayleigh number. This results in enhanced convective heat transfer, i.e., higher Nusselt number.

The heat transfer augmentation techniques may also be introduced in the current design to further enhance thermal performance of LTESSs. These may include, addition of nano particles in PCMs, shape and geometrical modifications in HTF tube, effects of eccentricity of HTF tube. The inclusions of nano particles enhance the thermal conductivity of the PCM which ultimately lead to melting rates improvement.

However, large quantities of nano particles may reduce the charging capacity of LTESS due to reduction in overall heat storage capacity of PCM. Similarly, the change in the geometry of HTF tube should not be very complex since the manufacturing of the tubes can also become challenging. The use of eccentricity in PCM based heat storage systems improve natural convection effects in PCM and therefore enhance their thermal performance. However, eccentricity may cause some delay in discharging of the heat storage system. Therefore, a thorough study is required to be carried out in the future that can address these problems.

# Bibliography

[1] R. Wen, W. Zhang, Z. Lv, Z. Huang, and W. Gao, "A novel composite Phase change material of Stearic Acid/Carbonized sunflower straw for thermal energy storage," *Mater. Lett.*, vol. 215, pp. 42–45, 2018, doi: 10.1016/j.matlet.2017.12.008.

[2] A. Papadimitratos, S. Sobhansarbandi, V. Pozdin, A. Zakhidov, and F. Hassanipour, "Evacuated tube solar collectors integrated with phase change materials," *Sol. Energy*, vol. 129, pp. 10–19, 2016, doi: 10.1016/j.solener.2015.12.040.

[3] C. Muratore, S. M. Aouadi, and A. A. Voevodin, "Embedded phase change material microinclusions for thermal control of surfaces," *Surf. Coatings Technol.*, vol. 206, no. 23, pp. 4828–4832, 2012, doi: 10.1016/j. surfcoat.2012.05.030.

[4] K. Du, J. Calautit, Z. Wang, Y. Wu, and H. Liu, "A review of the applications of phase change materials in cooling, heating and power generation in different temperature ranges," *Appl. Energy*, vol. 220, no. March, pp. 242–273, 2018, doi: 10.1016/j.apenergy.2018.03.005.

[5] C. Liu and D. Groulx, "Experimental study of the phase change heat transfer inside a horizontal cylindrical latent heat energy storage system," *Int. J. Therm. Sci.*, vol. 82, no. 1, pp. 100–110, 2014, doi: 10.1016/j.ijthermalsci.2014.03.014.

[6] N. Zhang, Y. Yuan, X. Cao, Y. Du, Z. Zhang, and Y. Gui, "Latent Heat Thermal Energy Storage Systems with Solid–Liquid Phase Change Materials: A Review," *Adv. Eng. Mater.*, vol. 20, no. 6, pp. 1–30, 2018, doi: 10.1002/adem.201700753.

[7] C. Liu, Y. Yuan, N. Zhang, X. Cao, and X. Yang, "A novel PCM of lauric-myristic-stearic acid/expanded graphite composite for thermal energy storage," *Mater. Lett.*, vol. 120, pp. 43–46, 2014, doi: 10.1016/j.matlet.2014.01.051.

[8] L. F. Cabeza, A. Castell, C. Barreneche, A. De Gracia, and A. I. Fernández, "Materials used as PCM in thermal energy storage in buildings: A review," *Renew. Sustain. Energy Rev.*, vol. 15, no. 3, pp. 1675–1695, 2011, doi: 10.1016/j.rser.2010.11.018.

[9] A. F. Regin, S. C. Solanki, and J. S. Saini, "Heat transfer characteristics of thermal energy storage system using PCM capsules: A review," *Renew. Sustain. Energy Rev.*, vol. 12, no. 9, pp. 2438–2458, 2008, doi: 10.1016/j.rser.2007.06.009.

[10] A. Abhat, "Low temperature latent heat thermal energy storage: Heat storage materials," *Sol. Energy*, vol. 30, no. 4, pp. 313–332, 1983, doi: 10.1016/0038-092X(83)90186-X.

[11] G. A. Lane, "Low temperature heat storage with phase change materials," *Int. J. Ambient Energy*, vol. 1, no. 3, pp. 155–168, 1980, doi: 10.1080/01430750.1980.9 675731.

[12] M. M. Kenisarin, "Thermophysical properties of some organic phase change materials for latent heat storage. *A Review*," *Sol. Energy*, vol. 107, pp. 553–575, 2014, doi: 10.1016/j.solener.2014.05.001.

[13] A. Sari and A. Karaipekli, "Thermal conductivity and latent heat thermal energy storage characteristics of paraffin as phase change material," *Appl. Therm. Eng.*, vol. 27, no. 8–9, pp. 1271– 1277, 2007, doi: 10.1016/j.applthermaleng.2006.11.004.

[14] M. Akgün, O. Aydin, and K. Kaygusuz, "Thermal energy storage performance of paraffin in a novel tube-in-shell system," *Appl. Therm. Eng.*, vol. 28, no. 5–6, pp. 405–413, 2008, doi: 10.1016/j. applthermaleng. 2007.05.013.

[15] Y. Yuan, N. Zhang, W. Tao, X. Cao, and Y. He, "Fatty acids as phase change materials: A review," *Renew. Sustain. Energy Rev.*, vol. 29, pp. 482–498, 2014, doi: 10.1016/j. rser.2013.08.107.

[16] L. Feng, J. Zheng, H. Yang, Y. Guo, W. Li, and X. Li, "Preparation and characterization of polyethylene glycol/active carbon composites as shape-stabilized phase change materials," *Sol. Energy Mater. Sol. Cells*, vol. 95, no. 2, pp. 644–650, 2011, doi: 10.1016/j.solmat.2010.09.033.

[17] F. Bruno, M. Belusko, M. Liu, and N. H. S. Tay, Using solid-liquid phase change materials (PCMs) in thermal energy storage systems. *Woodhead Publishing Limited*, 2015.

[18] A. I. Fernández, C. Barreneche, M. Belusko, M. Segarra, F. Bruno, and L. F. Cabeza, "Considerations for the use of metal alloys as phase change materials for high temperature applications," *Sol. Energy Mater. Sol. Cells*, vol. 171, no. March, pp. 275–281, 2017, doi: 10.1016/j.solmat.2017.06.054.

[19] A. Sari, "Eutectic mixtures of some fatty acids for low temperature solar heating applications: Thermal properties and thermal reliability," *Appl. Therm. Eng.*, vol. 25, no. 14–15, pp. 2100–2107, 2005, doi: 10.1016/j.applthermaleng.2005.01.010.

[20] M. Fang and G. Chen, "Effects of different multiple PCMs on the performance of a latent thermal energy storage system," *Appl. Therm. Eng.*, vol. 27, no. 5–6, pp. 994–1000, 2007, doi: 10.1016/j.applthermaleng.2006.08.001.

[21] J. M. Mahdi, H. I. Mohammed, E. T. Hashim, P. Talebizadehsardari, and E. C. Nsofor, "Solidification enhancement with multiple PCMs, cascaded metal foam and nanoparticles in the shell-and-tube energy storage system," *Appl. Energy*, vol. 257, no. June 2019, p. 113993, 2020, doi: 10.1016/j.apenergy.2019.113993.

[22] D. D. Winfred Rufuss, S. Iniyan, L. Suganthi, and D. Pa, "Nanoparticles Enhanced Phase Change Material (NPCM) as Heat Storage in Solar Still Application for Productivity Enhancement," *Energy Procedia*, vol. 141, pp. 45–49, 2017, doi: 10.1016/j.egypro.2017.11.009.

[23] J. M. Khodadadi and S. F. Hosseinizadeh, "Nanoparticle-enhanced phase change materials (NEPCM) with great potential for improved thermal energy

storage," *Int. Commun. Heat Mass Transf.*, vol. 34, no. 5, pp. 534–543, 2007, doi: 10.1016/j.icheatmasstransfer.2007.02.005.

[24] S. Ebadi, S. H. Tasnim, A. A. Aliabadi, and S. Mahmud, "Melting of nano-PCM inside a cylindrical thermal energy storage system: Numerical study with experimental verification," *Energy Convers. Manag.*, vol. 166, no. March, pp. 241–259, 2018, doi: 10.1016/j.enconman.2018.04.016.

[25] W. L. Cheng, R. M. Zhang, K. Xie, N. Liu, and J. Wang, "Heat conduction enhanced shape-stabilized paraffin/HDPE composite PCMs by graphite addition: Preparation and thermal properties," *Sol. Energy Mater. Sol. Cells*, vol. 94, no. 10, pp. 1636–1642, 2010, doi: 10.1016/j.solmat.2010.05.020.

[26] A. H. N. Al-Mudhafar, A. F. Nowakowski, and F. C. G. A. Nicolleau, "Performance enhancement of PCM latent heat thermal energy storage system utilizing a modified webbed tube heat exchanger," *Energy Reports*, vol. 6, pp. 76–85, 2020, doi: 10.1016/j.egyr.2020.02.030.

[27] F. Agyenim, P. Eames, and M. Smyth, "Heat transfer enhancement in medium temperature thermal energy storage system using a multitube heat transfer array," *Renew. Energy*, vol. 35, no. 1, pp. 198–207, 2010, doi: 10.1016/j.renene.2009.03.0 10.

[28] M. Esapour, M. J. Hosseini, A. A. Ranjbar, Y. Pahamli, and R. Bahrampoury, "Phase change in multi-tube heat exchangers," *Renew. Energy*, vol. 85, pp. 1017–1025, 2016, doi: 10.1016/j.renene.2015.07.063.

[29] H. Liu, S. Li, Y. Chen, and Z. Sun, "The melting of phase change material in a cylinder shell with hierarchical heat sink array," *Appl. Therm. Eng.*, vol. 73, no. 1, pp. 975–983, 2014, doi: 10.1016/j.applthermaleng.2014.08.062.

[30] J. Liu, C. Xu, X. Ju, B. Yang, Y. Ren, and X. Du, "Numerical investigation on the heat transfer enhancement of a latent heat thermal energy storage system with bundled tube structures," *Appl. Therm. Eng.*, vol. 112, pp. 820–831, 2017, doi: 10.1016/j.applthermaleng.2016.10.144.

[31] S. P. Jesumathy, M. Udayakumar, S. Suresh, and S. Jegadheeswaran, "An experimental study on heat transfer characteristics of paraffin wax in horizontal double pipe heat latent heat storage unit," *J. Taiwan Inst. Chem. Eng.*, vol. 45, no. 4, pp. 1298–1306, 2014, doi: 10.1016/j.jtice.2014.03.007.

[32] N. Kousha, M. Rahimi, R. Pakrouh, and R. Bahrampoury, "Experimental investigation of phase change in a multitube heat exchanger," *J. Energy Storage*, vol. 23, no. December 2018, pp. 292–304, 2019, doi: 10.1016/j.est.2019.03.024.

[33] M. M. Joybari, S. Seddegh, X. Wang, and F. Haghighat, "Experimental investigation of multiple tube heat transfer enhancement in a vertical cylindrical latent heat thermal energy storage system," *Renew. Energy*, vol. 140, pp. 234–244, 2019, doi: 10.1016/j.renene.2019.03.037.

[34] M. Alizadeh, M. H. Pahlavanian, M. Tohidi, and D. D. Ganji, "Solidification expedition of Phase Change Material in a triplex-tube storage unit via novel fins and SWCNT nanoparticles," *J. Energy Storage*, vol. 28, no. December 2019, p. 101188, 2020, doi: 10.1016/j.est.2019.101188.

[35] Y. Yuan, X. Cao, B. Xiang, and Y. Du, "Effect of installation angle of fins on melting characteristics of annular unit for latent heat thermal energy storage," *Sol. Energy*, vol. 136, pp. 365–378, 2016, doi: 10.1016/j.solener.2016.07.014.

[36] A. H. Mosaffa, F. Talati, H. Basirat Tabrizi, and M. A. Rosen, "Analytical modeling of PCM solidification in a shell and tube finned thermal storage," *Energy Build.*, vol. 49, pp. 356–361, 2012, doi: 10.1016/j.enbuild.2012.02.053.

[37] R. Baby and C. Balaji, "Thermal optimization of PCM based pin fin heat sinks: An experimental study," *Appl. Therm. Eng.*, vol. 54, no. 1, pp. 65–77, 2013, doi: 10.1016/j.applthermaleng.2012.10.056.

[38] M. S. Yousef, H. Hassan, S. Kodama, and H. Sekiguchi, "An experimental study on the performance of single slope solar still integrated with a PCM-based pin-finned heat sink," *Energy Procedia*, vol. 156, no. September 2018, pp. 100–104, 2019, doi: 10.1016/j.egypro.2018.11.102.

[39] Z. Sun, R. Fan, F. Yan, T. Zhou, and N. Zheng, "Thermal management of the lithium-ion battery by the composite PCM-Fin structures," *Int. J. Heat Mass Transf.*, vol. 145, p. 118739, 2019, doi: 10.1016/j.ijheatmasstransfer.2019.118739.

[40] A. Acır and M. Emin Canlı, "Investigation of fin application effects on melting time in a latent thermal energy storage system with phase change material (PCM)," *Appl. Therm. Eng.*, vol. 144, pp. 1071–1080, 2018, doi: 10.1016/j.applthermaleng.2018.09.013.

[41] A. Sciacovelli, F. Gagliardi, and V. Verda, "Maximization of performance of a PCM latent heat storage system with innovative fins," *Appl. Energy*, vol. 137, pp. 707–715, 2015, doi: 10.1016/j.apenergy.2014.07.015.

[42] S. Mat, A. A. Al-Abidi, K. Sopian, M. Y. Sulaiman, and A. T. Mohammad, "Enhance heat transfer for PCM melting in triplex tube with internal-external fins," *Energy Convers. Manag.*, vol. 74, pp. 223–236, 2013, doi: 10.1016/j.enconman.2013.05.003.

[43] Z. Khan, Z. Khan, and K. Tabeshf, "Parametric investigations to enhance thermal performance of paraffin through a novel geometrical configuration of shell and tube latent thermal storage system," *Energy Convers. Manag.*, vol. 127, pp. 355–365, 2016, doi: 10.1016/j.enconman.2016.09.030.

[44] X. Yang, Z. Lu, Q. Bai, Q. Zhang, L. Jin, and J. Yan, "Thermal performance of a shell-and-tube latent heat thermal energy storage unit: Role of annular fins," *Appl. Energy*, vol. 202, pp. 558–570, 2017, doi: 10.1016/j.apenergy.2017.05.007.

[45] P. Wang, H. Yao, Z. Lan, Z. Peng, Y. Huang, and Y. Ding, "Numerical investigation of PCM melting process in sleeve tube with internal fins," *Energy Convers. Manag.*, vol. 110, pp. 428–435, 2016, doi: 10.1016/j.enconman.2015.12.042.

[46] M. J. Hosseini, A. A. Ranjbar, M. Rahimi, and R. Bahrampoury, "Experimental and numerical evaluation of longitudinally finned latent heat thermal storage systems," *Energy Build.*, vol. 99, pp. 263–272, 2015, doi: 10.1016/j.enbuild.2015.04.045.

[47] M. K. Rathod and J. Banerjee, "Thermal performance enhancement of shell and tube Latent Heat Storage Unit using longitudinal fins," *Appl. Therm. Eng.*, vol. 75, pp. 1084–1092, 2015, doi: 10.1016/j.applthermaleng.2014.10.074.

[48] A. A. Al-Abidi, S. Mat, K. Sopian, M. Y. Sulaiman, and A. T. Mohammad, "Internal and external fin heat transfer enhancement for thermal energy storage in triplex tube heat exchangers," *Appl. Therm. Eng.*, vol. 53, no. 1, pp. 147–156, 2013, doi: 10.1016/j.applthermaleng.2013.01.011.

[49] X. Cao, Y. Yuan, B. Xiang, L. Sun, and Z. Xingxing, "Numerical investigation on optimal number of longitudinal fins in horizontal annular phase change unit at different wall temperatures," *Energy Build.*, vol. 158, pp. 384–392, 2018, doi: 10.1016/j.enbuild.2017.10.029.

[50] S. Deng, C. Nie, G. Wei, and W. B. Ye, "Improving the melting performance of a horizontal shell-tube latent-heat thermal energy storage unit using local enhanced finned tube," *Energy Build.*, vol. 183, pp. 161–173, 2019, doi: 10.1016/j.enbuild.2018.11.018.

[51] M. Kazemi, M. J. Hosseini, A. A. Ranjbar, and R. Bahrampoury, "Improvement of longitudinal fins configuration in latent heat storage systems," *Renew. Energy*, vol. 116, pp. 447–457, 2018, doi: 10.1016/j.renene.2017.10.006.

[52] A. M. Abdulateef, S. Mat, K. Sopian, J. Abdulateef, and A. A. Gitan, "Experimental study of melting phase-change material in a triplex tube heat exchanger fins," *Sol. Energy*, vol. 155, pp. 142–153, 2017, doi: 10.1016/j.solener.2017.06.024.

[53] L. A. Khan and M. M. Khan, "Role of orientation of fins in performance enhancement of a latent thermal energy storage unit," *Appl. Therm. Eng.*, vol. 175, no. December 2019, p. 115408, 2020, doi: 10.1016/j.applthermaleng.2020.115408.

[54] A. Pizzolato, A. Sharma, R. Ge, K. Maute, V. Verda, and A. Sciacovelli, "Maximization of performance in multi-tube latent heat storage – Optimization of fins topology, effect of materials selection and flow arrangements," *Energy*, vol. 203, 2020, doi: 10.1016/j.energy.2019.02.155.

[55] C. W. Robak, T. L. Bergman, and A. Faghri, "Enhancement of latent heat energy storage using embedded heat pipes," *Int. J. Heat Mass Transf.*, vol. 54, no. 15–16, pp. 3476–3484, 2011, doi: 10.1016/j.ijheatmasstransfer.2011.03.038.

[56] S. Tiari, S. Qiu, and M. Mahdavi, "Numerical study of finned heat pipe-assisted thermal energy storage system with high temperature phase change material," *Energy Convers. Manag.*, vol. 89, pp. 833–842, 2015, doi: 10.1016/j.enconman.2014.10.053.

[57] T. Bouhal, S. ed-Dîn Fertahi, T. Kousksou, and A. Jamil, "CFD thermal energy storage enhancement of PCM filling a cylindrical cavity equipped with submerged heating sources," *J. Energy Storage*, vol. 18, no. April, pp. 360–370, 2018, doi: 10.1016/j.est.2018.05.015.

[58] A. Pourakabar and A. A. Rabienataj Darzi, "Enhancement of phase change rate of PCM in cylindrical thermal energy storage," *Appl. Therm. Eng.*, vol. 150, no. January, pp. 132–142, 2019, doi: 10.1016/j.applthermaleng.2019.01.009.

[59] M. Faghani, M. J. Hosseini, and R. Bahrampoury, "Numerical simulation of melting between two elliptical cylinders," *Alexandria Eng. J.*, vol. 57, no. 2, pp. 577–586, 2018, doi: 10.1016/j.aej.2017.02.003.

[60] D. H. Shin, J. Park, S. H. Choi, H. S. Ko, S. W. Karng, and Y. Shin, "A new type of heat storage system using the motion of phase change materials in an elliptical-shaped capsule," *Energy Convers. Manag.*, vol. 182, no. December 2018, pp. 508–519, 2019, doi: 10.1016/j.enconman.2018.12.091.

[61] E. Assis, L. Katsman, G. Ziskind, and R. Letan, "Numerical and experimental study of melting in a spherical shell," *Int. J. Heat Mass Transf.*, vol. 50, no. 9–10, pp. 1790–1804, 2007, doi: 10.1016/j.ijheatmasstransfer.2006.10.007.

[62] W. Li, S. G. Li, S. Guan, Y. Wang, X. Zhang, and X. Liu, "Numerical study on melt fraction during melting of phase change material inside a sphere," *Int. J. Hydrogen Energy*, vol. 42, no. 29, pp. 18232–18239, 2017, doi: 10.1016/j.ijhydene.2017.04.136.

[63] V. R. Voller & C. Prakash, "A Fixed grid numerical modelling methodology for convection diffusion mushy region phase change problems," *Int. Jounal Heat Mass Transf.*, vol. 30, no. 8, pp. 1709–1719, 1978.

[64] J. Vogel and A. Thess, "Validation of a numerical model with a benchmark experiment for melting governed by natural convection in latent thermal energy storage," *Appl. Therm. Eng.*, vol. 148, pp. 147–159, 2019, doi: 10.1016/j.appltherma leng.2018.11.032.

[65] T. J. B. C. Jespersen, "The design and application of upwind schemes on unstructured meshes. *Moffett Field , CA 27th Aerospace Sciences Meeting,*" *27th Aerosp. Sci. Meet.*, 1989.

[66] ANSYS Academic Research, "ANSYS Fluent Theory Guide," ANSYS Help Syst., no. January, 2018.

[67] M. Garcia-Vilchez et al., "Computational fluid dynamics and particle image velocimetry assisted design tools for a new generation of trochoidal gear pumps," *Adv. Mech. Eng.*, vol. 7, no. 7, pp. 1–14, 2015, doi: 10.1177/1687814015592561.

[68] B. R. Munson, D. F. Young, and T. H. Okiishi, "Fundamentals of fluid mechanics," *Fundam. Fluid Mech.*, 1994, doi: 10.1201/b15874-3.

[69] A. A. Al-abidi, S. Mat, K. Sopian, M. Y. Sulaiman, and A. Th, "Experimental study of melting and solidification of PCM in a triplex tube heat exchanger with fins," *Energy Build.*, vol. 68, pp. 33–41, 2014, doi: 10.1016/j.enbuild.2013.09.007.

[70] C. Gau and R. Viskanta, "Melting and solidification of a pure metal on a vertical wall," *J. Heat Transfer*, vol. 108, no. 1, pp. 174–181, 1986, doi: 10.1115/1.3246884.

[71] A. D. Brent, V. R. Voller, and K. J. Reid, "Enthalpy-porosity technique for modeling convection-diffusion phase change: Application to the melting of a pure metal," *Numer. Heat Transf.*, vol. 13, no. 3, pp. 297–318, 1988, doi: 10.1080/10407788808913615.

[72] B. W. Webb and R. Viskanta, "Analysis of heat transfer during melting of a pure metal from an isothermal vertical wall," *Numer. Heat Transf.*, vol. 9, no. 5, pp. 539–558, May 1986, doi: 10.1080/10407788608913492.

[73] Z. J. Zheng, Y. Xu, and M. J. Li, "Eccentricity optimization of a horizontal shell-and-tube latent-heat thermal energy storage unit based on melting and melting-solidifying performance," *Appl. Energy*, vol. 220, no. March, pp. 447–454, 2018, doi: 10.1016/j.apenergy.2018.03.126.